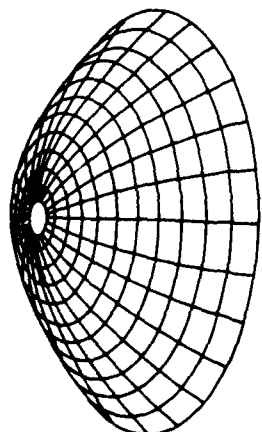
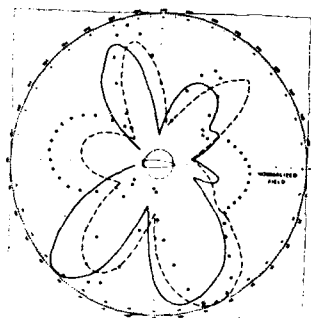
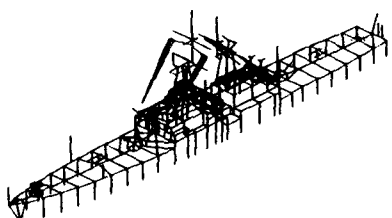
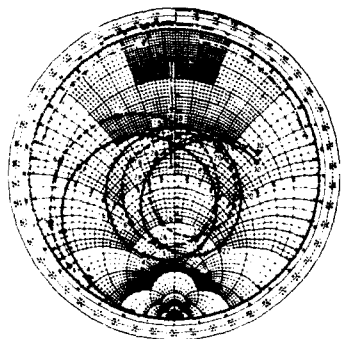
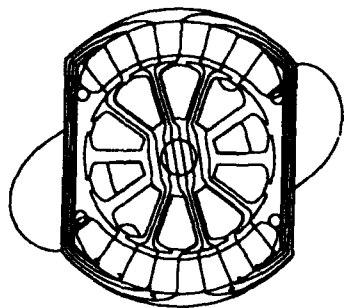


2

AD-A276 753



APPLIED  
COMPUTATIONAL  
ELECTROMAGNETICS  
SOCIETY  
Journal

DTIC  
ELECTE  
MAR 10 1994  
S E D

March 1994  
Vol. 9 No. 1

ISSN 1054-4887

Approved for public release  
Distribution is unlimited

94-07818



**GENERAL PURPOSE AND SCOPE.** The Applied Computational Electromagnetics Society Journal hereinafter known as the ACES Journal is devoted to the exchange of information in computational electromagnetics, to the advancement of the state-of-the-art, and to the promotion of related technical activities. A primary objective of the information exchange is the elimination of the need to "re-invent the wheel" to solve a previously-solved computational problem in electrical engineering, physics, or related fields of study. The technical activities promoted by this publication include code validation, performance analysis, and input/output standardization; code or technique optimization and error minimization; innovations in solution technique or in data input/output; identification of new applications for electromagnetics modeling codes and techniques; integration of computational electromagnetics techniques with new computer architectures; and correlation of computational parameters with physical mechanisms.

**SUBMISSIONS CONTENT.** The ACES Journal welcomes original, previously unpublished papers, relating to applied computational electromagnetics.

Typical papers will represent the computational electromagnetics aspects of research in electrical engineering, physics, or related disciplines. However, papers which represent research in applied computational electromagnetics itself are equally acceptable.

For additional details, see "Information for Authors", elsewhere in this issue.

**SUBSCRIPTIONS.** All members of the Applied Computational Electromagnetics Society (ACES) who have paid their subscription fees are entitled to receive the ACES Journal with a minimum of two issues per calendar year. Current annual subscription fees are subject to change every 1 April. Current fees are:

**AREAS:** U.S. and Canada: AIRMAIL: \$60 Individual, \$110 Organizational, SURFACE MAIL N/A; Mexico, Central & So. America: AIRMAIL: \$65 Individual, \$110 Organizational, SURFACE MAIL: \$63; Europe, Former USSR, Turkey, Scandinavia, AIRMAIL: \$73 Individual, \$110 Organizational, SURFACE MAIL: \$63; Asia, Africa, Middle East and Pacific Rim: AIRMAIL: \$80 Individual, \$110 Organizational, SURFACE MAIL: \$63. **FULL-TIME STUDENTS:** \$25.00. **REMIT BY:** (1) BANK DRAFTS (MUST BE DRAWN ON U.S. BANK), (2) INTERNATIONAL MONEY ORDER, (3) TRAVELER'S CHECKS IN U.S. DOLLARS, (4) ELECTRONIC TRANSFER, (CONTACT ACES EXECUTIVE OFFICER, RICHARD ADLER).

Back issues, when available, are \$15.00 each. Subscriptions to ACES, orders for back issues of the ACES Journal and changes of addresses should be sent to:

Dr. Richard Adler  
ACES Executive Officer  
ECE Department, Code ECAB  
Naval Postgraduate School  
833 Dyer Road, Room 437  
Monterey, CA 93943-5121 USA

Allow four week's advance notice for change of address. Claims for missing issues will not be honored because of insufficient notice or address change or loss in mail unless the secretary is notified within 60 days for USA and Canadian subscribers or 90 days for subscribers in other countries, from the last day of the month of publication. For information regarding reprints of individual papers or other materials, see "Information for Authors".

**LIABILITY.** Neither ACES or the ACES Journal editors are responsible for any consequence of misinformation or claims, express or implied, in any published material in an ACES Journal issue. This also applies to advertising, for which only camera-ready copies are accepted. Authors are responsible for information contained in their papers. If any material submitted for publication includes material which has already been published elsewhere, it is the author's responsibility to obtain written permission to reproduce such material.

APPLIED  
 COMPUTATIONAL  
 ELECTROMAGNETICS  
 SOCIETY  
 Journal

March 1994  
 Vol. 9 No. 1

ISSN 1054-4887

Accession For	
NTIS CRA&I	<input checked="" type="checkbox"/>
DTIC TAB	<input type="checkbox"/>
Unannounced	<input type="checkbox"/>
Justification .....	
By .....	
Distribution /	
Availability Codes	
Dist	Avail and/or Special
A-1	

The ACES Journal is abstracted in INSPEC, in Engineering Index, and in DTIC.

The second, third, fourth, and fifth illustrations on the front cover have been obtained from Lawrence Livermore National laboratory.

The first illustration on the front cover has been obtained from FLUX2D software, CEDRAT S.S. France, MAGSOFT Corporation, New York.

# THE APPLIED COMPUTATIONAL ELECTROMAGNETICS SOCIETY JOURNAL

## EDITORS

### EDITOR-IN-CHIEF/ACES

W. Perry Wheless, Jr.  
University of Alabama, EE Dept.  
PO Box 870286  
Tuscaloosa, AL 35487-0286 U.S.A.

### EDITOR-IN-CHIEF/JOURNAL

Duncan C. Baker  
EE Dept. University of Pretoria  
0002 Pretoria, SOUTH AFRICA

### MANAGING EDITOR

Richard W. Adler  
ECE Department Code ECAB  
Naval Postgraduate School  
Monterey, CA 93943-5121, U.S.A.

### EDITOR-IN-CHIEF, EMERITUS

Robert M. Bevensee  
Box 812  
Alamo, CA 94507-0516 U.S.A.

### EDITOR-IN-CHIEF, EMERITUS

David E. Stein  
Headquarters Air Force Sys. Cmd.  
PO Box 169,  
Linthicum Heights, MD 21090 U.S.A.

Brian A. Austin  
University of Liverpool  
Liverpool, UK

Christian Hafner  
Swiss Federal Inst. of Technology  
Zurich, SWITZERLAND

Adalbert Konrad  
University of Toronto  
Toronto, Ontario, CANADA

Fulvio Bessi  
Ingegneria del Sistemi S.p.A.  
Pisa, ITALY

Roger Harrington  
Syracuse University  
Syracuse, NY, U.S.A.

Peter Krylstedt  
National Defence Research Est.  
Sundbyberg, SWEDEN

Robert Bevensee  
Box 812  
Alamo, CA U.S.A.

Donald F. Herrick  
ERIM  
Ann Arbor, MI, U.S.A.

Stanley Kubina  
Concordia University  
Montreal, Quebec, CANADA

John R. Bowler  
University of Surrey  
Surrey, UK

Kuetchien C. Hill  
Wright Laboratory  
Wright-Patterson AFB, OH, U.S.A.

Karl J. Langenberg  
Universitat Kassel  
Kassel, GERMANY

Robert T. Brown  
Lockheed Aeronautical Sys. Co.  
Valencia, CA, U.S.A.

Todd H. Hubing  
University of Missouri-Rolla  
Rolla, MO, U.S.A.

Ronald Marhefka  
Ohio State University  
Columbus, OH, U.S.A.

Chalmers M. Butler  
Clemson University  
Clemson, SC, U.S.A.

Nathan Ida  
The University of Akron  
Akron, OH, U.S.A.

Gerald Meunier  
INPG/ENSIEG  
St. Martin-d'Herès Cedex, FRANCE

Edgar Coffey  
Advanced Electromagnetics  
Albuquerque, NM, U.S.A.

Magdy F. Iskander  
University of Utah  
Salt Lake City, UT, U.S.A.

Edmund K. Miller  
3225 Calle Celestial  
Santa Fe, NM, U.S.A.

Tony Fleming  
Telecom Australia  
Clayton, Victoria, AUSTRALIA

Kiyohiko Itoh  
Hokkaido University  
Sapporo, JAPAN

Kenzo Miya  
University of Tokyo  
Tokyo, JAPAN

Pat Foster  
Microwave & Antenna Systems  
Gt. Malvern, Worc. UK

Randy J. Jost  
SRI International  
Arlington, VA, U.S.A.

Osama A. Mohammed  
Florida International University  
Miami, FL, U.S.A.

Gregory R. Haack  
DSTO Salisbury  
Salisbury, SA, AUSTRALIA

Linda P.B. Katchl  
University of Michigan  
Ann Arbor, MI, U.S.A.

Giorgio Molinari  
University of Genova  
Genova, ITALY

## **EDITORS (Continued)**

**Frederic A. Molinet**  
Societe Mothesim  
Le Plessis-Robinson, FRANCE

**Gerrit Mur**  
Technische Universiteit Delft  
Delft, NETHERLANDS

**Takayoshi Nakata**  
Okayama University  
Okayama, JAPAN

**Andrew F. Peterson**  
Georgia Institute of Technology  
Atlanta, GA, U.S.A.

**Harold A. Sabbagh**  
Sabbagh Associates  
Bloomington, IN, U.S.A.

**Chris Smith**  
Kaman Sciences Corp.  
Colorado Springs, CO, U.S.A.

**David E. Stein**  
PO Box 169  
Linthicum Heights, MD, U.S.A.

**C.W. "Bill" Trowbridge**  
Vector Fields Limited  
Oxford, UK

**Jean-Claude Verite**  
Electricite de France  
Clamart, Cedex, FRANCE

**Frank Walker**  
Boeing Defence & Space Group  
Seattle, WA U.S.A.

**Keith W. Whites**  
University of Kentucky  
Lexington, KY, U.S.A.

**John W. Williams**  
SAIC  
Germantown, MD 20874

**Manfred Wurm**  
FB Technik  
Kiel, GERMANY

# THE APPLIED COMPUTATIONAL ELECTROMAGNETICS

## SOCIETY JOURNAL

Vol. 9 No. 1

March 1994

### TABLE OF CONTENTS

"Editorial" by D.C. Baker .....	5
"On the Use of Bivariate Spline Interpolation of Slot Data in the Design of Slotted Waveguide Arrays" by D.A. McNamara and J. Joubert .....	6
"A Technique for Determining Non-Integer Eigenvalues for Solutions of Ordinary Differential Equations" by D. Reuster and M. Kaye .....	10
"Antenna Modeling and Characterization of a VLF Airborne Dual Trailing Wire Antenna System" by J.K. Breakall, D.H. Werner and R.J. Lunnen .....	18
"Electromagnetic Scattering from Two-Dimensional Composite Objects" by A.A. Kishk and P.J. Goggans .....	32
"Efficient Matrix Element Calculations for the Spectral Domain Method Applied to Symmetrical Multiconductor Transmission Lines" by J.C. Coetzee and J.A.G. Malherbe .....	40
"Parallel Implementation of the Numerical Electromagnetics Code" by D.C. Nitch and A.P.C. Fourie .....	51
"Validation of the Mininec3 Code for Complex Radiating Structures" by K.P. Murray and B.A. Austin .....	58
"Some Examples of the Prediction and Validation of Near-Field Dependent Aircraft HF Antenna Parameters Using NEC" by J.W.R. Cox .....	67
"Use of a Stealth Boundary with Finite Difference Frequency Domain Simulations of Simple Antenna Problems" by R.B. Thompson, F.S. Chute and F.E. Vermeulen .....	78
"Two Wire Rhombic Illuminator Performance as Predicted by Theoretical and Numerical Models" by J.P. Donohoe, S.N. Tabet and C.D. Taylor .....	88
Institutional Membership .....	102

## **LETTER FROM THE EDITOR-IN-CHIEF, ACES JOURNAL**

We live in times when our personal and professional circumstances are increasingly subject to rapid change. The same is true of the ACES Journal. The March 1994 issue is the first one which I have had the privilege of putting together as the new and untried Editor-in-Chief. I now realize the tremendous contributions that David Stein has made over the years as Editor-in-Chief for ACES. This contribution can be measured against the fact that it has taken three people, Perry Wheless, Jr., Adalbert Konrad and myself to replace him. Perry is the new Editor-in-Chief for ACES with overall responsibility for the ACES publications, while Adalbert is Associate Editor-in-Chief of the ACES Journal. Adalbert's expertise will be particularly useful in the field of low frequency power electromagnetics. On behalf of our Journal I acknowledge and thank Dave Stein for his dedication and hard work over the years to ensure that the Journal will occupy a position of pre-eminence in the applied electromagnetics community.

This year also marks the Tenth Review of Progress in Applied Computational Electromagnetics. It is appropriate that ACES and all its committees should take stock of their achievements and plan a new course for the future at this time. The Journal is always reviewing its role within ACES and investigating ways and means of better serving its readership. With the able assistance of the panel of Journal editors, Perry, Adalbert and I are reviewing the type of article which would have the greatest value for our readers. Inevitably, there will be differences of opinion because of the diversity of interests of the ACES members and readers of the Journal. We will strive for the best possible compromise to ensure that the articles will be of interest to the broadest cross-section of our members and readers, and that these articles will support the objectives of ACES. As Editors-in-Chief we do however, reserve the right to publish articles which may be contentious and, hopefully, thought provoking as well as those which may open up a new area of investigation.

As with all technical publications, the ACES Journal and Newsletter are faced with ever increasing publication costs. This issue serves as a trial run for one method of reducing these costs. The reader will notice that several articles have been published in a compact format using double columns and a reduced font size. The effect of this has been to reduce the number of printed pages, and thus costs, without affecting the actual length of the papers themselves. Our sincere thanks to those authors who have been able to assist with this trial run. Our readers are invited to give constructive criticism of these changes. Please note that no author's paper will be turned down because he/she is unable to accommodate the compact format.

As Editor-in-Chief of the Journal I gratefully acknowledge the support and assistance of Perry Wheless, Adalbert Konrad, Dick Adler and Dave Stein in putting this issue together. Not surprisingly, Dave has been particularly generous in passing on the wisdom and experience he has built up over the years.

Finally, the Journal reflects the collective wisdom and hard work of each and every author, along with the constructive criticism of various editors and unnamed reviewers who have given generously of their time and experience. Without them there would be no Journal.

Duncan C. Baker

# ON THE USE OF BIVARIATE SPLINE INTERPOLATION OF SLOT DATA IN THE DESIGN OF SLOTTED WAVEGUIDE ARRAYS

Derek A. McNamara and Johan Joubert

*Department of Electrical & Electronic Engineering, University of Pretoria, Pretoria, South Africa 0002*

**Abstract :** *Essential to the design process of slotted waveguide arrays is an accurate knowledge of the self-properties of the individual slots. These properties can be computed with sufficient accuracy using moment method codes, which are too computationally intensive to be incorporated into design codes for large arrays. This paper describes an interpolation scheme which provides both sufficiently accurate, and rapid, computation of slot data from a pre-determined database to be viable for use in a slotted waveguide array design code.*

## 1. INTRODUCTION

It is correct to state that the structured design of high-performance slotted waveguide arrays began with the publication by Elliott [1] in 1978. All the design procedures available in the literature are, to the best of the authors' knowledge, based on this original approach [2,3], with further discussions [3] aimed principally at examining the correlation of the design method with experiment or the details of its implementation.

Essential to the design process is an ability to determine the self-properties of the individual slots. These properties can be computed with sufficient accuracy using moment method techniques. In a recent paper [3], which very carefully compares theory and experiment, the inclusion of the moment method computation itself in the design process has been suggested. However, because of the extensive computational effort involved, this has only been used in connection with the design of linear arrays of slots with no more than 21 elements. An even braver approach has been presented by Gulick and Elliott [4], where the moment method is used to obtain a complete solution for the integral equation formulation of the array antenna considered as a whole. The advantage of this scheme is that it does not require individual characterisation of the radiating elements, with mutual coupling, both internal and external, being handled automatically. However, this approach has thus far only been demonstrated on an array of 8 slots and is at present not a practical procedure for the design (as opposed to analysis only) of large planar arrays.

Although the moment method formulations [5,6,7] are quite efficient, they are still too computationally intensive to be incorporated into design codes for large arrays. Although it is possible to use approximate formulas for slot properties, it is possible to avoid any compromise and use numerically generated slot data along with a spline interpolation scheme for use in the design phase. This has already been an approach recommended in microstrip circuit design [8] and the modeling of antenna near a half-space [11].

When designing slotted waveguide arrays, the waveguide dimensions (e.g. full-height, half-height, quarter-height) and wall thickness would have been determined before the start of the design. Practical fabrication considerations usually require that the slot width be the same pre-determined value for each of the slots. Also, although the array performance may be analysed at a number of frequencies, any design run is done at some single frequency. Thus, if the results of the moment method code, namely complex  $s_{11}$  and  $s_{21}$  (or complex self-immittances of the equivalent network model) are obtained over the range of slot offsets  $x_0$  and lengths  $2l$  (these are shown in Fig.1), such sets of data can be considered as bivariate functions of the variables  $x_0$  and  $2l$ . Ready-to-use computer routines are available [9] for performing a bivariate spline interpolation, and these have been used by the present authors.

## 2. BIVARIATE CUBIC SPLINE INTERPOLATION OF SLOT SCATTERING PARAMETERS

The procedure is to establish (via the moment method code) the slot data at some single frequency at selected values of the two independent variables  $x_0$  and  $2l$ . The range of this data will usually be known from previous experience or examination of the literature. This data may be the complex  $s_{11}$  and  $s_{21}$ , from which equivalent network parameters are easily obtained, or such equivalent network parameters themselves. The routine *SPLIE2* [9,P.100] is then run with this data as input in order to compute certain derivative data needed for the final spline interpolation. Thereafter the original slot data, plus that generated by *SPLIE2*, is used with routine *SPLIN2* [9,p.101] to compute interpolated values of the

slot data for any given  $x_0$  and  $2l$  combination as requested by a design code. This process is as rapid as if direct closed-form formula such as the variational expression in [10] were utilised (which is not sufficiently accurate of course), even when many data nodes are used. The latter remark applies to the other quantities as well. Note that the above-mentioned routines also require the availability of two others (*SPLINE* and *SPLINT*), also available in [9, pp.86-89].

In order to illustrate this point, Table 1 shows the scattering parameters (magnitude and phase) for various slot lengths and offsets (at 9.0 GHz in half-height X-band waveguide) computed with the moment method code and with the spline interpolation procedure from a database. The width of the slots were taken as 1.6 mm and the wall thickness of the waveguide as 0.9 mm. Database values were computed with the moment method code at 23 node points in slot length (13 mm to 24 mm in steps of .5 mm) and 12 node points in slot offset (.8 mm and 1 mm to 6 mm in steps of .5 mm). The database was computed to an accuracy of 6 significant digits, so as not to lose accuracy during the interpolation process through round-off error. All the lengths and offsets shown in Table 1 are in between these node points and examination of the data reveals that the difference between the exact moment method computed data differ only very slightly from the scattering-parameter data computed from the database. Fig.2 has been included to give a global view of the variation of the magnitude of  $s_{11}$  with the slot parameters  $x_0$  and  $2l$ . We have shown a portion of the  $x_0=3\text{mm}$  dataset in Fig.3, obtained using a decreasing number of nodal points to give some indication of the number needed. The accuracy achievable can easily be increased simply by using more nodes in the database until it is well within that required for design purposes (and certainly up to that accuracy with which slot properties can be measured).

### 3. CONCLUDING REMARKS

The interpolation schemes whose use has been discussed in this paper provide both sufficiently accurate, and rapid, computation of slot data for their use in a slotted waveguide array design code to be viable. Given a set of measured or computed (using accurate moment method techniques) data, node points can be selected in such a way as to obtain sufficient accuracy with as few nodes as possible (and thus interpolate as rapidly as possible).

### REFERENCES

- [1] R.S. Elliott and L.A. Kurtz, "The design of small slot arrays", *IEEE Trans. Antennas Propagat.*, vol. AP-26, pp. 214-219, March 1978.
- [2] R.S. Elliott, "An improved design procedure for small arrays of shunt slots", *IEEE Trans. Antennas Propagat.*, vol. AP-31, no. 1, pp. 48-53, Jan. 1983.
- [3] A.J. Sangster and A.H.I. McCormick, "Theoretical design/synthesis of slotted waveguide arrays", *IEE Proc.*, vol. 136, Part H, no. 1, pp.39-89, Febr. 1989.
- [4] J.J. Gulick and R.S. Elliott, "The design of linear and planar arrays of waveguide-fed longitudinal slots", *Electromagnetics*, vol. 10, no. 4, pp. 327-347, Oct./Dec. 1990.
- [5] R.W. Lyon and A.J. Sangster, "Efficient moment method analysis of radiating slots in a thick-walled rectangular waveguide", *IEE Proc.*, vol. 128, Pt. H, pp. 197-205, Aug. 1981.
- [6] G.J. Stern and R.S. Elliott, "Resonant length of longitudinal slots and validity of circuit representation: theory and experiment", *IEEE Trans. Antennas Propagat.*, vol. AP-33, no. 11, pp. 1264-1271, Nov. 1985.
- [7] L.G. Josefsson, "Analysis of longitudinal slots in rectangular waveguides", *IEEE Trans. Antennas Propagat.*, vol. AP-35, no. 12, pp. 1351-1357, Dec. 1989.
- [8] Y.L. Chua, J.B. Davies and D. M'Irshekar-Syahkal, "An accurate bivariate formulation for computer-aided design of circuits including microstrip", *IEEE Trans. Microwave Theory Tech.*, vol.MTT-31, No.8, pp.685-687, Aug.1983.
- [9] W.H. Press, B.P. Flannery, S.A. Teukolsky and W.T. Vetterling, *Numerical Recipes*, Cambridge University Press, 1989, pp.86-89 and pp.100-101.
- [10] H.Y. Yee, "Impedance of a narrow longitudinal slot in a slotted waveguide array", *IEEE Trans. Antennas Propagat.*, vol. AP-22, pp. 589-592, July 1974.
- [11] E.K.Miller, J.N.Brittingham and J.T.Okada, "Bivariate-interpolation approach for efficiently and accurately modeling antennas near a half space", *Electron. Lett.*, Vol.13, pp.690-691, 1977.

		Data computed with the moment method code				Data computed from database using spline interpolation			
$2\ell$	$x_0$	$ S_{11} $	$\angle S_{11}$	$ S_{21} $	$\angle S_{21}$	$ S_{11} $	$\angle S_{11}$	$ S_{21} $	$\angle S_{21}$
13.2	2.1	.027	76.05	.994	-1.62	.027	76.00	.994	-1.63
14.4	3.4	.104	63.76	.959	-5.93	.104	63.76	.959	-5.93
15.6	3.7	.188	43.46	.874	-9.21	.188	43.46	.874	-9.21
16.8	4.1	.284	15.47	.732	-7.37	.284	15.67	.733	-7.43
17.2	4.8	.337	15.41	.684	-9.85	.337	15.51	.685	-9.87
18.7	5.2	.380	-8.46	.622	0.74	.380	-8.44	.622	0.73

**Table 1:** Comparison between scattering parameter data generated by a moment method code, and data computed from a data base using a spline interpolation routine. (Lengths and offsets given in mm, and phase in degrees).

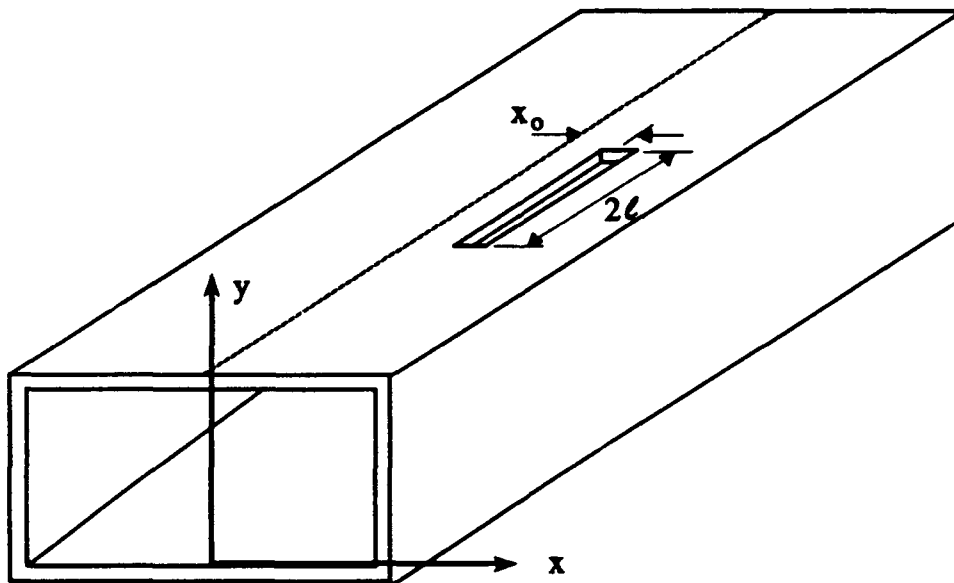


**Figure 1:** Geometry of a longitudinal slot in rectangular waveguide, showing the notation used in the paper.

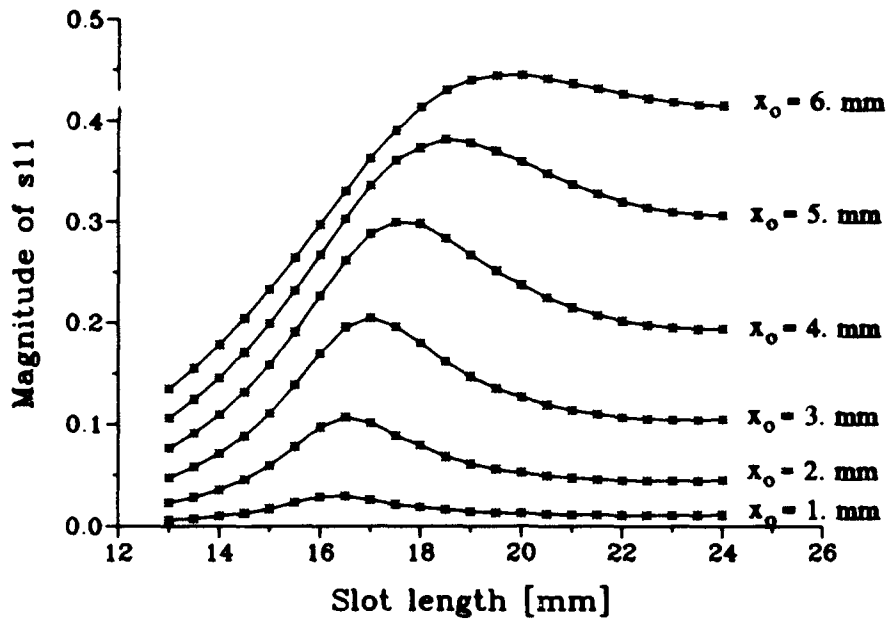


Figure 2: Magnitude of  $s_{11}$ , for varying  $x_0$  and  $2l$ , computed using the moment method.

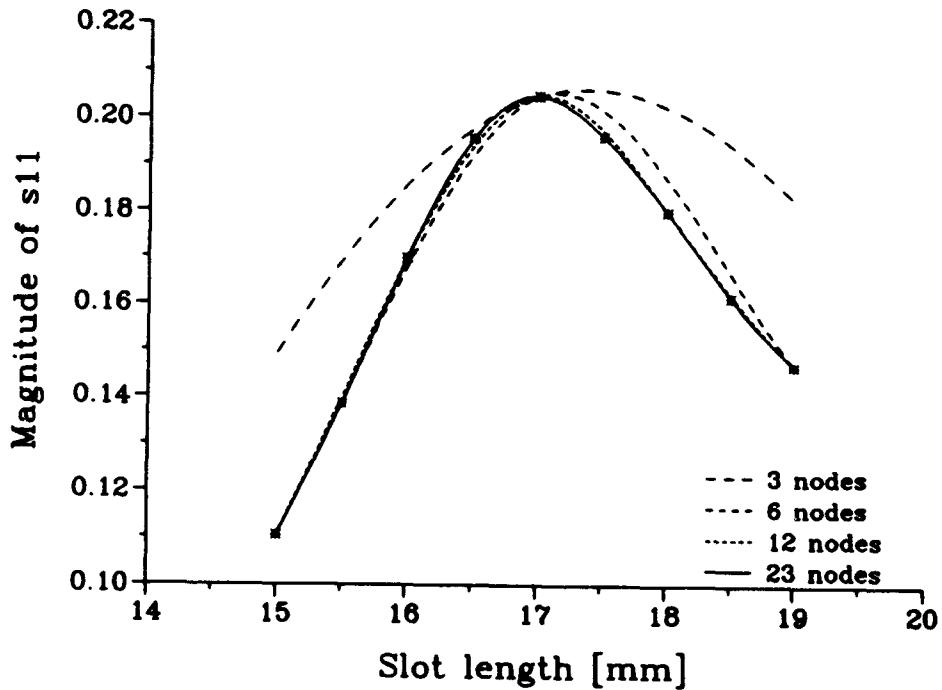


Figure 3: Magnitude of  $s_{11}$ , for  $x_0 = 3$  mm and varying  $2l$ , computed using the spline interpolation procedure with different numbers of nodal points. Some moment method results are shown (\*) for reference.

# A TECHNIQUE FOR DETERMINING NON-INTEGER EIGENVALUES FOR SOLUTIONS OF ORDINARY DIFFERENTIAL EQUATIONS

D. Reuster and M. Kaye

University of Dayton  
Department of Electrical Engineering  
Dayton, OH 45469-0226  
USA

*ABSTRACT: A study of the determination of non-integer eigenvalues for ordinary differential equations with transcendental solutions is presented. An algorithm based on expansion in terms of Chebyshev polynomials and collocation is presented. The method is applied to the problem of computing the electric field external to a biconical radiating structure. Eigenfunction solutions for Legendre's differential equation satisfying the boundary conditions of the problem considered are presented.*

## 1. INTRODUCTION

Canonical analysis of boundary value problems commonly produce series solutions of transcendental functions, [1-3] where the index of summation is a set of eigenvalues ( $\nu$ ) determined by the boundary conditions of the problem. When considering perfectly conducting boundaries, the eigenvalues are those values such that the transcendental function of order  $\nu$ , or its derivative, is equal to zero at the boundaries. Unfortunately, the determination of the eigenvalues that provide such results is usually limited to special cases, often when  $\nu$  is an integer. Difficulty in determining the correct values for  $\nu$ , when  $\nu$  is not an integer, has limited the use of canonical analysis for these problems.

This paper presents a generalized numerical approach for determining the eigenvalues of transcendental functions subject to the Dirichlet and Neumann boundary conditions. The method proposed is based upon expanding the unknown function in a series of Chebyshev polynomials [4] and using the method of collocation [3] to obtain a well conditioned system of linear homogeneous equations. The eigenvalues ( $\nu$ ) are then found by using a bracketing and bisection technique [5].

This paper is organized as follows. Section 2 describes the mathematical formulation of the problem. Section 3 presents the method for numerically computing the eigenvalues. Section 4 presents sample results for Legendre's differential equation, which arises in the canonical analysis of spherical based problems.

## 2. MATHEMATICAL FORMULATION

Assume that the physical problem under consideration is described by the function  $y_v(x)$ , which is defined on the closed region  $[a,b]$ , and satisfies a second order ordinary differential equation (ODE) of the following form:

$$A(x) \frac{d^2 y_v(x)}{dx^2} + B(x) \frac{dy_v(x)}{dx} + C(x,v) y_v(x) = 0 \quad (2.1)$$

The functions  $A(x)$ ,  $B(x)$ , and  $C(x,v)$  are taken to be continuous on the open region  $(a,b)$ . The sought solutions are subject to boundary conditions which can be separated into different types according to the physical problem under consideration. Typical boundary conditions are:

$$y_v(a) = y_v(b) = 0 \quad (2.2)$$

$$y_v'(a) = y_v'(b) = 0 \quad (2.3)$$

$$y_v(a) = y_v'(b) = 0 \quad (2.4)$$

$$y_v'(a) = y_v(b) = 0 \quad (2.5)$$

where  $y_v'(\xi)$  denotes the derivative of  $y_v(x)$  with respect to  $x$ , evaluated at  $x = \xi$ .

Let  $y_v(x)$  be expressed by the following Chebyshev polynomial expansion:

$$y_v(x) = \sum_{n=0}^{\infty} \alpha_n^v T_n[\ell(x)] \quad a \leq x \leq b \quad (2.6)$$

where  $T_n(z)$  is the  $n$ th Chebyshev polynomial of the first kind, and  $\ell(x)$  is a linear mapping which maps the interval  $[a,b]$  to  $[-1,1]$

$$T_n(z) = \cos(n \cos^{-1}(z)) \quad -1 \leq z \leq 1 \quad (2.7)$$

$$\ell(x) = \left[ \frac{2}{(b-a)} \right] x - \frac{2a}{(b-a)} - 1 \quad a \leq x \leq b \quad (2.8)$$

Since the set of Chebyshev polynomials are continuous on  $[-1,1]$ , the first and second derivatives of  $y_v(x)$  may be expressed as follows:

$$\frac{dy_v(x)}{dx} = \sum_{n=0}^{\infty} \alpha_n^v T_n'[\ell(x)] \frac{d\ell(x)}{dx} \quad (2.9)$$

$$\frac{d^2y_v(x)}{dx^2} = \sum_{n=0}^{\infty} \alpha_n^v T_n''[\ell(x)] \left[ \frac{d\ell(x)}{dx} \right]^2 \quad (2.10)$$

$T_n'[\ell(x)]$  and  $T_n''[\ell(x)]$  are the first and second derivatives of  $T_n[\ell(x)]$  with respect to  $\ell(x)$ , and are given by:

$$T_n'(z) = \frac{1}{(1-z^2)} [-nz T_n(z) + n T_{n-1}(z)] \quad (2.11)$$

$$T_n''(z) = \frac{1}{(1-z^2)^2} [ T_n(z) ((nz)^2 - nz^2 - n) + T_{n-1}(z)(-2n^2z + 3nz) + T_{n-2}(z)(n^2 - n) ] \quad (2.12)$$

Substituting Eqs. (2.9) and (2.10) in Eq. (2.1) and approximating the series expansion for  $y_v(x)$  by the first N terms, yields the following linear homogeneous equation for the expansion coefficients ( $\alpha_n^v$ ):

$$\sum_{n=0}^{N-1} M_n^v(x) \alpha_n^v = 0 \quad (2.13)$$

where,

$$M_n^v(x) = A(x) T_n''[\ell(x)] \left[ \frac{d\ell(x)}{dx} \right]^2 + B(x) T_n'[\ell(x)] \frac{d\ell(x)}{dx} + C(x, v) T_n[\ell(x)] \quad (2.14)$$

Enforcing Eq. (2.14) at N points,  $\{x_i, i=1, N\}$ , on the interval  $[a, b]$  leads to a system of N linear homogeneous equations, which may be written as the following matrix equation:

$$\begin{bmatrix} M_0^v(x_1) & M_1^v(x_1) & \dots & M_{N-1}^v(x_1) \\ M_0^v(x_2) & M_1^v(x_2) & \dots & M_{N-1}^v(x_2) \\ \cdot & \cdot & & \cdot \\ \cdot & \cdot & & \cdot \\ \cdot & \cdot & & \cdot \\ M_0^v(x_N) & M_1^v(x_N) & \dots & M_{N-1}^v(x_N) \end{bmatrix} \begin{bmatrix} \alpha_0^v \\ \alpha_1^v \\ \cdot \\ \cdot \\ \cdot \\ \alpha_{N-1}^v \end{bmatrix} = \begin{bmatrix} 0 \\ 0 \\ \cdot \\ \cdot \\ \cdot \\ 0 \end{bmatrix} \quad (2.15)$$

Note that the matrix  $M$  is solely a function of  $v$ , the desired eigenvalues of the given ODE. Since Eq. 2.13 is a homogeneous equation, it will have non-trivial solutions if and only if the determinant of the matrix  $M$  is zero. However, taking the determinant of the matrix  $M$  in its present form yields zero for any value of  $v$ . This is because solutions exist for any given value of  $v$  due to the fact that the boundary conditions have not yet been imposed. Hence, it is necessary to first impose the boundary conditions in order to obtain the desired values for  $v$ .

Boundary conditions are imposed by replacing the first and last rows of the matrix  $M$  with the series representation for the boundary conditions. Thus if,  $y_v(a) = y_v(b) = 0$  the first row of the matrix  $M$  is replaced by

$$\sum_{n=0}^{N-1} \alpha_n^v T_n[\ell(a)] = 0 \quad (2.16)$$

and the last row is replaced by

$$\sum_{n=0}^{N-1} \alpha_n^v T_n[\ell(b)] = 0 \quad (2.17)$$

The new matrix obtained will be denoted by  $\tilde{M}$ . Because the boundary conditions require the function, or the derivative of the function, to be zero at the boundaries, the matrix equation remains homogeneous; thus, non-trivial solutions still exist if and only if the determinant of the matrix  $\tilde{M}$  is zero. Hence, the permissible values of  $v$ , subject to the given boundary conditions, are obtained by requiring  $\det(\tilde{M}) = 0$ .

### 3. COMPUTER IMPLEMENTATION

Numerical estimation of the eigenvalues  $v_p$  ( $p = 1, \dots, P$ ), is based on the fact that the  $\det(\tilde{M})$  is an oscillatory function of  $v$ , with the  $\det(\tilde{M}^{v_p}) = 0$  ( $p = 1, \dots, P$ ). Hence, over any interval containing a single eigenvalue,  $\det(\tilde{M})$  will change sign. This behavior allows the eigenvalues ( $v_p$ ) to be determined using a bracketing and bisection technique [5]. Scanning  $\det(\tilde{M})$  for changes in sign over a given interval on the  $v$  axis, provides the bracketing intervals for the eigenvalues. Care must be taken in selecting a maximum scan distance which is less than the minimum distance between any two adjacent roots. Scan distances which are too large may cause roots to be missed. Once the roots are bracketed the bisection technique may be implemented to compute the particular eigenvalue to the desired degree of accuracy. Since the bisection method requires only the computation of the sign of the determinant, the common problem of numerical over-flow, associated with determinant calculations, is avoided.

### 4. ANALYSIS OF A BICONICAL RADIATING STRUCTURE

The technique developed in section 2. is now applied to Legendre's differential equation which describes the electromagnetic field external to a biconical radiating structure (shown in figure 4.1). It can be shown that, under radiation conditions, the electric fields external to the structure have series solutions of the following form:

$$E_r = \sum_v c_v H_{v+1/2}^{(2)}(kr) L_v(\cos\theta) \quad (4.1)$$

where  $H_{v+1/2}^{(2)}(kr)$  is a modified Hankel function of the second kind, and  $L_v(\cos\theta)$  is an odd Legendre polynomial [6]. Boundary conditions require that  $L_v(\cos\theta_1) = L_v(\cos\theta_2) = 0$ . Thus, it is necessary to determine the eigenvalues whose eigenfunctions satisfy the given boundary conditions. For Legendre's differential equation,  $A(x) = 1-x^2$ ,  $B(x) = -2x$  and  $C(x,v) = v(v+1)$ .

Two different biconical radiating structures were chosen for analysis: Structure 1,  $\theta_1 = 30^\circ$  and  $\theta_2 = 150^\circ$ ; Structure 2,  $\theta_1 = 10^\circ$  and  $\theta_2 = 170^\circ$ . Tables I and II provide the first four eigenvalues for each structure and compares the calculated eigenvalues with the eigenvalues estimated by Grimes using an asymptotic expansion technique [7]. Graphs of the corresponding eigenfunctions are shown in figures 4.2 and 4.3. For both radiating structures under study, coverage of the calculated eigenvalues occurred for matrix sizes on the order of  $N = 50$  to  $60$ .

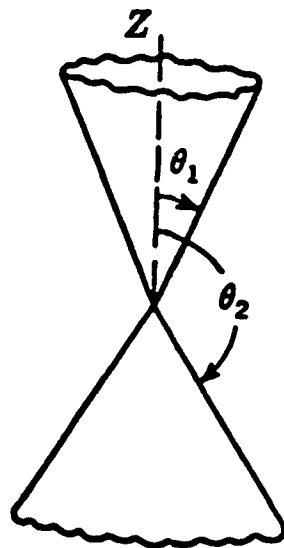


Figure 4.1 Geometry of the biconical radiating structure

TABLE I  
Structure 1  $\theta_1 = 30^\circ$ ,  $\theta_2 = 150^\circ$

Eigenvalue	Calculated Value	Grimes' Result
nu-1	2.439211	2.439211
nu-2	5.466996	5.466996
nu-3	8.477510	8.477309
nu-4	11.482784	-

TABLE II  
Structure 2  $\theta_1 = 10^\circ$ ,  $\theta_2 = 170^\circ$

Eigenvalue	Calculated Value	Grimes' Result
nu-1	1.621407	1.620624
nu-2	3.916836	3.915488
nu-3	6.188799	6.187171
nu-4	8.451585	8.450112

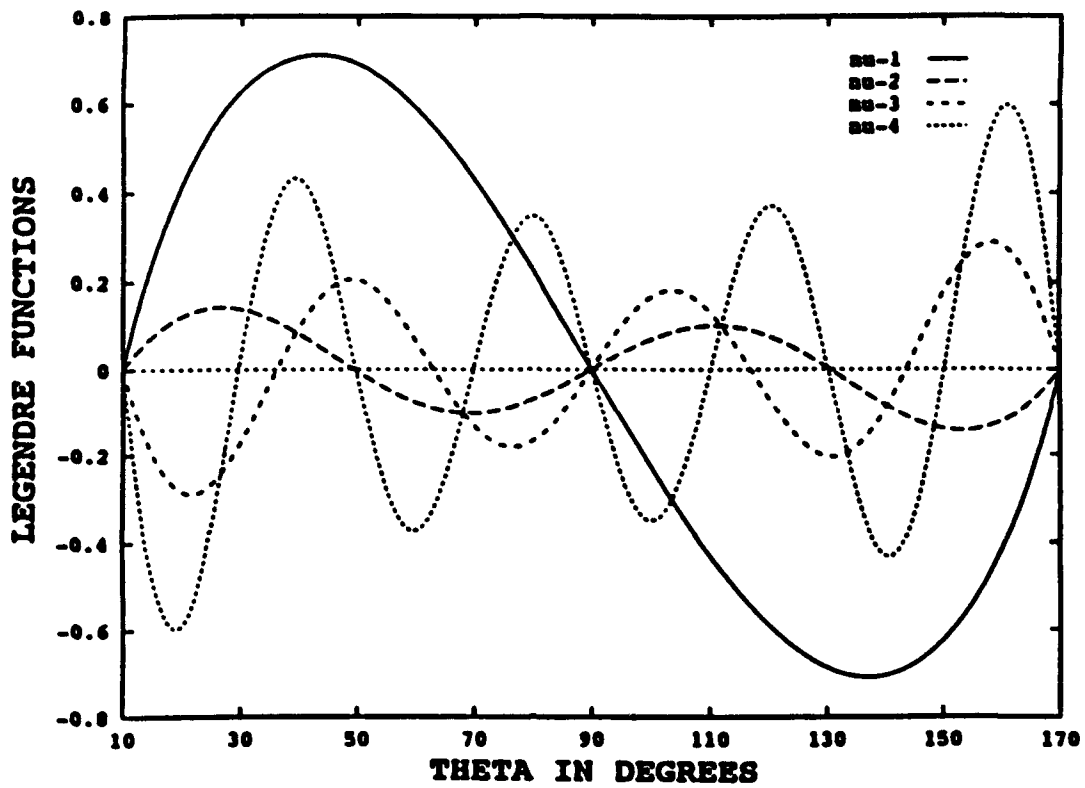


Figure 4.2 First four Legendre functions (eigenfunctions) for  $10^\circ$  biconical structure ( $\theta_1 = 10^\circ, \theta_2 = 170^\circ$ )

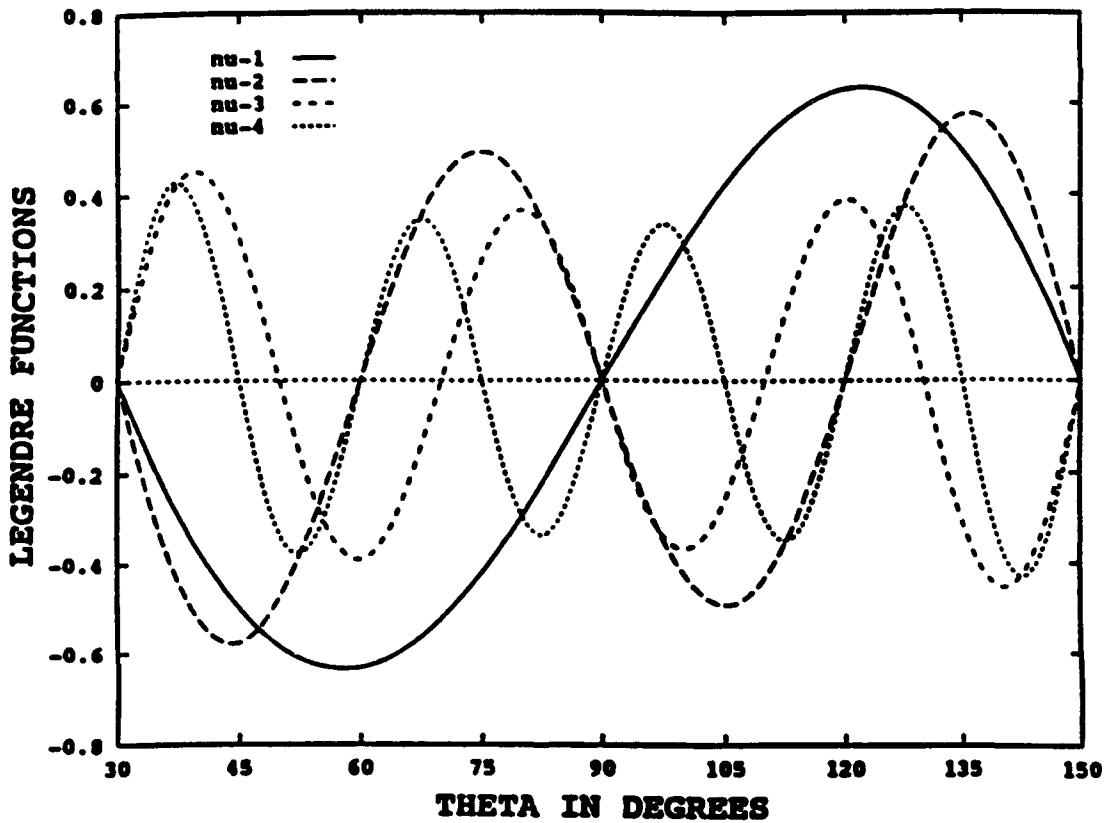


Figure 4.3 First four Legendre functions (eigenfunctions) for  $30^\circ$  biconical structure ( $\theta_1 = 30^\circ, \theta_2 = 150^\circ$ )

## 5. CONCLUSIONS

A generalized technique for determining non-integer eigenvalues for ordinary differential equations with transcendental solutions has been presented. To verify the technique, the method was applied to a biconical radiating structure and the computed eigenvalues were compared with results obtained by Grimes using an asymptotic method. Excellent agreement was established between the two methods. The method proposed here is completely general and has the advantages that only the sign of the determinant needs to be computed and that the matrix size needed for convergence is small.

## ACKNOWLEDGEMENT

The authors would like to thank Dr. Warren Perger for the use of his hypergeometric evaluator program [8] which was used for generating the numerical values of the eigenfunctions.

## REFERENCES

1. S.A. Schelkunoff and H.T. Friis, Antennas Theory and Practice, (John Wiley and Sons, New York, 1952).
2. R.F. Harrington, Time-Harmonic Electromagnetic Fields, (McGraw-Hill Book Co., New York, 1961).
3. D.S. Jones, The Theory of Electromagnetism, (Pergamon Press, New York, 1964).
4. T.J. Rivlin, The Chebyshev Polynomials (John Wiley and Sons, New York, 1974).
5. W.H Press, B.P. Flannery, S.A. Teukolsky and W.T. Vetterling, Numerical Recipes, (Cambridge University Press, New York, 1990), p. 243.
6. J.R. Wait, Electromagnetic Radiation for Conical Structures, in Antenna Theory, Part I, edited by R.E. Collin and F.J. Zucker (McGraw-Hill, New York, 1969), Chapter 12.
7. D.M. Grimes, Biconical receiving antenna, *J. Math. Phys.* 23, 897, 1982.
8. M. Nardin, W.F. Perger and A. Bhalla, Numerical evaluation of the confluent hypergeometric function for complex arguments of large magnitudes, *J. Comput. Appl. Math.* 39, 193, 1992.

# ANTENNA MODELING AND CHARACTERIZATION OF A VLF AIRBORNE DUAL TRAILING WIRE ANTENNA SYSTEM

J. K. Breakall

Department of Electrical and Computer Engineering  
The Pennsylvania State University  
University Park, PA 16802

D. H. Werner and R. J. Lunnen  
The Applied Research Laboratory  
The Pennsylvania State University  
P. O. Box 30  
State College, PA 16804

## Abstract

This paper describes the electrical characterization of the Very Low Frequency (VLF) dual trailing wire antenna systems associated with Navy aircraft used for communications to underwater Navy assets. The static wire geometry with the aircraft in orbit was obtained using a modified version of the program WIRE3, which models the mechanical parameters of the dual trailing wire antenna. The Numerical Electromagnetics Code (NEC) was used to model all electrical characteristics of the VLF dual trailing wire systems associated with the typical TACAMO aircraft. Antenna parameters such as current distribution, input impedance versus frequency, effective radiated power, and the effect of antenna wire conductivity were evaluated. It is demonstrated that the computer codes provide results which are consistent with measured values of static antenna electrical parameters.

## I. Introduction

The Numerical Electromagnetics Code (NEC) was utilized to computer model the electrical characteristics of the VLF dual trailing wire transmitting antenna system, which consists of both a long and a short trailing wire [1]. A drogue is attached to the far end of the LTWA which causes the wire to be as vertical as possible. A drogue is also attached to the end of the STWA in order to provide stability. A measure, called verticality, is defined as the ratio of the projection of the wire on the Z-axis to the total length of the wire. Verticality is given in terms of a percentage, and the higher the number, the better for coupling into the earth-ionosphere waveguide for propagation. The wire shape geometries of the long trailing wire antenna (LTWA) and the short trailing wire antenna (STWA) were determined using the programs WIRE4NEC and STWANEC, respectively [2]. These are steady-state mechanical codes which provide piecewise wire segments for data input to NEC. The following antenna characteristics have been obtained for this system: current distribution, input impedance versus frequency, and efficiency. The computed antenna input impedance is compared to measured values for eight actual flights.

## II. Static Characterization of the Dual Trailing Wire Antenna

A steady-state mathematical model, which computes the spatial configuration and tension along an orbiting LTWA, was originally developed at the Naval Air Development Center (NADC), Warminster, PA [3]. This model involved the numerical solution of a system of three coupled ordinary differential equations which describe the position of the LTWA with respect to a cylindrical coordinate system. The numerical technique used to evaluate this system of differential equations was later improved by others at NADC and the improved version of their code was given the name WIRE3 [4]. A corrected and modified version of the WIRE3 code was then created for use with NEC in the work reported here and was given the name WIRE4NEC. The WIRE4NEC code writes a file containing a set of NEC compatible geometry inputs.

A brief summary of input parameters necessary to run WIRE4NEC follows. All input parameters are contained in a data file called WIREIN.DAT:

- Line 1    Number of runs to be executed (integer number)
- Line 2    Run title (20 characters)
- Line 3    True airspeed (kts), aircraft orbit radius (ft), aircraft altitude (ft), number of wire increments (integer number), step size (integer number), output flag (0 for trouble shooting, 1 for formatted output).
- Line 4    Estimated separation between the aircraft and the drogue (ft), range of estimated separation (ft).
- Line 5    Drogue weight (lbs), drogue diameter (ft), coefficient of drag of the drogue.
- Line 6    Wire density (lbs/ft), wire diameter (ft), wire length (ft), coefficient of friction of the wire, coefficient of drag of the wire.

Lines 2-6    are repeated for multiple runs.

The WIRE4NEC program evaluates the wire model at five different separation cases between the aircraft and the drogue. The program will stop iterating at each separation case after 31 iterations or if the solution converges so that the antenna feed endpoint, known as LTWA distance, is within 100 feet of the aircraft. Generally, it requires the full number of iterations for the program to converge to a solution. In order to test the sensitivity of NEC to the endpoint of the LTWA, solutions less than 100 feet were accepted.

Several models were considered for the short trailing wire antenna (STWA). The first model treated the STWA as remaining in the plane of the flight path. Two cases for this assumption were analyzed: STWA tangential to the radius of the flight path, and the STWA along the circumference traced by the flight. Both models provided only marginal results. Next, the wire was allowed to drop at a constant angle with respect to horizontal,

resulting in an improvement over the previous models. Finally, a code called STWANEK was developed which determines the steady-state geometry of the STWA for input to NEC. The STWANEK program numerically solves a system of coupled ordinary differential equations which represent the mechanical forces on the antenna. A fourth-order Runge-Kutta technique was used. A complete description of the mechanical model for the STWA is beyond the scope of this work [2].

### III. NEC Modeling and Results

Determining the geometry of the Long Trailing Wire Antenna (LTWA) and the Short Trailing Wire Antenna (STWA) of the dual trailing wire system is done using the two aforementioned programs WIRE4NEK and STWANEK. Both of the programs utilize various flight data in order to predict the STWA and LTWA positions. Some of the parameters that are used in both programs include: true air speed, aircraft orbit radius, aircraft altitude, estimated separation between aircraft and drogue, and drogue weight. Based on all the parameters, the program determines the verticality of the wire and the separation of the predicted wire endpoint from the aircraft. In addition, the geometry inputs for use in NEC are produced. By merging the outputs from these two programs, the entire geometry of the two trailing wires is obtained.

Although using the outputs of WIRE4NEK and STWANEK yields the basic geometry of the long and short wires in a NEC format, the simple concatenation of the two files does not produce the final form of the model. Each section of the antenna must be analyzed in order to add the correct amount of segment length tapering near the feed point. It is also necessary to move the short wire so that it is connected to the endpoint of the long wire/feed section using the NEC "move" and "translate" input. After this movement, the short wire is rotated to make it tangential to the circumference of the flight path using the NEC "rotate" input.

To obtain accurate results from the model, the wire segment lengths near the feedpoint must be tapered. An algorithm has been developed to calculate the adjacent segment length ratios and the number of segments for both the long and short wires. The modeling approach is to choose very short segments near the critical feedpoint region and then to smoothly taper outward along the wires from this feedpoint. The process provides excellent detail at the feed point as well as throughout the entire antenna structure. Figure 1 shows the top view and Figure 2 shows a side view of the NEC wire segmentation used for the dual trailing wire antenna shown in Figure 3. The tapering algorithm and its implementations will now be described.

NEK has an option for tapering either the length or radius of adjacent segments on a straight wire. It requires as an optional input the ratio of the length of a segment to the length of the previous segment in the wire. It also requires the radius of the first segment and the last segment if stepped radius tapering is desired. For the work described in this paper only length tapering of the segments was required which will be discussed in the following.

In the method used in NEC, once given the end coordinates of the wire, the number of segments,  $N_s$ , and the adjacent ratio factor,  $R_\Delta$ , one can calculate the length of the first segment,  $S_1$ , as:

$$S_1 = L(1-R_\Delta)/(1-R_\Delta^{N_s}) \quad (1)$$

where  $L$  is the total length of the straight wire. If the ratio factor equals 1, then

$$R_\Delta = 1. \quad (2)$$

which implies

$$S_1 = L / N_s \quad (3)$$

which is the normal case of the wire being divided up into a total of  $N_s$  equal length segments.

A more useful and desirable approach to this segment tapering problem is to choose the first segment length,  $L_1$ , and the last segment length,  $L_{N_s}$ , and with these parameters compute the number of segments,  $N_s$ , and the adjacent segment ratio factor,  $R_\Delta$ , given the total length of wire,  $L$ . If the computed  $R_\Delta$  is less than a factor of 2 or some other modeling guideline criterion, then this  $R_\Delta$  can be used.

There have been some attempts at this problem [5] using an iterative solution of (1). This method is time consuming and unnecessary because there exists an exact analytical solution for this problem which will be described. The last segment,  $S_{N_s}$ , is

$$S_{N_s} = S_1 R_\Delta^{N_s-1} \quad (4)$$

This can be rewritten and solved for  $N_s$  as

$$N_s = \frac{\log(S_{N_s} / S_1)}{\log R_\Delta} + 1 \quad (5)$$

Since  $N_s$  is an integer, one must take the nearest integer of this expression when programming. Substituting (4) into (1), rearranging and solving for  $R_\Delta$  gives

$$R_\Delta = \frac{(S_1 - L)}{(S_{N_s} - L)} \quad (6)$$

A FORTRAN program has been written incorporating the above equations and was used in the modeling discussed in this paper.

The final STWA geometry model was determined using the steady-state mechanical code called STWANEC discussed above. This model resulted in a curved drop for the STWA. Furthermore, the wire dropped such that it was tangential to the flight path circumference. The final form for the model can be seen in Figure 3 which plots the LTWA and STWA geometries from different aspect angles. Using this final form, excellent agreement was obtained with respect to the measured data. A comparison of the computed impedances using the simple arc and the final form versus the measured data is seen in Table 1 [6].

Figure 4 shows the calculated current distribution on the LTWA and STWA for the 22 kHz test case (title for this case is given as 08:0322:90 VAL). Both amplitude and phase of the current distribution are shown. Labels on the plot list the various aircraft parameters used in the calculation. Analysis of the results for the amplitude of the current distribution shows that the amplitude is peaking at 60 Amps. This peak occurs at an arc length of about 11,000 feet, which is about half of the distance from the drogue to the feed point.

**Table 1. STWA Geometry Effects on Impedance**

FREQUENCY (KHZ)	RUN TITLE	IMPEDANCE		
		MEASURED	NEC STWA ARC	NEC STWA MODEL
22	08:0322:90VAL	600-j350	712-j267	647-j399.8
WIRE DC RESISTANCE = 4.5 OHMS/1000 FT				

Figure 5 compares the NEC calculated current distribution for the 22 kHz test case with a pure sinusoidal current distribution. The calculated current distribution was normalized to a maximum value of 1 for comparison purposes. This figure demonstrates that the calculated current distribution is in general agreement with the classical sinusoidal current distribution approximation. However, there are some slight deviations at the feed point and towards the drogue end of the LTWA.

Table 2 is a comparison of measured versus calculated input impedance for the various runs. Figure 6 is a comparison of the measured and calculated input impedances over frequency. Both the real and imaginary parts of the impedance are displayed. The imaginary part is negative while the real part is positive.

The calculated impedance data agrees well with the measured data. The close agreement between the measured and calculated impedances provides further evidence that the NEC model is closely simulating the actual dual trailing wire antenna system.

**Table 2. Measured Versus Calculated Input Impedance**

FREQUENCY (KHZ)	RUN TITLE	LTWA DIST	LTWA VERT	STWA VERT	MEASURED IMPEDANCE	NEC IMPEDANCE
22	08:0322:90VAL	31.41	69.81	30.66	600-j350	647-j399.8
22	08:0322:90VAL	85.32	70.76	30.66	600-j350	654.8-j396.9
18	08:03182:90VAL	40.42	72.89	29.67	450-j525	642-j525
17	09:2417:90VAL	37.30	68.41	27.73	480-j525	665.3-j491
19	09:2419:90VAL	88.18	70.99	29.66	600-j490	665.4-j459.4
20	09:2420:90V(B24)	46.23	68.18	29.75	650-j490	674.6-j437.4
20	09:2420:90V(B24)	55.87	69.94	29.75	650-j490	690.4-j432.2
20	09:2420:90V(E48)09:2	19.11	69.98	30.28	550-j350	672.1-j433.1
20	420:90V(E48)	73.81	70.85	30.28	550-j350	679.6-j430.6
20	09:2420:90V(E48)	83.97	68.26	30.28	550-j350	657.9-j438.9
21	09:2421:90VAL	74.02	66.78	30.09	670-j480	649-j423.3

One of the options provided in the NEC code is the ability to model lossy wire antennas. NEC uses an exact expression for the skin effect resistance and internal reactance in ohms/meter. An approximation for the skin effect resistance which has been used at moderately low frequencies where the current is constant throughout the wire cross section is [7]:

$$R = \frac{1}{\pi r_0^2 \sigma} \left[ 1 + \frac{1}{48} \left( \frac{r_0}{\delta} \right)^4 \right] \quad (7)$$

where

- $r_0$  = radius of wire
- $\sigma$  = wire conductivity
- $\delta$  = skin depth

At HF frequencies a better approximation can be given for both the real and imaginary parts of internal impedance of a round wire as:

$$Z_{HF} = \frac{R_s(1 + j)}{2\pi r_0} \quad (8)$$

where

$$R_s = \frac{1}{\sigma \delta} = \sqrt{\frac{\pi f \mu}{\sigma}} \quad (9)$$

and

$f$  = frequency  
 $\mu$  = permeability

A more accurate expression for the internal impedance of a round wire is found from evaluating expressions of the total current in the wire and the magnetic field at the surface of the wire. The magnetic field can be obtained from the electric field via Maxwell's Equations:

$$\nabla \times \bar{E} = -j\omega\mu\bar{H} \quad (10)$$

Expressions can be derived for  $H_\phi$  in terms of Bessel functions. The internal impedance per unit length can then be found from the ratio of the tangential component of the electric field at the surface of the wire divided by the total current in the wire:

$$Z_i = - \frac{T J_0(T r_0)}{2\pi r_0 \sigma J_0'(T r_0)} \quad (11)$$

where  $T = j^{-1/2} \sqrt{\omega \mu \sigma}$   
 $= j^{-1/2} \sqrt{2} / \delta$

This complex internal impedance can be separated into real and imaginary parts using identities of Bessel functions resulting in Kelvin functions.

$$Z_i = \frac{jR_s}{\sqrt{2} \pi r_0} \left[ \frac{\text{Ber } q + j\text{Bei } q}{\text{Ber}' q + j\text{Bei}' q} \right] \quad (12)$$

where  $q = \frac{\sqrt{2} r_0}{\delta}$  and the following identities:

$$\text{Ber } v + j\text{Bei } v = J_0(j^{-1/2} v) \quad (13a)$$

$$\text{Ber}' v + j\text{Bei}' v = \frac{d}{dv} (\text{Ber } v + j\text{Bei } v) = j^{-1/2} J_0'(j^{-1/2} v) \quad (13b)$$

NEC incorporates these exact expressions in the determination of wire conductivity skin effect.

Table 3 is a comparison of NEC calculated input impedance, loss resistance and efficiency for various antenna configurations. The first configuration listed is for a half-wave vertical dipole at an altitude of 20,500 feet over perfectly conducting ground. It is offset fed in the same manner corresponding to the STWA and LTWA of example 08:0322:90 VAL. The parameters are: LTWA = 19,500 feet, STWA = 2680 feet, frequency = 22kHz, and wire resistance = 4.5Ω/1000 ft. This case would correspond to an antenna with a verticality of 100% and offset fed. Shown also is the same vertical dipole offset fed assuming perfectly conducting wire, lossless case. The loss resistance can therefore be computed from the difference of the real part of the impedance for the two cases as well as an efficiency factor given by

$$\eta = \frac{R_{lossless}}{R_{lossy}} \quad (14)$$

Also shown are results for a center fed vertical halfwave dipole which is the same antenna as the offset case. The results are for over perfectly conducting ground and in free space for both lossy and perfectly conducting wire. The last result is the model for the dual trailing wire antenna system. The efficiency of the 22 kHz test case dual trailing wire antenna was found to be 47%, assuming a known wire DC resistance of 4.5 ohms/1000 feet. This suggests that nearly half of the power input to the antenna is being dissipated as heat.

#### IV. Conclusions

This paper has shown the application and validity of using the Numerical Electromagnetics Code for the modeling of the VLF aircraft dual trailing wire antenna system. A description was given of the approach of performing mechanical modeling of the steady-state shape geometry of the dual trailing wire antenna composed of the LTWA and STWA. Software has been written to convert these wire shapes into NEC geometry input data involving tapering of the wire segment lengths to achieve high accuracy. Figure 7 summarizes the procedures and various computer codes which have been used to obtain results in this work.

Comparisons have been made to actual experimental measurements of antenna feedpoint impedance with excellent agreement to computed results. Efficiencies have been calculated from various modeled results using exact formulations of wire conductivity effects.

These results are important in that the current distributions as computed can be input to an additional code, TWIRENEC, which computes VLF propagation in the earth-ionosphere waveguide [8]. Additionally, similar modeling can be performed with dynamic mechanical models of the wires to obtain the variations of all antenna characteristics (impedance, currents, and radiation fields) versus time, corresponding to the mechanical motions versus time.

**Table 3. Efficiency of Wire Antenna (22 kHz)**

ANTENNA CONFIGURATION	IMPEDANCE		LOSS RESISTANCE	EFF (%)
HALF-WAVE VERTICAL DIPOLE OVER GROUND (OFF-SET FEED)	1150-j85 (LOSSY)	724-j46 (LOSSLESS)	426	63%
HALF-WAVE VERTICAL DIPOLE OVER GROUND (CENTER FED)	157+j70.8 (LOSSY)	99.3+j50.5 (LOSSLESS)	57.7	63%
HALF-WAVE DIPOLE (FREE-SPACE) (CENTER FED)	133.7+j68.1 (LOSSY)	76.6+j47.2 (LOSSLESS)	57.1	57%
DUAL TRAILING WIRE	647-j399.8 (LOSSY)	303.8-j386.0 (LOSSLESS)	343.2	47%
WIRE DC RESISTANCE = 4.5 OHMS/1000 FT				

### Acknowledgements

The authors wish to thank J. D. Carlson, T. A. Erdley, J. S. Young, and J. A. Huffman for modeling and computer programming assistance. This work was supported by the TACAMO Aircraft Programs Office, PMA 271, under contract number N00039-88-C-0051.

### References

1. Burke, G. J., and A. J. Poggio, "Numerical Electromagnetics Code (NEC) - Method of Moments," Naval Ocean Systems Center Technical Document No. 116, prepared by Lawrence Livermore Laboratory for the Naval Ocean Systems Center and Air Force Weapons Laboratory, July 1977.
2. Breakall, J. K., D. H. Werner, R. J. Lunnen, J. D. Carlson, T. A. Erdley, and J. S. Young, "Navy Aircraft for Underwater Communications - Antenna System Modeling and Characterization," TACAMO Interim Report, Applied Research Lab., The Pennsylvania State University, Jan. 25, 1991.
3. Huang, S. L., "Mathematical Model for Long Cable Towed by Orbiting Aircraft," Naval Air Development Center Report No. NADC-AM-6849, Warminster, PA, June 1969.

4. NADC Letter Code 40L, Forwarding of WIRE3 Program and Related User Instructions, 20 February 1990.
5. Adler, R. W., Naval Postgraduate School, Private Communication.
6. Nathans, D., "TACAMO Dual Trailing Wire Antenna Input Impedance Measurements and Antenna Simulator Design," Naval Air Development Center Report No. 87040-40, Final Report No. A511-5114/001-F/5PME11000, Warminster, PA 18974, 19 December 1986.
7. Ramo, W. and V. Duzer, "Fields and Waves in Communication Electronics," John Wiley & Sons, New York, 1965.
8. Werner, D. H., J. K. Breakall, and R. J. Lunnen, "Propagation of VLF Radiation in the Earth-Ionosphere Waveguide Excited by an Airborne Dual Trailing Wire Antenna," *Applied Computational Electromagnetics Society Journal*, Vol. 8, No. 2, pp. 72-92, 1993.

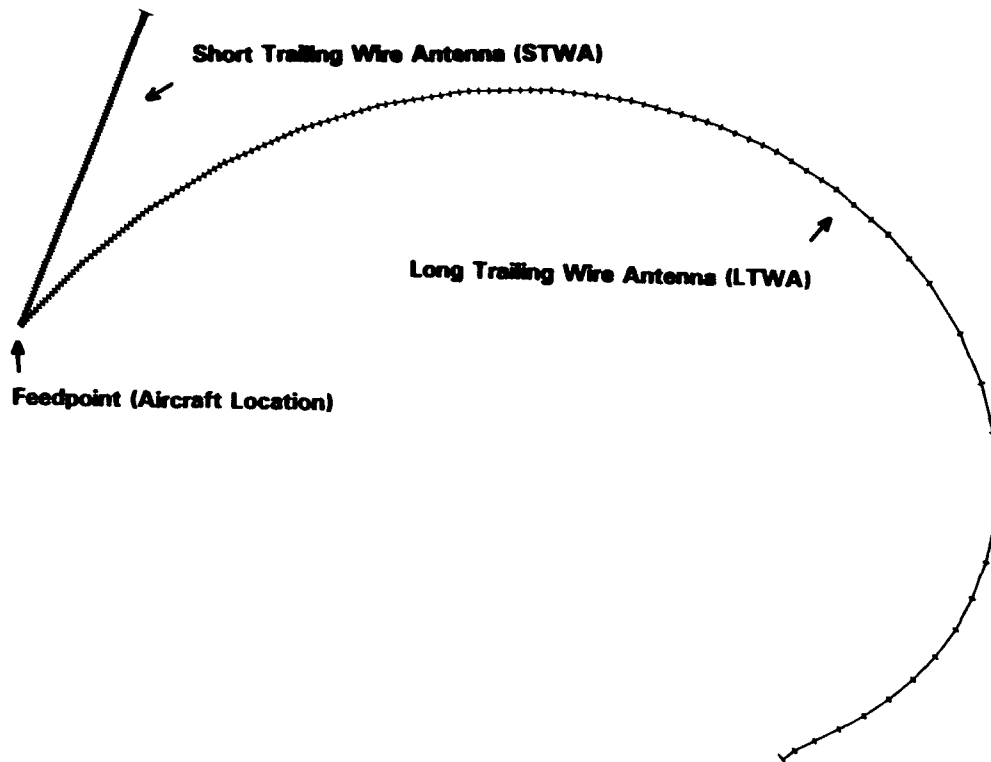


Figure 1. Top View Showing the NEC Wire Segmentation Geometry for the 22 kHz Test Case.

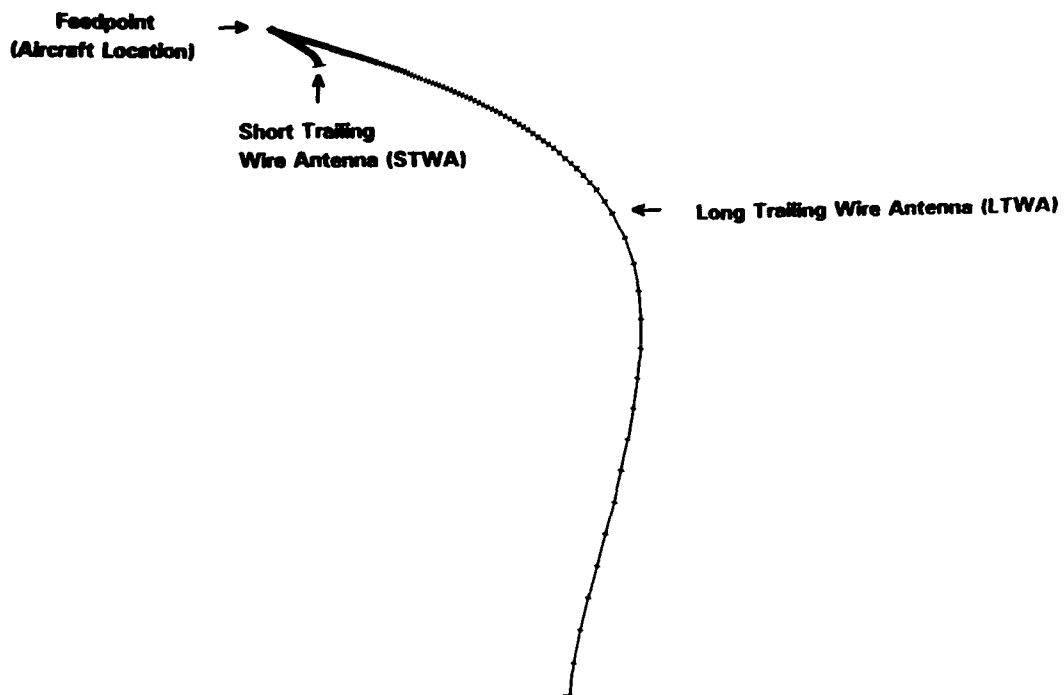
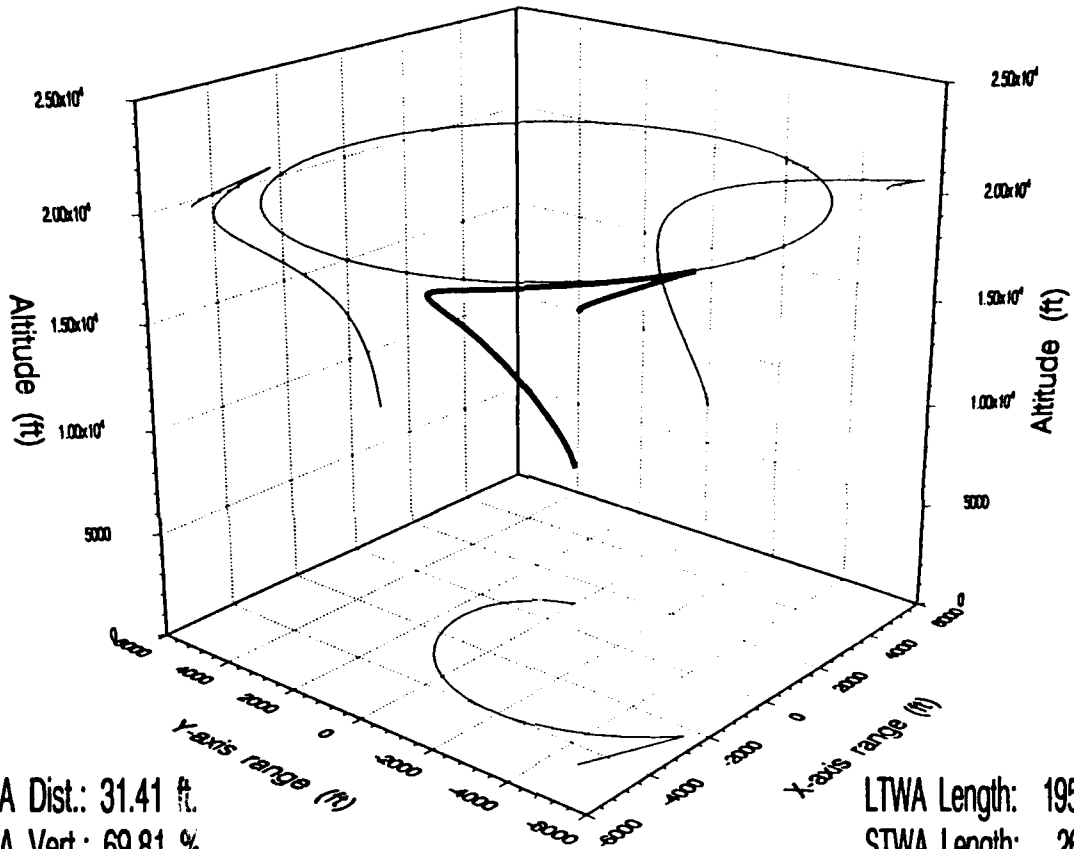


Figure 2. Side View Showing the NEC Wire Segmentation Geometry for the 22 kHz Test Case.

**LTWA AND STWA GEOMETRY WITH ORBIT**  
 File: 08:0322:90VAL Freq: 22 KHz



LTWA Dist.: 31.41 ft.  
 LTWA Vert.: 69.81 %  
 STWA Vert.: 30.66 %

LTWA Length: 19500 ft.  
 STWA Length: 2680 ft.  
 Altitude: 20500 ft.

Figure 3. Steady-State Dual Trailing Wire Antenna Geometry for a 22 kHz Test Case.

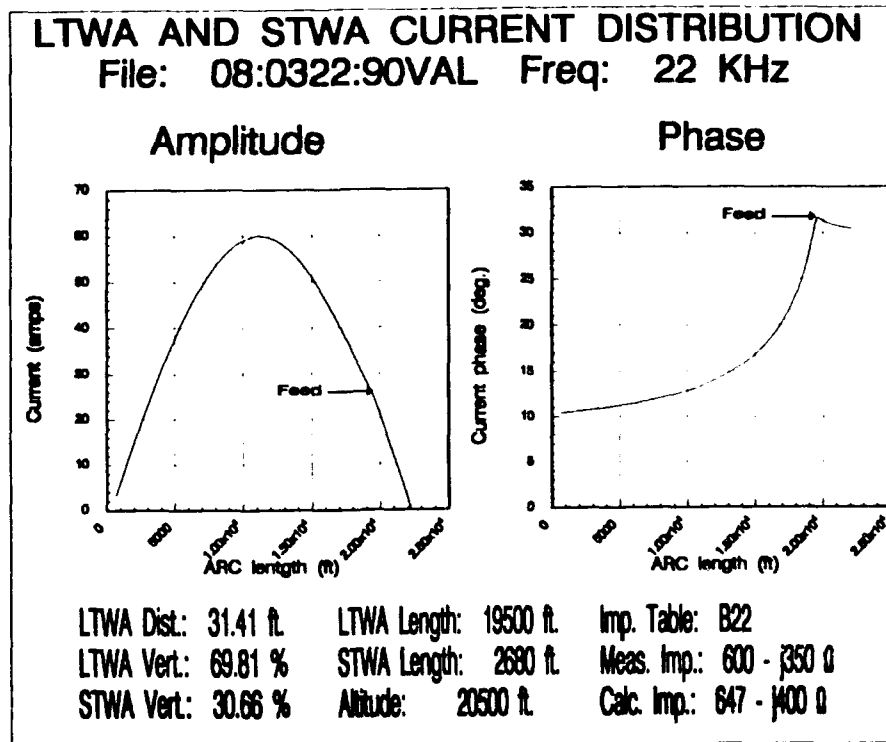


Figure 4. NEC Calculated Current Distribution Resulting From the 22 kHz Test Case of Figure 3.

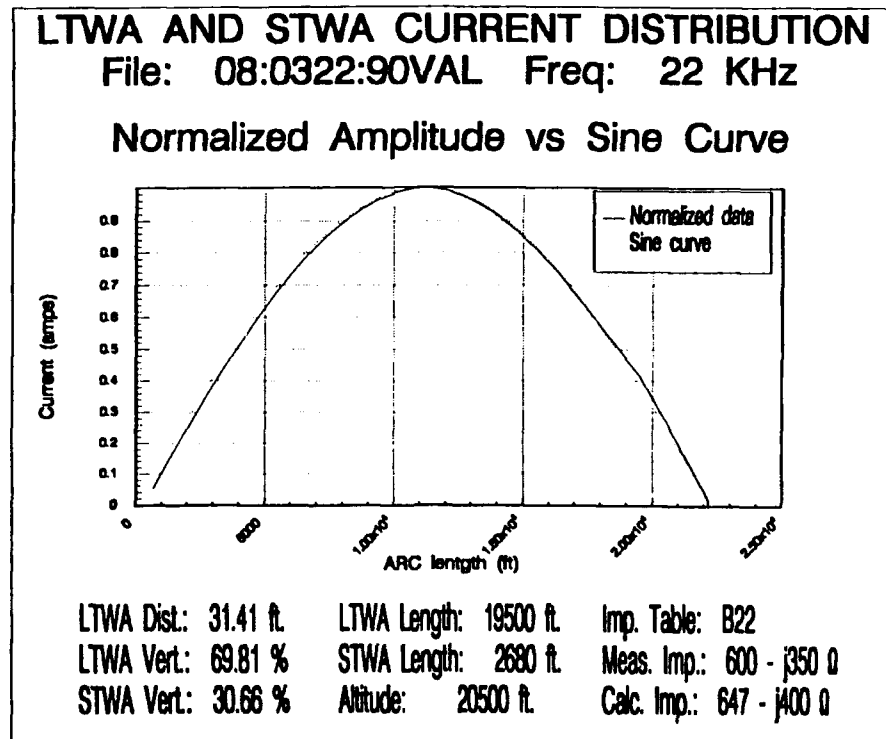


Figure 5. Normalized NEC Calculated Current Amplitude From Figure 4 Compared to a Sinusoidal Current Distribution.

## TACAMO ANTENNA IMPEDANCE Measured vs Calculated

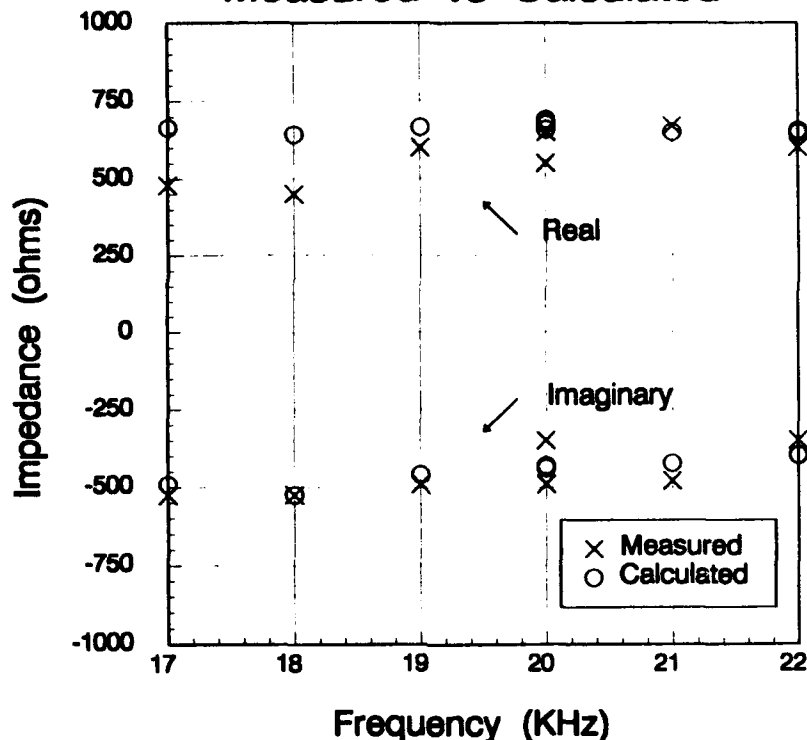


Figure 6. Measured Versus NEC Calculated Input Impedance (Real and Imaginary Parts) for the Validation Runs of Table 2.

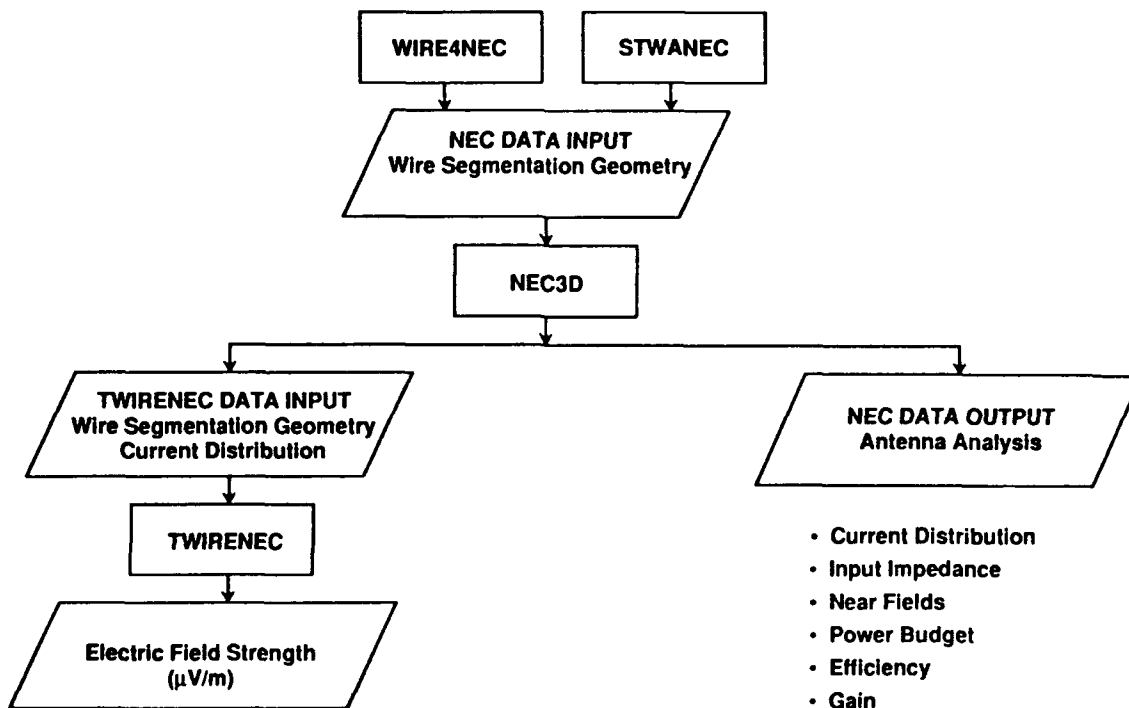


Figure 7. Flowchart showing the Interrelationship Between the Program Modules.

# ELECTROMAGNETIC SCATTERING FROM TWO-DIMENSIONAL COMPOSITE OBJECTS

Ahmed A. Kishk and Paul M. Goggans  
Department of Electrical Engineering  
University of Mississippi  
University, MS 38677

**ABSTRACT.** *Different surface integral equations are presented for two-dimensional composite objects. The objects consist of impedance bodies partially coated with dielectric materials. In all of the formulations, the impedance boundary condition is applied on the impedance surface to reduce the matrix size in the numerical solution. The integral equations are reduced to a system of linear equations via the point matching technique. Application of the point matching technique is straight forward for two dimensional objects. Because of this surface discontinuities can be treated easily without the problems encountered when using triangle basis functions as a result, consideration of two-dimensional objects gives a clear picture of the accuracy that can be obtained using these formulations. Two of the formulations discussed herein overcome the problem of internal resonance. The numerical solutions are verified either by comparison with the analytical solutions for cylindrical objects or by applying self consistency tests for targets without analytical solutions.*

## 1 INTRODUCTION

Recently, interest has been renewed in using the impedance boundary conditions (IBC) in the solution of electromagnetic scattering problems. Use of the IBC can simplify the solution of the many complex electromagnetic problems for which it is valid. However, composite objects of complex structure, in terms of both material type and geometry, are difficult to treat using the IBC because the IBC is often not valid on all object surfaces. Using the exact boundary conditions to solve these problems is uneconomical and requires complicated programming when compared to a method incorporating the IBC.

The IBC is a valid approximation under certain conditions [1-4]. The problem of extending the IBC for use on surfaces where use of the standard IBC would usually be considered questionable has been investigated to some extent. Generalized impedance boundary conditions were proposed in [5] and [6] for this purpose. Unfortunately, use of these generalized impedance boundary conditions comes at the expense of considerable analytical complications and

requires specialized researchers to treat each new geometry.

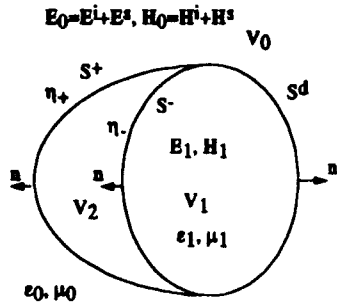
An alternative to using generalized impedance boundary conditions is to use the usual IBC only on surfaces where it is valid. Since IBC is a localized approximation, it can be used on surfaces where it is valid and the exact boundary conditions can be used on the rest of the object [7]. In a practical sense, the IBC can be used for any surface type for which the surface impedance can be determined. In cases of rapid spatial variation of the surface impedance, knowledge of the derivative of the surface impedance is also required. In numerical solutions the surface impedance must be slowly varying to allow for proper piecewise approximation on the surface segmentation. The idea of using both the impedance boundary condition and the exact boundary conditions in a single formulation leads to a technique that is both accurate and efficient.

In this paper such a technique is implemented for two-dimensional (2D) scatterers. Here, four different surface integral formulations are implemented for two-dimensional problems. The method of moments using the point matching technique is then used to reduce the integral equations to matrix equations. The separation of the two transverse polarizations in the 2D problem and the ability to easily implement point matching in the numerical solution of the 2D problem (and so to treat surface discontinuities) will lead to a more complete understanding of the limitations imposed on this technique than is possible with three-dimensional implementations.

## 2 FORMULATION

Consider the general geometry of a two-dimensional scatterer consisting of an impedance body that is partially coated with dielectric as illustrated in Fig. 1. The impedance body has known surface impedance and the dielectric coating is linear, isotropic, and homogeneous. For this geometry, there are three distinct regions:  $V_2$  constituting the impedance body, characterized by surface impedance  $\eta_c$ ;  $V_0$ , the exterior of the scatterer, characterized by the permittivity and permeability of the free space ( $\epsilon_0$ ,  $\mu_0$ ); and

$V_1$ , the dielectric region, characterized by the permittivity and permeability  $(\epsilon_1, \mu_1)$ . The excitation is an



Original Problem

Fig. 1 Geometry of the Original Problem

electromagnetic plane wave of incident fields  $E^i$  and  $H^i$ . The total electric and magnetic fields in region  $V_0$  are denoted by  $E_0$  and  $H_0$ , respectively. In  $V_2$  the total fields are not of interest and have therefore been assumed to be zero for convenience. The region  $V_1$  is bounded by  $S^-$ , the boundary surface between  $V_1$  and  $V_2$ , and  $S^d$ , the boundary surface between  $V_1$  and  $V_0$ . The region  $V_0$  is bounded by  $S^+$ , the boundary surface between  $V_0$  and  $V_2$ , and  $S^d$ . The normal unit vector  $\hat{n}$  on the surface  $S^-$  points into the region  $V_2$  and out of the region  $V_1$ . On the surfaces  $S^+$  and  $S^d$ ,  $\hat{n}$  points into region  $V_0$  and out of regions  $V_2$  and  $V_1$ .

The equivalence principle is applied to create the two auxiliary problems shown in Fig. 2 [7]. The first (Fig. 2a) is the exterior equivalent problem that is electromagnetically equivalent to the original problem in region  $V_0$ . The second (Fig. 2b) is equivalent to the original problem in region  $V_1$ .

In the TM case the equivalent electric currents  $J^d$ ,  $J^+$ , and

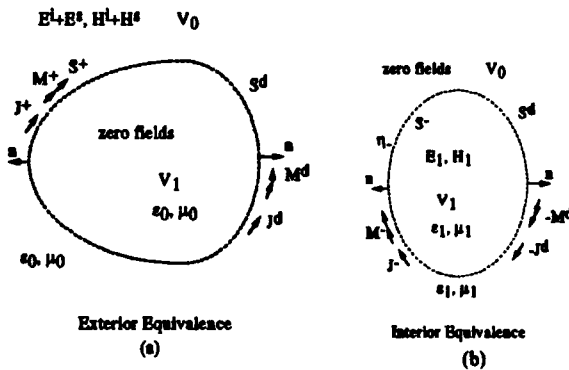


Fig.2 The equivalence problems

$J$  are all axially directed and the equivalent magnetic currents  $M^d$ ,  $M^+$ , and  $M^-$  are circumferentially directed. Using this fact the equivalent currents can be written in the following form:

$$J^q = J_z^q \hat{z} \quad \text{on } S^q \quad (1)$$

$$M^q = M_t^q \hat{t} \quad \text{on } S^q \quad (2)$$

where  $q$  represents  $+$ ,  $-$ , or  $d$ ,  $\hat{z}$  is the unit vector in the  $z$  direction and  $\hat{t}$  is the unit tangent. The unit tangent is defined by the equation

$$\hat{t} = \hat{z} \times \hat{n}. \quad (3)$$

In the zero field regions, the constitutive parameters are taken to be the same as in the non zero field region, so that the equivalent currents in Figs. 2a and 2b radiate into an unbounded homogeneous medium.

To formulate integral equations, the impedance boundary condition is applied on the surfaces  $S^-$  and  $S^+$  and the continuity of the tangential components of the electric and magnetic fields on  $S^d$  is enforced. These boundary conditions are expressed as

$$E_1|_{\text{tan}} = \eta_- \eta_0 (\hat{n} \times H_1) \quad \text{on } S^- \quad (4)$$

$$E_0|_{\text{tan}} = \eta_+ \eta_0 (\hat{n} \times H_0) \quad \text{on } S^+ \quad (5)$$

$$E_1|_{\text{tan}} = E_0|_{\text{tan}} \quad \text{on } S^d \quad (6)$$

and

$$\hat{n} \times H_1 = \hat{n} \times H_0 \quad \text{on } S^d \quad (7)$$

The quantities  $\eta_0$ ,  $\eta_-$  and  $\eta_+$  are the intrinsic impedance of the free space, the normalized surface impedance on  $S^-$  and the normalized surface impedance on  $S^+$  respectively ( $\eta_-$  and  $\eta_+$  are normalized by  $\eta_0$ ). Equations (4) and (5) imply that the tangential components of the electrical field can be expressed in terms of the tangential components of the magnetic field. In terms of the corresponding equivalent magnetic and electric surface currents,

$$M^+ = \eta_0 \eta_+ J_z^+ \times \hat{n} = \eta_0 \eta_+ J_z^+ \hat{t} \quad (8)$$

and

$$M^- = \eta_0 \eta_- J_z^- \times \hat{n} = \eta_0 \eta_- J_z^- \hat{t} \quad (9)$$

To account for different formulations, the integral equations obtained from (4) and (5) may be rewritten as follows [7]:

$$\frac{\alpha}{\eta_0} E_{\parallel} |_{\text{int}} = \beta \eta_- (\hat{n} \times H_1) \quad \text{on } S^- \quad (10)$$

$$\frac{\alpha}{\eta_0} E_{\parallel} |_{\text{ext}} = \beta \eta_+ (\hat{n} \times H_0) \quad \text{on } S^+ \quad (11)$$

where  $\alpha$  and  $\beta$  are, respectively, the combination parameters weighing the EFIE and MFIE just inside the surfaces  $S^+$  and  $S^-$ . Thus different field formulations can be obtained by using (10) and (11), with different selections of  $\alpha$  and  $\beta$ , together with (6) and (7). Equations (6) and (7) represent the PMCHW boundary condition on  $S^d$ . These formulations can be obtained according to Table I.

Table I

Generation of different formulations

Formulation type	$\alpha$	$\beta$
1. IBCE-PMCHW	1.	0.
2. IBCH-PMCHW	0.	-1./ $\eta_c$
3. IBCC-PMCHW	< 1.	-1./ $\eta_c$
4. IBC-PMCHW	1.	1.

In Table I,  $\eta_c$  stands for either  $\eta_+$  or  $\eta_-$ . In the first two formulations, IBCE and IBCH imply that E- and H-field boundary conditions are applied, respectively, just inside the impedance surface with the implementation of the IBC approximation for the magnetic current, whereas PMCHW implies that the continuity of the tangential field components is enforced on the dielectric surface  $S^d$ . In the third formulation IBCC denotes the combination of IBCE and IBCH on the impedance surface. In the fourth formulation, IBC implies that the IBC is applied on the impedance surface. Indeed, still other formulations may be obtained when the Muller formulation is applied on  $S^d$  instead of the

PMCHW formulation [8].

The currents of (1), (2), (8) and (9) give rise to TM fields only. Using this fact equations (10), (11), (6), and (7) can be reduced to scalar integral equations and written as

$$\begin{aligned} & \frac{\alpha}{\eta_0} [E_{1z}(J_z^+) + \eta_- \eta_0 E_{1z}(J_z^+ \hat{t}) + E_{1z}(J_z^+) + E_{1z}(M_1^+)] \\ & - \beta \eta_- [H_{1r}(J_z^+) + \eta_- \eta_0 H_{1r}(J_z^+ \hat{t}) + H_{1r}(J_z^+) + H_{1r}(M_1^+)] \\ & = 0 \quad \text{on } S^- \end{aligned} \quad (12)$$

$$\begin{aligned} & - \frac{\alpha}{\eta_0} [E_{0z}(J_z^-) + \eta_+ \eta_0 E_{0z}(J_z^- \hat{t}) + E_{0z}(J_z^-) + E_{0z}(M_1^-)] \\ & + \beta \eta_+ [H_{0r}(J_z^-) + \eta_+ \eta_0 H_{0r}(J_z^- \hat{t}) + H_{0r}(J_z^-) + H_{0r}(M_1^-)] \\ & = \frac{\alpha}{\eta_0} E_z^i - \beta \eta_+ H_r^i \quad \text{on } S^+ \end{aligned} \quad (13)$$

$$\begin{aligned} & \frac{1}{\eta_0} [E_{0z}(J_z^-) + \eta_+ \eta_0 E_{0z}(J_z^- \hat{t}) + E_{1z}(J_z^-) + \eta_- \eta_0 E_{1z}(J_z^- \hat{t}) \\ & + E_{0z}(J_z^-) + E_{1z}(J_z^-) + E_{0z}(M_1^-) + E_{1z}(M_1^-)] \\ & = \frac{1}{\eta_0} E_z^i \quad \text{on } S^d \end{aligned} \quad (14)$$

$$\begin{aligned} & H_{0r}(J_z^-) + \eta_+ \eta_0 H_{0r}(J_z^- \hat{t}) + H_{1r}(J_z^-) + \eta_- \eta_0 H_{1r}(J_z^- \hat{t}) \\ & + H_{0r}(J_z^-) + H_{1r}(J_z^-) + H_{0r}(M_1^-) + H_{1r}(M_1^-) \\ & = H_r^i \quad \text{on } S^d \end{aligned} \quad (15)$$

where

$$H_r = H \cdot \hat{r} \quad (16)$$

and

$$E_z = E \cdot \hat{z} \quad (17)$$

The operators  $E_{\alpha}(J)$ ,  $E_{\alpha}(M)$ ,  $H_{\alpha}(J)$ , and  $H_{\alpha}(M)$  are determined using the following equations:

$$E_{\alpha}(J_z^{\pm}) = -jk_0 \eta_{\pm} \int_{S^d} J_z^{\pm}(\rho') g_{\alpha}(\rho, \rho') dl \quad (18)$$

$$E_{\alpha}(M_i^{\alpha}) = -\hat{z} \cdot \nabla \times \int_{S'} M_i^{\alpha}(\rho') g_{\alpha}(\rho, \rho') dl' \quad (19)$$

$$H_{\alpha}(J_i^{\alpha}) = \hat{i} \cdot \nabla \times \int_{S'} J_i^{\alpha}(\rho') g_{\alpha}(\rho, \rho') dl' \quad (20)$$

$$H_{\alpha}(M_i^{\alpha}) = \frac{1}{jk_{\alpha}\eta_{\alpha}} \hat{i} \cdot \nabla \times \nabla \times \int_{S'} M_i^{\alpha}(\rho') g_{\alpha}(\rho, \rho') dl' \quad (21)$$

where

$$g_{\alpha}(\rho, \rho') = \frac{1}{4j} H_0^{(2)}(k_{\alpha} |\rho - \rho'|) \quad (22)$$

$k_{\alpha} = \omega\sqrt{\mu_{\alpha}\epsilon_{\alpha}}$ , and  $\eta_{\alpha} = \sqrt{\mu_{\alpha}/\epsilon_{\alpha}}$ . In the expressions above  $\mu_{\alpha}$  and  $\epsilon_{\alpha}$  are the permeability and permittivity of region  $V_{\alpha}$ , and  $H_0^{(2)}$  is the Hankel function of second type and zero order. In Equations 18 through 21 the contour integral is evaluated on the contour that results from the intersection of  $S^+$ ,  $S^-$  or  $S^d$  with the  $x$ - $y$  plane. These contours are referred to as  $S^+$ ,  $S^-$  or  $S^d$  in the context of a two-dimensional body. The contour integrals proceed in the  $\hat{i}$  direction. The vector  $\rho$  is a vector in the  $x$ - $y$  plane that identifies the field point. The vector  $\rho'$  identifies the source point.

Equations (12) to (15) are specific to the TM incident wave case. In the TE case the equivalent electric currents  $J^+$ ,  $J^-$ , and  $J^d$  are all circumferentially directed and the equivalent magnetic currents  $M^+$ ,  $M^-$ , and  $M^d$  are axially directed. The TE polarized case is completely dual to the TM case.

The scattered field can be calculated in the exterior equivalent situation from the currents  $J^+$ ,  $J^-$ , and  $M^d$ . In equation form this is expressed as

$$E_z^s(\rho, \phi) = \eta_{\alpha} \eta_0 E_z(J_i^+ \hat{t}) + E_z(J_i^-) + E_z(J_i^d) + E_z(M_i^d) \quad (23)$$

### 3 NUMERICAL SOLUTION

To solve the surface integral equations, the contours of the scattering body are divided into a number of linear zones. The end points of the zones lie on the actual contours of the body. The length of the zones is taken to be less than one tenth of a wavelength. The currents are expanded in pulses basis functions multiplied by to-be-determined coefficients. The point matching technique is employed to reduce the integral equations to a system of linear equations following

the procedure given in [9]. Using point matching and pulses basis functions allows for accurate representation of the currents at surface of the discontinuities. Accurate representation of the currents is particularly important at the junction [10] between the dielectric surface and conducting or impedance surface. Equations (18) to (22) are reduced to a standard matrix element form and are placed in the proper location in equations (12) to (15) to obtain the moment method matrix. The solution of the matrix determines the current coefficients on all of the surfaces of the scattering body. These coefficients are then used to obtain the far scattered fields. The expressions used to calculate the matrix elements and the scattered fields are given in [9].

### 4 RESULTS AND DISCUSSION

The numerical solutions of the four formulations defined in Table I are verified in this section. First, circular cylindrical bodies are considered. The series solution of an impedance cylinder coated with a linear and homogeneous dielectric layer of uniform thickness is used to verify the numerical results. Fig. 3 shows the normalized bistatic scattering width ( $\sigma/\lambda$ ) from an impedance cylinder of  $\eta=0.5$  and  $ka=3$  coated with a dielectric layer of  $\epsilon_r=4.0$  and  $\mu_r=1.0$ , from  $ka=3$  to  $kb=4$ . The agreement between the numerical solution of all the formulations and the series solution is satisfactory for both TM and TE polarizations. The IBCE-PMCHW and IBCH-PMCHW formulations will

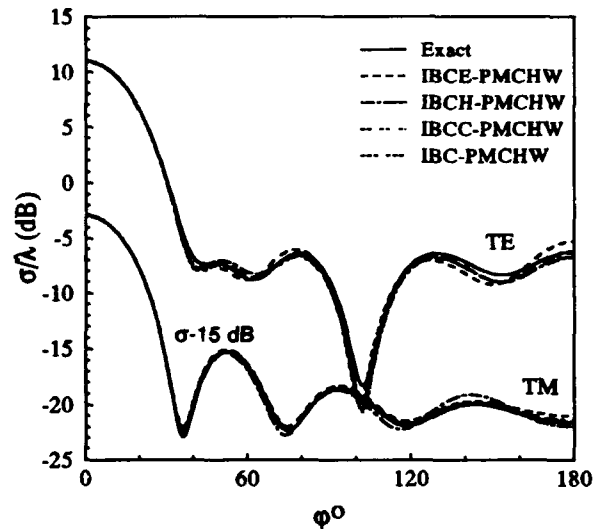


Fig. 3 Bistatic scattering width of a coated impedance circular cylinder,  $ka=3$ ,  $kb=4$ ,  $\epsilon_r=4$ ,  $\mu_r=1$ , and  $\eta=0.5$ .

fail when the impedance core is at resonance. To illustrate this failure, one specific example is presented. The case of

a circular impedance cylinder coated with a uniform dielectric layer, with  $ka=2.71$ ,  $kb=3$ ,  $\epsilon_r=2$ ,  $\mu_r=1$ , and  $\eta$ .

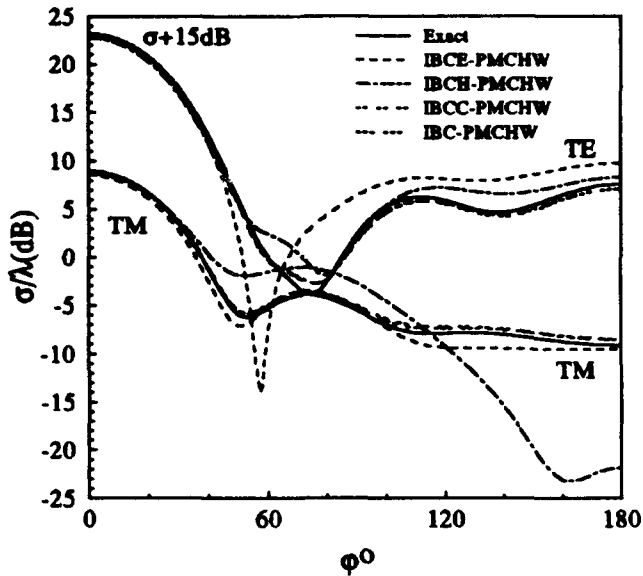


Fig. 4 Bistatic scattering width of a coated circular cylinder,  $ka=2.71$ ,  $kb=3$ ,  $\epsilon_r=2$ ,  $\mu_r=1$ , and  $\eta=0.5$ .

$=0.5$ , is considered. This example was selected because it has the same resonance frequency for both polarizations. Fig. 4 shows the comparison between the bistatic patterns computed numerically using the present method and the bistatic pattern determined using the series solution. Clearly the solution due to the IBCE-PMCHW and IBCH-PMCHW formulations fails to give the correct solution. The results from the other two formulations, the IBCC-PMCHW and IBC-PMCHW, are in good agreement with the exact solution, indicating that they are not affected by the internal resonance problem. If in the previous example the surface impedance is zero, the perfect conducting core case, the IBC-PMCHW formulation will fail to give the correct solution because it reduces to the E-PMCHW formulation.

In the previous examples we have considered completely coated objects. In the following examples we will consider partially coated objects. The bistatic scattering width of a half-dielectric/half-impedance cylinder of  $ka=3$ ,  $\eta_r=\eta_i=0.5$ ,  $\epsilon_r=1$ , and  $\mu_r=1$  ("phantom" dielectric) is computed for all formulations. Results for the object with the "phantom" dielectric half must be the same as those for an impedance half-cylinder. In Fig. 5 a comparison is made between the numerical solution of the impedance body with the "phantom" dielectric half and the numerical solution of the impedance half-cylinder with  $\eta_r=0.5$ . Excellent agreement is observed. The same geometry is considered with  $\epsilon_r=4$  and the numerical results are compared with the

numerical solution of the same object where the impedance half is replaced by a lossy dielectric half cylinder ( $\epsilon_{r1}=8-j16$

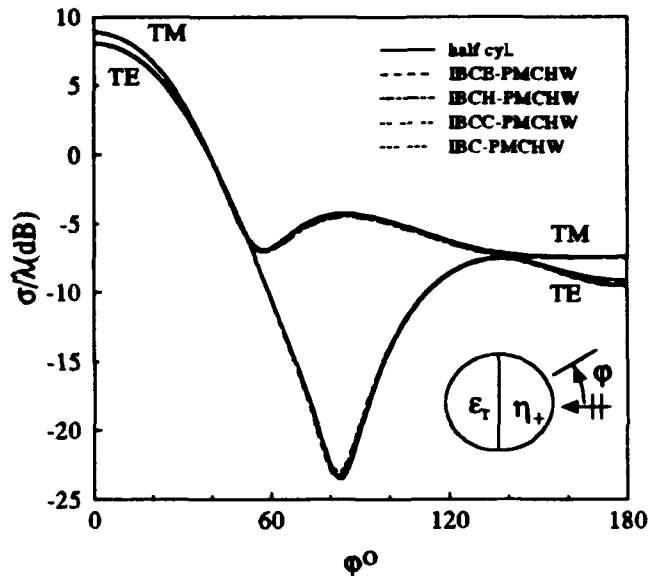


Fig. 5 Comparison between the bistatic scattering width of a half impedance cylinder and half impedance/half dielectric cylinder,  $ka=3$ ,  $\eta_r=\eta_i=0.5$ ,  $\epsilon_r=1$ , and  $\mu_r=1$ .

and  $\mu_{r1}=2-j4$ ), which has an equivalent normalized surface impedance of 0.5. For the lossy materials the exact boundary conditions are enforced on all the object boundaries. Fig. 6 and 7 show a comparison between the electric and magnetic surface currents, respectively, on the outer surfaces of the object using the numerical solution

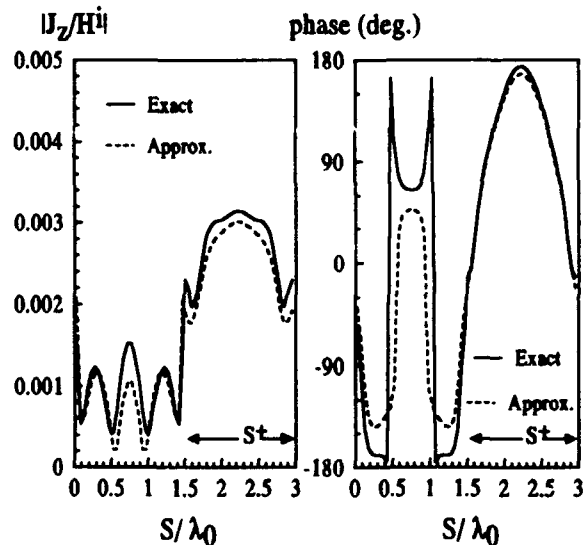


Fig. 6 (TM) Electric outer surface current on a half lossy /half dielectric cylinder and half impedance/half dielectric cylinder,  $ka=3$ ,  $\epsilon_r=4$ , and  $\mu_r=1$

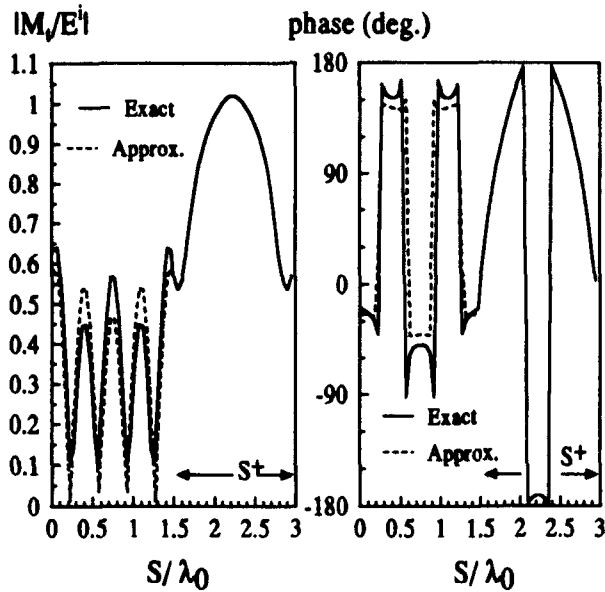


Fig. 7 (TM) Magnetic surface currents on a half lossy /half dielectric cylinder and half impedance/half dielectric cylinder,  $ka=3$ ,  $\epsilon_r=4$ , and  $\mu_r=1$

with exact boundary conditions and the approximate solution of the E-PMCHW formulation for the TM polarization. Good agreement between both results is obtained in the currents magnitudes, but a large difference is observed in the phase of the electric current on the pure dielectric surface. If more accurate estimate of the surface impedance were used, better accuracy could be achieved. A significant observation is the excellent accuracy of the surface currents around the junction. The junction between three or more dielectric regions can be treated accurately even when triangle basis functions are used [10]. However, the treatments of junctions between dielectric and conductor or impedance surfaces with triangle basis functions requires an approximations which neglects the contributions due to the magnetic currents on half the triangle basis functions around the junctions. This problem does not exist when point matching and pulses basis functions are used. Fig. 8 illustrated that the exact solution and the approximate solutions for the scattering width are in excellent agreement with each other. It seems that the current error has insignificant effect on the far scattered field calculations. If the lossy material is changed so that  $\epsilon_{r1} = 6-j4$  and  $\mu_{r1} = 1$ , the equivalent surface impedance is  $\eta_r = \eta_+ = 0.3564 + j0.108$ . For this example, results for the solution incorporating the exact boundary conditions and the approximate solutions (the present method) are compared in Fig. 9. The agreement in this case is not as good as in the previous example. This result is expected because the surface impedance is calculated assuming that there is no wave transmitted through the dielectric. These results indicate that the fields

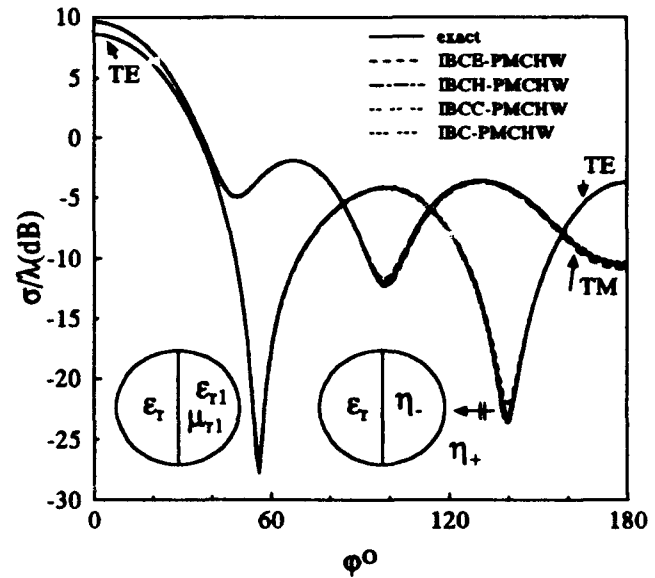


Fig. 8 Bistatic scattering width of the case in Fig. 6 and 7

within the lossy material in the latter example are much larger than in the former example.

Only bistatic radar cross section has been considered to this point. The effect of different angles of incident can be investigated by computing the monostatic scattering width.

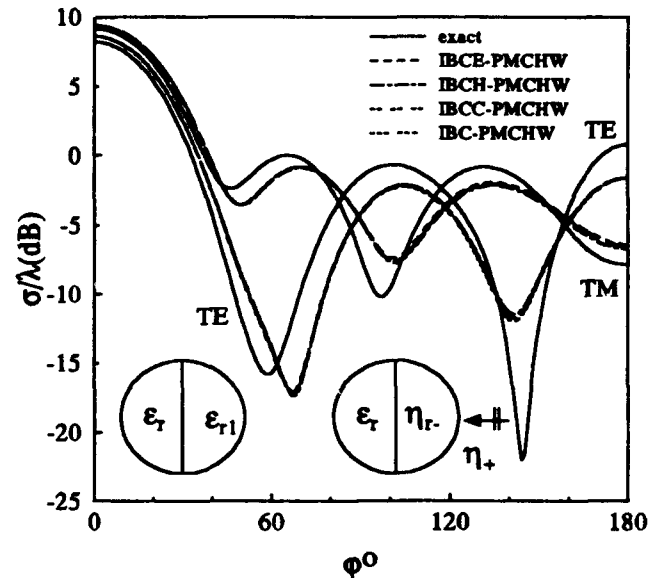


Fig. 9 Bistatic scattering width of a half lossy/half dielectric cylinder and half impedance/half dielectric cylinder,  $ka=3$ ,  $\epsilon_r=4$ , and  $\mu_r=1$ .

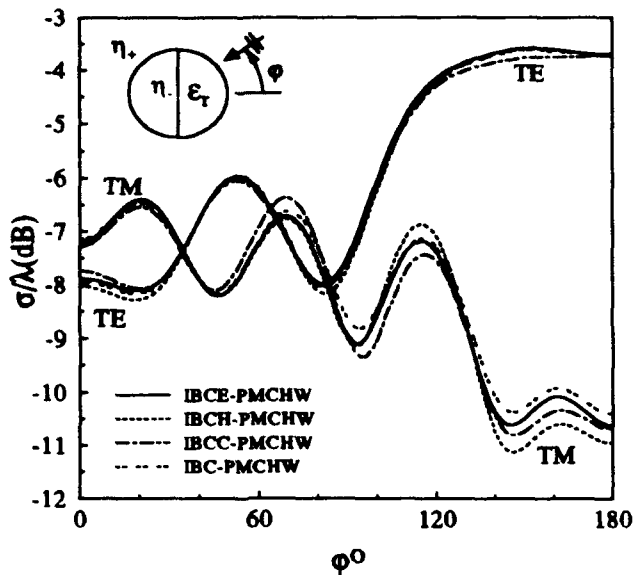


Fig. 10 Monostatic scattering width of half impedance/half dielectric cylinder,  $ka=3$ ,  $\eta_c=\eta_s=0.5$ ,  $\epsilon_r=4$ , and  $\mu_r=1$ .

The monostatic scattering width of the object considered in Fig. 8 is given in Fig. 10. The agreement between the numerical solution of the different formulations is within 0.75 dB for the TM polarization and 0.25 dB for the TE polarization.

It is known that if the surface impedance of an object equal to the intrinsic impedance of free space, the object will have zero back scattering width. This suggest that a reduction of the scattering width for an object can be obtained by manipulating the material parameters of the object. To illustrate this technique, the dielectric-coated rounded impedance cylinder shown in insert of Fig. 11a is considered. For the original scattering object, consider the core to be perfect electric conductor ( $\eta_c=0.0$ ) coated with a uniform dielectric layer of thickness  $t=0.1\lambda_0$  and  $\epsilon_r=4.0-j1.7$ . If the transmission line model is used to calculate the equivalent surface impedance on the outer dielectric surface, the surface impedance is  $\eta_+=(0.6828+j1.0247)$  (neglecting the curvature of the surface). To reduce the scattering width, the core is selected to be an impedance surface and its surface impedance value is manipulated to make the equivalent outer surface impedance resistive and equal to the characteristic impedance of free space. It is found, using the transmission line model, that with  $\eta_c=(0.092+j0.215)$  an outer surface impedance of  $\eta_+=(1.0026+j0.0058)$  results. The scattering width which is calculated for the original

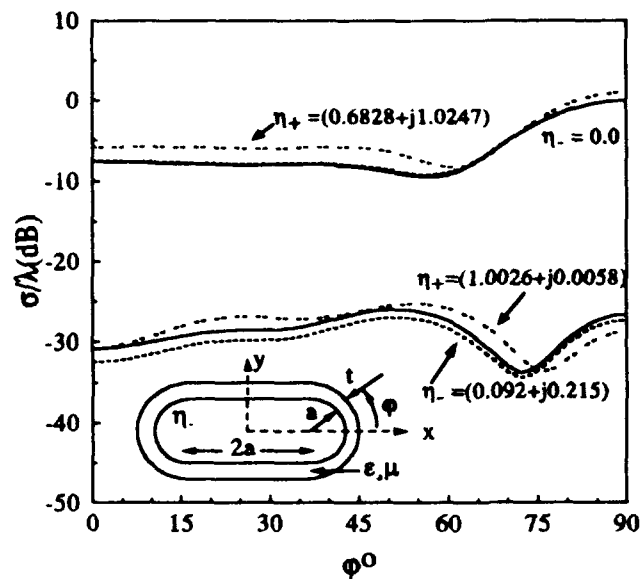


Fig. 11a Monostatic scattering width of a coated rounded impedance cylinder when  $\eta_c=0.0$  and  $\eta_c=0.092+j0.215$ ,  $\epsilon_r=4-j1.7$ , and  $\mu_r=1$  (TM).

object and for the reduced scattering width body is shown in

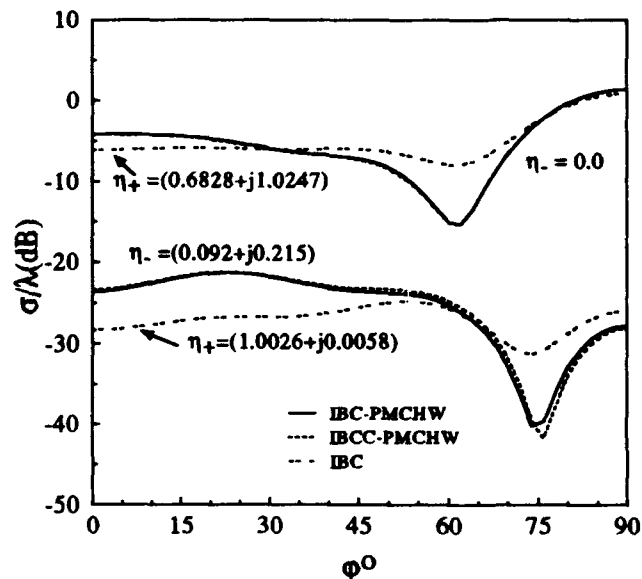


Fig. 11b Monostatic scattering width of a coated rounded impedance cylinder when  $\eta_c=0.0$  and  $\eta_c=0.092+j0.215$ ,  $\epsilon_r=4-j1.7$ , and  $\mu_r=1$  (TE).

Fig. 11. In Fig 11, two models are used for each of the bodies to calculate the scattering width. The first model is the two surface model. The two surface model considers

both the inner impedance surface and the outer dielectric surface. The second model is a one surface model. The one surface model treats the outer dielectric surface as an impedance surface with equivalent surface impedance  $\eta_s$ . Results of the one surface model are denoted as IBC results in Fig. 11. For the body consisting of a dielectric coated core, significant reduction of the scattering width is achieved using an impedance core instead of a perfect electric conductor (PEC) core. The scattering width solution obtained using the one surface model is less accurate than that obtained using the two surface model. For the one surface model, the solution error is more pronounced in the TE case than in the TM case. This example illustrates that proper selection of the core material results in low back scattering width and that the present method can be used to accurately predict the reduced scattering width.

## 5 CONCLUSION

Four surface integral equation formulations are developed for two-dimensional objects composed of impedance surfaces partially coated with dielectric material. These formulations are useful in obtaining accurate and economical numerical solutions for bodies that can be modeled as coated impedance surfaces. Both TE and TM polarizations are considered. The point matching technique is used to solve the surface integral equations. The numerical solutions are verified either by comparison with the series solution for circular cylinders or by comparison with exact solutions (exact boundary conditions on all surface boundaries) for other objects. The internal resonance problem is investigated and a form of the combined field integral equation is proposed to overcome this problem. The solution accuracy is shown to be independent of the polarization. It is also shown that accurate evaluation of the surface impedance is very important to achieve good accuracy. One example is given to show that low back-scattering width can be achieved by selecting the material properties so that the outer surface impedance is equal to the characteristic impedance of free space.

## 6 ACKNOWLEDGMENTS

This work was partially supported by the National Science Foundation under Grant Number ECS-8906807.

## 7 REFERENCES

- [1] T. B. A. Senior, "Approximate boundary conditions," *IEEE Trans. Antennas Propagat.*, vol. 29, pp. 826-829, 1981.
- [2] J. R. Wait, "Use and misuse of impedance boundary conditions in electromagnetics", *Proc. PIERS Symposium*, Boston, MA, p. 358, July 1989.
- [3] D.-S. Wang, "Limits and validity of the impedance boundary condition for penetrable surfaces", *IEEE Trans. Antennas Propagat.*, Vol. AP-35, pp. 453-457, No. 4, 1987.
- [4] S.-W. Lee, "How good is the impedance boundary condition?", *IEEE Trans. Antennas Propagat.*, Vol. AP-35, pp. 1313-1315, No. 11, 1987.
- [5] J. L. Volakis and T. B. A. Senior, "Application of a class of generalized boundary conditions to scattering by a metal-backed dielectric half-plane," *Proc. IEEE*, Vol. 77, pp. 796-805, May 1989.
- [6] T. B. A. Senior and J. L. Volakis, "Derivation and application of a class of generalized boundary conditions," *IEEE Trans. Antennas Propagat.*, Vol. AP-37, pp. 1566-1572, No. 12, 1989.
- [7] A. A. Kishk, "Electromagnetic scattering from composite objects using a mixture of exact and impedance boundary conditions," *IEEE Trans. Antennas Propagat.*, Vol. AP-39, pp. 826-833, No. 6, 1991.
- [8] A. A. Kishk and L. Shafai, "On the accuracy limits of different integral-equation formulations for numerical solution of dielectric bodies of revolution," *Canadian Journal of Physics*, vol. 63, no. 12, pp. 1532-1539, 1985.
- [9] P. M. Goggans, "A combined method-of-moments and approximate boundary condition solution for scattering from a conducting body with a dielectric-filled cavity," *Ph.D. Dissertation*, Auburn University, 1990.
- [10] J. M. Putnam and L. N. Medgyesi-Mitschang, "Combined field integral equation formulation for inhomogeneous two- and three-dimensional bodies: The junction problem," *IEEE Trans. Antennas Propagat.*, Vol. AP-39, pp. 667-672, No. 5, 1991.

# Efficient Matrix Element Calculations for the Spectral Domain Method Applied to Symmetrical Multiconductor Transmission Lines

J.C. Coetzee and J.A.G. Malherbe

Department of Electrical and Electronic Engineering  
University of Pretoria  
Pretoria 0002, South Africa

## Abstract

The spectral domain method has proved to be a suitable analytical tool for the characterization of open, symmetrical planar structures. The method requires the repeated calculation of matrix elements, which each involves the time-consuming process of numerical integration over an infinite range. In this paper, suitable basis functions for the expansion of electric surface currents on strips or electric fields in slots, are provided. It is also shown how the use of these basis functions makes possible the efficient and rapid calculation of the matrix elements.

## 1. Introduction

The spectral domain method has become an important tool in the analysis of microwave and millimetre wave integrated circuits [1]. Of particular interest in this paper is its application on the characterization of open, symmetrical planar structures where substrates are assumed to be infinitely wide [2-6]. The method generally requires a significant amount of analytical preprocessing, but the introduction of the imittance approach [2] has simplified the derivation of the dyadic Green's function elements. However, some practical difficulties are still encountered during the implementation of the method, and in this paper we show how these may be overcome.

Application of the imittance approach yields the spectral dyadic Green's function for the planar structure under consideration. The unknown electric surface currents on strips (or electric fields in slots) are expanded into finite sets of basis functions. For a solution of the dispersion characteristics, the method requires an iterative search for the value of the axial propagation constant,  $\beta$ , which renders the determinant of a square matrix to zero. The matrix elements need to be recalculated during each iteration. The computation of each individual matrix element requires numerical integration over an infinite range, where the integrand contains basis functions that have been used in the expansions. These calculations are the most time-consuming steps in the implementation of the method. Due to the slow rate of convergence of certain integrals, difficulties are encountered in attempts to attain the required accuracy tolerances during the numerical integration. In this paper, we provide suitable basis functions for the expansion of unknown electric currents or fields. The use of these basis functions facilitates the efficient calculation of the matrix elements.

## 2. Suitable basis functions

Consider the general multilayered planar structure shown in Figure 1. It consists of a number of dielectric layers, with strips and/or slots spaced symmetrically about the  $y$ -axis between the different layers. The structure has infinitely thin metallized surfaces with infinitely wide dielectric substrates, and is homogeneous in the  $z$ -direction. It may be analyzed in the spectral domain, with the Fourier transform defined as

$$\begin{aligned}\tilde{\Phi}(\alpha) &= \int_{-\infty}^{\infty} \Phi(x) e^{j\alpha x} dx \\ \Phi(x) &= \frac{1}{2\pi} \int_{-\infty}^{\infty} \tilde{\Phi}(\alpha) e^{-j\alpha x} d\alpha\end{aligned}\tag{1}$$

The electric surface currents on all finite width strips and the transverse (with respect to the  $y$  direction) electric fields in finite width slots are expanded into finite sets of basis functions. Using the immittance approach [2], equivalent circuits may be constructed, where the expanded quantities act as current and voltage sources respectively. From the equivalent circuits, the elements of the spectral dyadic Green's function are obtained in closed form.

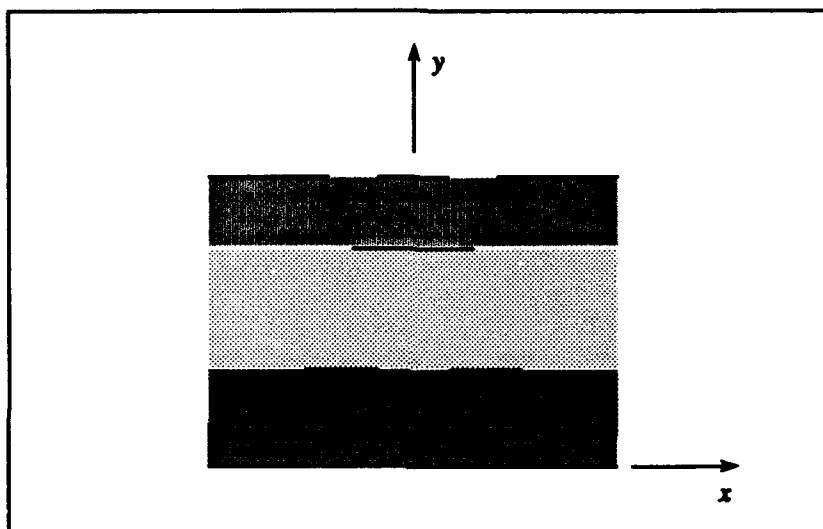


Figure 1 Symmetrical multilayered planar structure.

In symmetrical planar structures, the strips or slots in a specific plane  $y = y_1$  belong to one of two categories, namely

1. A *single* strip or slot centred at  $x = 0$ , as shown in Figure 2(a).
2. A *pair* of strips or slots centred at  $x = b$  and  $x = -b$  respectively, as depicted in Figure 2(b).

A multiconductor transmission line supports a number of fundamental modes. For symmetrical structures, each mode belongs to one of two mode types, which we denominate as *even* and *odd* type modes. The field distribution of even (odd) type modes is characterized by the fact that a magnetic conductor (electric conductor) may be introduced in the plane of symmetry without disturbing the fields. Depending on the mode type, only basis functions which are either even or odd functions of  $x$  need to be included in the expansion of currents on single strips or fields in single slots. The same symmetry considerations hold for the case of a pair of strips or slots. It is however necessary to include basis functions which are both even and odd with respect to the individual axes of a pair of strips or slots [6]. This could be explained by means of the following example. Let Figure 2(b) represent a pair of strips, and we would like to expand the electric surface current  $J_x(x, y_1)$  for an even type mode. From the symmetry considerations it then follows that  $J_x(x, y_1)$  should be an odd function of  $x$ , and that its basis functions should thus all be odd with respect to  $x = 0$ . However, the current distribution on the right hand strip would in general not be symmetrical about its axis at  $x = b$ . This fact therefore requires the inclusion of basis functions which are even and basis functions which are odd with respect to  $x = b$  in the domain  $|x - b| \leq w/2$ .

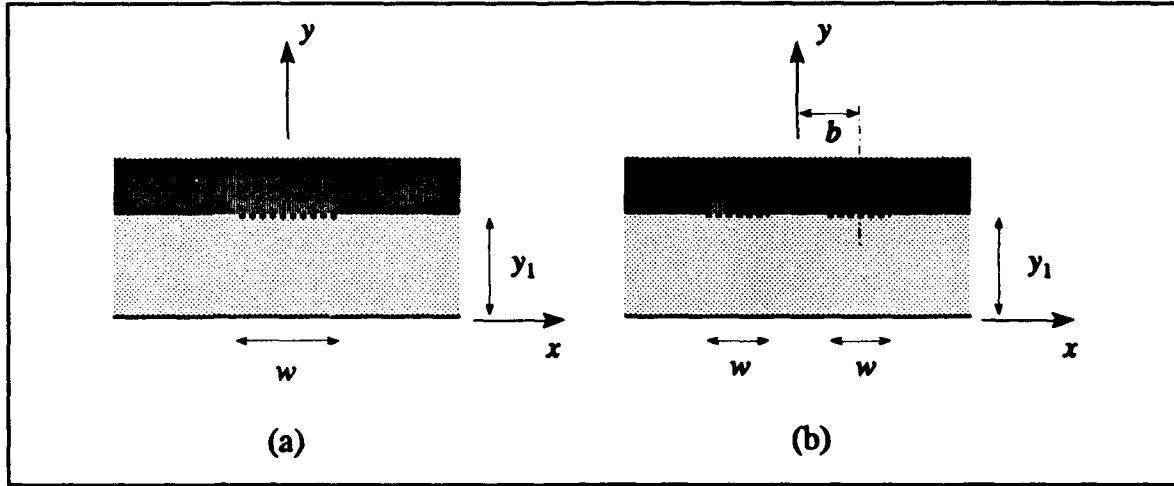


Figure 2 (a) A single strip or slot and (b) a pair of strips or slots.

The surface currents or electric fields in the plane  $y = y_1$  may be expanded using any kind of basis functions, as long as they are non-zero only for  $|x| \leq w/2$  in the case of Figure 2(a), or only for  $|x \pm b| \leq w/2$  in Figure 2(b). The efficiency and accuracy of the method is, however, dependent on the choice of basis functions. The singular behaviour of the electric surface currents parallel to the strip edges or the electric fields normal to the slot edges should therefore be incorporated in the basis functions [7].

In general, the surface currents or electric fields in the plane  $y = y_1$  may be expanded as

$$F(x, y_1) = \sum_{n=1}^N a_n f_n(x) \quad G(x, y_1) = \sum_{n=1}^M b_n g_n(x) \quad (2)$$

where  $F(x, y_1)$  and  $G(x, y_1)$  represent  $J_x(x, y_1)$  and  $J_z(x, y_1)$ , or  $E_z(x, y_1)$  and  $E_x(x, y_1)$ . The terms  $a_n$  and  $b_n$  are unknown coefficients, while  $f_n(x)$  and  $g_n(x)$  are basis functions which satisfy the edge conditions. In the spectral domain, this becomes

$$F(\alpha, y_1) = \sum_{n=1}^N a_n \hat{f}_n(\alpha) \quad G(\alpha, y_1) = \sum_{n=1}^M b_n \hat{g}_n(\alpha) \quad (3)$$

We define two sets of functions which may act as building blocks for the appropriate bases. These are given by

$$\left. \begin{aligned} \xi_m(x, w) &= \frac{T_{m-1}(2x/w)}{\sqrt{1 - (2x/w)^2}} \\ \zeta_m(x, w) &= \sqrt{1 - (2x/w)^2} U_{m-1}(2x/w) \end{aligned} \right\} \begin{aligned} |x| &\leq w/2 \\ m &= 1, 2, 3, \dots \end{aligned} \quad (4)$$

$T_m(x)$  and  $U_m(x)$  are  $m$ th order Chebyshev polynomials of the first and second kind respectively. These functions are shown in Figure 3 for different values of  $m$ .  $\xi_m(x, w)$  is singular at  $|x| = w/2$ . Also note

that  $\xi_m(x, w)$  and  $\zeta_m(x, w)$  are even functions of  $x$  for  $m$  odd, and *vice versa*.

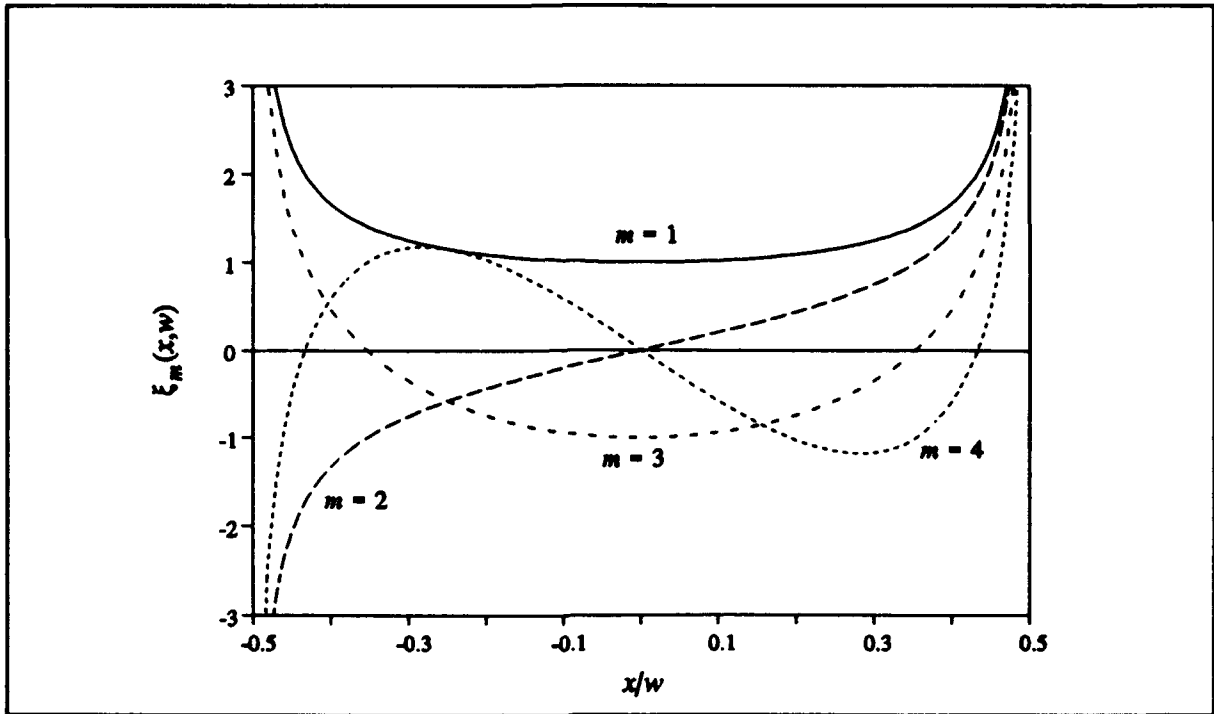


Figure 3(a) The function  $\xi_m(x, w)$  for different values of  $m$ .

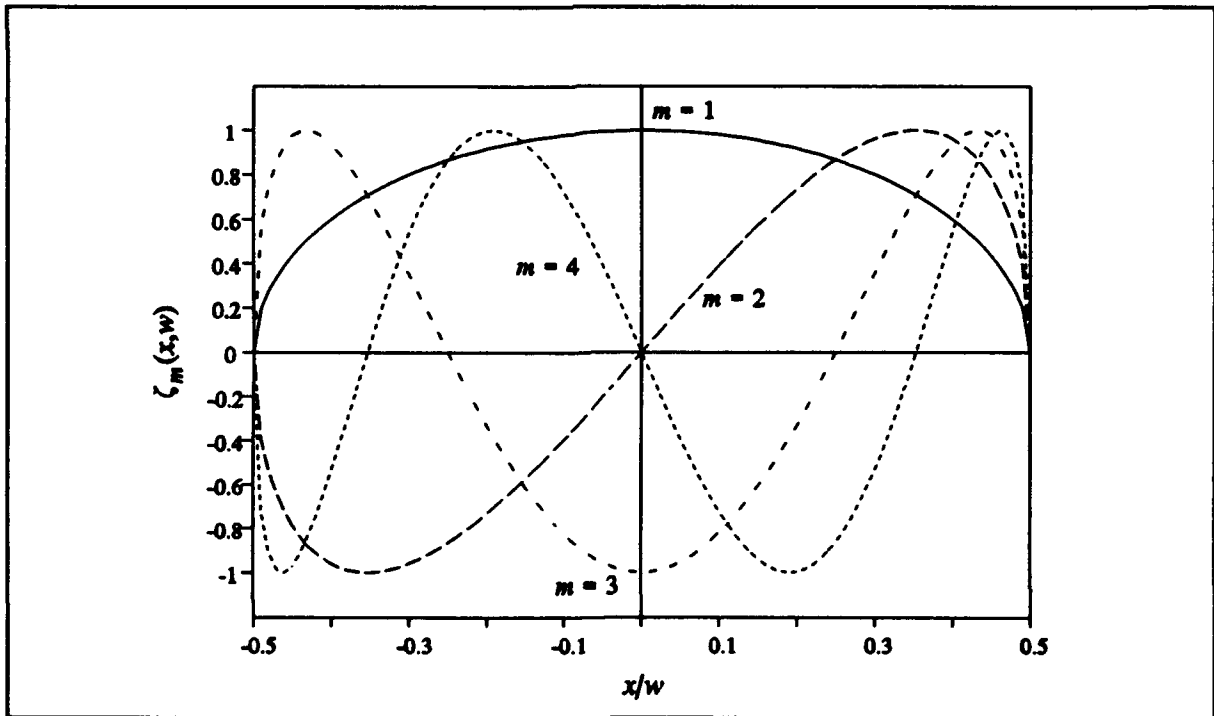


Figure 3(b) The function  $\zeta_m(x, w)$  for different values of  $m$ .

Their Fourier transforms are given by

$$\bar{\xi}_m(\alpha, w) = j^{m-1} \frac{\pi w}{2} J_{m-1}(\alpha w/2) \quad \bar{\zeta}_m(\alpha, w) = j^{m-1} \frac{\pi m}{\alpha} J_m(\alpha w/2) \quad (5)$$

where  $J_m(x)$  is the Bessel function of the first kind of order  $m$ . The basis functions  $f_n(x)$  and  $g_n(x)$  may thus be expressed as combinations and permutations of  $\zeta_n(x, w)$  and  $\xi_n(x, w)$  respectively. Table 1 provides suitable basis functions for the expansion of the different unknown quantities.

Single / Pair	Strip / Slot	Expanded quantity	Mode type	Basis function	Fourier transform of basis function		
Single	Strip	$J_x(x, y_1)$	Even	$\zeta_{2n}(x, w)$	$\bar{\zeta}_{2n}(\alpha, w)$		
			Odd	$\zeta_{2n-1}(x, w)$	$\bar{\zeta}_{2n-1}(\alpha, w)$		
		$J_z(x, y_1)$	Even	$\xi_{2n-1}(x, w)$	$\bar{\xi}_{2n-1}(\alpha, w)$		
			Odd	$\xi_{2n}(x, w)$	$\bar{\xi}_{2n}(\alpha, w)$		
	Slot	$E_x(x, y_1)$	Even	$\xi_{2n}(x, w)$	$\bar{\xi}_{2n}(\alpha, w)$		
			Odd	$\xi_{2n-1}(x, w)$	$\bar{\xi}_{2n-1}(\alpha, w)$		
		$E_z(x, y_1)$	Even	$\zeta_{2n-1}(x, w)$	$\bar{\zeta}_{2n-1}(\alpha, w)$		
			Odd	$\zeta_{2n}(x, w)$	$\bar{\zeta}_{2n}(\alpha, w)$		
Pair	Strip	$J_x(x, y_1)$	Even	$\zeta_n(x+b, w) - \delta \zeta_n(x-b, w)$	$-2j \sin(\alpha b) \bar{\zeta}_n(\alpha, w)$ $2 \cos(\alpha b) \bar{\zeta}_n(\alpha, w)$	$n$ odd $n$ even	
			Odd	$\zeta_n(x+b, w) + \delta \zeta_n(x-b, w)$	$2 \cos(\alpha b) \bar{\zeta}_n(\alpha, w)$ $-2j \sin(\alpha b) \bar{\zeta}_n(\alpha, w)$	$n$ odd $n$ even	
			$J_z(x, y_1)$	Even	$\xi_n(x+b, w) + \delta \xi_n(x-b, w)$	$2 \cos(\alpha b) \bar{\xi}_n(\alpha, w)$ $-2j \sin(\alpha b) \bar{\xi}_n(\alpha, w)$	$n$ odd $n$ even
				Odd	$\xi_n(x+b, w) - \delta \xi_n(x-b, w)$	$-2j \sin(\alpha b) \bar{\xi}_n(\alpha, w)$ $2 \cos(\alpha b) \bar{\xi}_n(\alpha, w)$	$n$ odd $n$ even
		Slot	$E_x(x, y_1)$	Even	$\xi_n(x+b, w) - \delta \xi_n(x-b, w)$	$-2j \sin(\alpha b) \bar{\xi}_n(\alpha, w)$ $2 \cos(\alpha b) \bar{\xi}_n(\alpha, w)$	$n$ odd $n$ even
				Odd	$\xi_n(x+b, w) + \delta \xi_n(x-b, w)$	$2 \cos(\alpha b) \bar{\xi}_n(\alpha, w)$ $-2j \sin(\alpha b) \bar{\xi}_n(\alpha, w)$	$n$ odd $n$ even
			$E_z(x, y_1)$	Even	$\zeta_n(x+b, w) + \delta \zeta_n(x-b, w)$	$2 \cos(\alpha b) \bar{\zeta}_n(\alpha, w)$ $-2j \sin(\alpha b) \bar{\zeta}_n(\alpha, w)$	$n$ odd $n$ even
				Odd	$\zeta_n(x+b, w) - \delta \zeta_n(x-b, w)$	$-2j \sin(\alpha b) \bar{\zeta}_n(\alpha, w)$ $2 \cos(\alpha b) \bar{\zeta}_n(\alpha, w)$	$n$ odd $n$ even

Table 1 The  $n$ th basis function for the expansion of currents or fields, where  $n = 1, 2, 3, \dots$  and  $\delta = \pm 1$  for  $n$  odd and  $n$  even respectively.

### 3. Calculation of the matrix elements

Application of Galerkin's method together with Parseval's theorem then results in the eigenvalue equation which needs to be solved numerically [2-7]. The matrix elements that need to be calculated during the process, are all of the form [7]

$$\begin{aligned} P(\beta) &= \int_{-\infty}^{\infty} \tilde{G}(\alpha, \beta) \tilde{h}_a(\alpha) \tilde{h}_b(\alpha) d\alpha \\ &= 2 \int_0^{\infty} \tilde{G}(\alpha, \beta) \tilde{h}_a(\alpha) \tilde{h}_b(\alpha) d\alpha \end{aligned} \quad (6)$$

where  $\tilde{G}(\alpha, \beta)$  is an element of the spectral dyadic Green's function.  $\tilde{h}_a(\alpha)$  and  $\tilde{h}_b(\alpha)$  are Fourier transformed basis functions pertaining to a domain with relevant dimensions denoted by subscripts  $a$  and  $b$  respectively.

For closed structures, the integrand of equation (6) might have poles located on the axis of integration. This necessitates the application of residue calculus techniques for the evaluation of the integrals [1,8]. These processes are considered to be beyond the scope of this paper.

In the case of open structures, no poles are located on the axis of integration, and therefore no special pole extraction techniques are required for the calculation of the integrals. However, the matrix elements are computed by performing numerical integration over an semi-infinite range, and often the rate of convergence is slow. This presents difficulties in attaining the required accuracy tolerances. By applying the following techniques, these difficulties may be overcome.

Using the basis functions defined in (5) and Table 1, we see that the product  $\tilde{h}_a(\alpha) \tilde{h}_b(\alpha)$  consists of :

1. A complex constant term.
2. A term of the form  $\alpha^{-r}$  with  $r = 0, 1, \text{ or } 2$ . For example, if either  $\tilde{h}_a(\alpha)$  is proportionate to  $\tilde{f}_m(\alpha, w_a)$  or  $\tilde{h}_b(\alpha)$  is proportionate to  $\tilde{f}_m(\alpha, w_b)$ , then  $r = 1$ . If neither  $\tilde{h}_a(\alpha)$  nor  $\tilde{h}_b(\alpha)$  is proportionate to  $\tilde{f}_m$ , then  $r = 0$ .
3. A product of two Bessel functions.
4. Zero, one or two  $\sin(\alpha b)$  and/or  $\cos(\alpha b)$  terms, where  $b = b_a$  or  $b = b_b$ . If both  $\tilde{h}_a(\alpha)$  and  $\tilde{h}_b(\alpha)$  pertain to single strips or slots, no sines or cosines would appear in the product. If either of the basis functions pertains to a pair of strips or slots, then the product of the bases contains one sine or cosine term. Finally, if both  $\tilde{h}_a(\alpha)$  and  $\tilde{h}_b(\alpha)$  belongs to pairs of strips/slots, each would contribute a  $\sin(\alpha b)$  or  $\cos(\alpha b)$  term to the product of the bases.

When the product of two trigonometric terms appear in the integrand of equation (6), the following identities are used to transform it to the sum of two terms.

$$\begin{aligned} \sin(\alpha b_a) \sin(\alpha b_b) &= \frac{1}{2} \{ \cos[\alpha(b_a - b_b)] - \cos[\alpha(b_a + b_b)] \} \\ \cos(\alpha b_a) \cos(\alpha b_b) &= \frac{1}{2} \{ \cos[\alpha(b_a - b_b)] + \cos[\alpha(b_a + b_b)] \} \\ \sin(\alpha b_a) \cos(\alpha b_b) &= \frac{1}{2} \{ \sin[\alpha(b_a - b_b)] + \sin[\alpha(b_a + b_b)] \} \end{aligned} \quad (7)$$

Equation (6) may thus in general be rewritten in the form

$$\begin{aligned}
 P(\beta) &= \sum_{i=0}^{\infty} A_i \int_0^{\infty} \frac{G(\alpha, \beta)}{\alpha} J_1(\alpha w_a/2) J_1(\alpha w_b/2) p_i(\alpha) d\alpha \\
 &= \sum_{i=0}^{\infty} A_i F_i(\beta)
 \end{aligned} \tag{8}$$

$$\begin{array}{lll}
 p_0(\alpha) = 1 & p_1(\alpha) = \sin(\alpha b_a) & p_2(\alpha) = \cos(\alpha b_a) \\
 p_3(\alpha) = \sin(\alpha b_b) & p_4(\alpha) = \cos(\alpha b_b) & p_5(\alpha) = \sin[\alpha(b_a + b_b)] \\
 p_6(\alpha) = \cos[\alpha(b_a + b_b)] & p_7(\alpha) = \sin[\alpha(b_a - b_b)] & p_8(\alpha) = \cos[\alpha(b_a - b_b)]
 \end{array}$$

where  $k$  and  $l$  are integers.  $A_0, A_1, \dots, A_8$  are complex constants, of which at least seven are zero. Therefore, a maximum of two terms in the series need to be computed. Note that equation (8) is not an expansion of the original integral in (6) - it is merely a general representation of all the possible forms equation (6) might take on after the transformations of (7) had been applied. If, for example, the original integrand in (6) contains the term  $\cos(\alpha b_a) \cos(\alpha b_b)$ , the only non-zero  $A_i$ 's in (8) are  $A_6$  and  $A_8$ . For the special case where  $b_a = b_b$ , the non-zero constants are  $A_0$  and  $A_6$ .

For  $i \neq 0$ , the integrands of the  $F_i(\beta)$  terms are all oscillatory over the entire range. These integrals have a poor convergence rate when it is evaluated with conventional quadrature routines. They may be computed much more efficiently by treating them as Fourier integrals with the sine and cosine terms as kernels. A special routine such as QDAWF [9] may then be used to evaluate these integrals. QDAWF is an adaptive routine, designed to integrate functions of the form  $f(x) \sin(\omega x)$  or  $f(x) \cos(\omega x)$  over a semi-infinite range. It integrates the integrand between zeros over a number of subintervals, and invokes an extrapolation scheme in order to estimate the integral.

In general, the  $F_0(\beta)$  term may be calculated by using a routine like QDAGI [9]. QDAGI is an integration routine designed to numerically evaluate integrals over an infinite or semi-infinite range. It initially transforms the interval into the finite interval  $[0, 1]$ , and then uses a 21 point Gauss-Kronrod rule to estimate the integral. The integrand of the  $F_0(\beta)$  term is well behaved, provided that the basis functions  $\tilde{h}_a(\alpha)$  and  $\tilde{h}_b(\alpha)$  are not associated with the same single or pair of strips or slots. Inspection reveals that the bases  $\tilde{h}_a(\alpha)$  and  $\tilde{h}_b(\alpha)$  then necessarily pertain to strips or slots that are on different vertical planes. (If  $\tilde{h}_a(\alpha)$  and  $\tilde{h}_b(\alpha)$  are associated with different strips or slots on the same vertical plane, the constant  $A_0$  is zero, and therefore the  $F_0(\beta)$  term need not be computed.) The Green's function elements are then of such a form that the integrand decays rapidly for large values of  $\alpha$ , and therefore the integral converges quickly.

However, when this provision does not apply, the basis functions  $h_a(x)$  and  $h_b(x)$  are defined over the same domain (so that  $w_a = w_b = w$  and  $b_a = b_b = b$ ). The integrand then decays less rapidly, which causes the rate of convergence to be slow. As reported for the specific case of a single slot in [4],  $F_0(\beta)$  may then be converted into a rapidly convergent integral by extracting its asymptotic form and evaluating it in closed form. This is done by stating that

$$\begin{aligned}
F_0(\beta) &= \int_0^{\infty} \tilde{f}(\alpha, \beta) d\alpha \\
&= \int_0^{\infty} [\tilde{f}(\alpha, \beta) - \tilde{f}_{\infty}(\alpha, \beta)] d\alpha + \int_0^{\infty} \tilde{f}_{\infty}(\alpha, \beta) d\alpha
\end{aligned} \tag{9}$$

where  $\tilde{f}_{\infty}(\alpha, \beta)$  is the asymptotic form of the integrand. For cases where convergence is slow, the asymptote is usually of the form

$$\tilde{f}_{\infty}(\alpha, \beta) = C(\beta) \frac{\alpha}{\alpha^2 + \beta^2} J_k(\alpha w/2) J_l(\alpha w/2) \tag{10}$$

with  $C(\beta)$  a complex function. When  $|k - l| = 2s$  with  $s$  an integer (as was the case in [4]), the second integral in the final expression of (9) is given in closed form by [10]

$$\int_0^{\infty} \tilde{f}_{\infty}(\alpha, \beta) d\alpha = \begin{cases} C(\beta) (-1)^k I_k(\beta w/2) K_l(\beta w/2) & k \geq l \\ C(\beta) (-1)^l I_l(\beta w/2) K_k(\beta w/2) & k < l \end{cases} \tag{11}$$

where  $I_m(x)$  and  $K_m(x)$  are modified Bessel functions of the first and second kind respectively.

However, when  $|k - l| = 2s + 1$  (i.e. an odd integer), this integral is not available in closed form. We therefore need to modify the expression for  $\tilde{f}_{\infty}(\alpha, \beta)$  by replacing the Bessel functions with their respective large argument forms [11], so that

$$\tilde{f}_{\infty}(\alpha, \beta) = C(\beta) \frac{\alpha}{\alpha^2 + \beta^2} \frac{(-1)^{(k+l+1)/2}}{\pi \alpha w/2} \cos(\alpha w) \tag{12}$$

and

$$\int_0^{\infty} \tilde{f}_{\infty}(\alpha, \beta) d\alpha = C(\beta) \frac{(-1)^{(k+l+1)/2}}{\beta w} e^{-\beta w} \tag{13}$$

The first term in the final expression of equation (9) is then a rapidly convergent integral, and is suitable for efficient numerical computation with a routine such as QDAGI [9].

#### 4. Example

Comparing the basis functions shown in Figure 3 with the conventional trigonometric bases in [3], [6] and [7], shows that the two sets of functions are similar in form. The use of the Chebyshev bases instead of the trigonometric bases, therefore does not result in a reduction (or an increase) in the number of unknowns. For a given accuracy level of the final result, the same number of bases should be included in the expansions, irrespective of the type of basis functions used. When the special calculation techniques described here are *not* used, the CPU time required to compute the integrals is also largely insensitive

to the choice of basis functions.

However, if we treat oscillatory integrals as Fourier integrals, and apply asymptotic extraction to slowly converging integrals, the required CPU time is reduced significantly. As an example, we consider certain matrix elements that are calculated during the analysis of the semi re-entrant (SRE) microstrip section [6]. This structure is ideally suited to illustrate these techniques, since it comprises of both a single strip and a pair of strips. Instead of the conventional trigonometric bases used by the authors in [6], we now utilize the appropriate basis functions specified in Table 1 to calculate the following elements :

1.  $P_{11}^{11}(\beta)$  for an even type mode:

From the definition of the matrix elements [6, eq. (9)], we see that

$$\begin{aligned} P_{11}^{11}(\beta) &= \int_{-\infty}^{\infty} Z_{xx}^{11}(\alpha, \beta) \tilde{f}_{x1}^1(\alpha) \tilde{f}_{x1}^1(\alpha) d\alpha \\ &= 2 \int_0^{\infty} Z_{xx}^{11}(\alpha, \beta) \tilde{f}_{x1}^1(\alpha) \tilde{f}_{x1}^1(\alpha) d\alpha \end{aligned} \quad (14)$$

where  $\tilde{Z}_{xx}^{11}(\alpha, \beta)$  is an element of the spectral dyadic Green's function, while  $\tilde{f}_{x1}^1(\alpha)$  is a Fourier transformed basis function for the  $x$  directed current on the single strip. From Table 1, it follows that  $\tilde{f}_{x1}^1(\alpha) = \tilde{f}_2(\alpha, w_1)$ , which yields

$$P_{21}^{11}(\beta) = -8\pi^2 \int_0^{\infty} \frac{Z_{xx}^{11}(\alpha, \beta)}{\alpha^2} J_2(\alpha w_1/2) J_2(\alpha w_1/2) d\alpha \quad (15)$$

If we compare this to equation (8), we see that  $A_0 = -8\pi^2$  and  $A_i = 0$  when  $i \neq 0$ . The integral  $F_0(\beta)$  is evaluated as indicated in equation (9). An expression for  $C(\beta)$  is obtained by calculating the Green's function element for  $\alpha \gg \beta$ , so that

$$Z_{xx}^{11}(\alpha, \beta) \rightarrow \frac{\alpha^3}{\alpha^2 + \beta^2} \frac{j}{\omega \epsilon_0 (1 + \epsilon_{r2})} \quad (16)$$

and

$$C(\beta) = \frac{j}{\omega \epsilon_0 (1 + \epsilon_{r2})} \quad (17)$$

2.  $Q_{32}^{12}(\beta)$  for an even type mode:

From [6, eq. (9)], we see that

$$\begin{aligned} Q_{32}^{12}(\beta) &= \int_{-\infty}^{\infty} Z_{xz}^{12}(\alpha, \beta) \tilde{f}_{z2}^2(\alpha) \tilde{f}_{x3}^1(\alpha) d\alpha \\ &= 2 \int_0^{\infty} Z_{xz}^{12}(\alpha, \beta) \tilde{f}_{z2}^2(\alpha) \tilde{f}_{x3}^1(\alpha) d\alpha \end{aligned} \quad (18)$$

Substituting the bases yields

$$Q_{32}^{12}(\beta) = j 12 \pi^2 w_2 \int_0^{\infty} \frac{Z_{zz}^{12}(\alpha, \beta)}{\alpha} J_1(\alpha w_2/2) J_6(\alpha w_1/2) \sin(\alpha \tau) d\alpha \quad (19)$$

where  $\tau = d + w_2/2$ . The complex constants in (8) are thus given by  $A_1 = j 12 \pi^2 w_2$  and  $A_i = 0$  when  $i \neq 1$ .  $F_1(\beta)$  is calculated as a Fourier integral.

3.  $S_{31}^{22}(\beta)$  for an odd type mode:

From the matrix element definition, it follows that

$$S_{31}^{22}(\beta) = 2 \int_0^{\infty} Z_{zz}^{22}(\alpha, \beta) \tilde{f}_{z1}^2(\alpha) \tilde{f}_{z3}^2(\alpha) d\alpha \quad (20)$$

which reduces to

$$\begin{aligned} S_{31}^{22}(\beta) &= 2 \pi^2 w_2^2 \int_0^{\infty} Z_{zz}^{22}(\alpha, \beta) J_0(\alpha w_2/2) J_2(\alpha w_2/2) \sin^2(\alpha \tau) d\alpha \\ &= \pi^2 w_2^2 \int_0^{\infty} Z_{zz}^{22}(\alpha, \beta) J_0(\alpha w_2/2) J_2(\alpha w_2/2) d\alpha \\ &\quad - \pi^2 w_2^2 \int_0^{\infty} Z_{zz}^{22}(\alpha, \beta) J_0(\alpha w_2/2) J_2(\alpha w_2/2) \cos(2\alpha \tau) d\alpha \\ &= A_0 F_0(\beta) + A_6 F_6(\beta) \end{aligned} \quad (21)$$

The  $F_6(\beta)$  term is treated as a Fourier integral with the cosine as kernel, while the integral  $F_0(\beta)$  is calculated by extracting its asymptotic form. The latter is done by noting that for  $\alpha \gg \beta$

$$Z_{zz}^{22}(\alpha, \beta) \rightarrow \frac{\alpha}{\alpha^2 + \beta^2} \left[ \frac{j\beta^2}{\omega \epsilon_0 (\epsilon_{r2} + \epsilon_{r3})} - \frac{j\omega \mu_0}{2} \right] \quad (22)$$

so that

$$C(\beta) = \frac{j\beta^2}{\omega \epsilon_0 (\epsilon_{r2} + \epsilon_{r3})} - \frac{j\omega \mu_0}{2} \quad (23)$$

These matrix elements were calculated on a Persetel PS8/90-3 computer, in the one case by utilizing the special techniques described in section 3, and in the other case by simply integrating the integrands as defined in equations (14), (18) and (20). The calculations were performed for an SRE structure with dimensions  $w_1/\lambda_0 = 0.01$ ,  $w_2/\lambda_0 = 0.02$ ,  $d/\lambda_0 = 0.005$ ,  $t/\lambda_0 = 0.01$ ,  $s/\lambda_0 = 0.0025$ ,  $\epsilon_{r2} = \epsilon_{r3} = 2.2$ , and with  $k_0/\beta = \lambda/\lambda_0 = 0.7$ . The integrals were calculated with a relative accuracy criterion of 0.001 (i.e. the error should be smaller than 0.1% of the absolute value of the final result). The CPU times required to

calculate the matrix elements using the two approaches are shown in Table 2.

Element	CPU time utilizing special techniques (seconds)	CPU time without special techniques (seconds)
$P_{11}^{11}(\beta)$	0.37	6.72
$Q_{32}^{12}(\beta)$	0.20	0.93
$S_{31}^{22}(\beta)$	0.74	12.15

Table 2 CPU time required to calculate the different matrix elements.

For these examples, the calculation of elements with oscillatory integrands as Fourier integrals, and the application of asymptotic extraction reduce the CPU time by factors of about 4.5 and 18 respectively.

## 5. Conclusion

Suitable basis functions for the expansion of unknown electric currents or fields as required by the spectral domain method applied to a symmetrical planar transmission line, have been provided. We have shown how through using these basis functions, the required CPU time for the matrix element calculations may be reduced appreciably. Elements with oscillatory integrands are treated as Fourier-type integrals, while asymptotic extraction is performed to enhance the convergence rate of integrals with non-oscillatory integrands. Application of the latter technique has been limited to structures with single strips or slots, but with the additional information furnished in this paper, this procedure may now be utilized during the analysis of any symmetrical multiconductor transmission line.

## References

- [1] R.H. Jansen, "The Spectral-Domain Approach for Microwave Integrated Circuits", *IEEE Trans. Microwave Theory Tech.*, Vol. MTT-33, No. 10, pp. 1043-1056, Oct. 1985.
- [2] T. Itoh, "Spectral Domain Immitance Approach for Dispersion Characteristics of Generalized Printed Transmission Lines", *IEEE Trans. Microwave Theory Tech.*, Vol. MTT-28, No. 7, pp. 733-736, Jul. 1980.
- [3] E.G. Farr, C.H. Chan and R. Mittra, "A Frequency-Dependent Coupled-Mode Analysis of Multiconductor Microstrip Lines with Application to VLSI Interconnection Problems", *IEEE Trans. Microwave Theory Tech.*, Vol. MTT-34, No. 2, pp. 307-310, Feb. 1986.
- [4] R. Janaswamy and D.H. Schaubert, "Dispersion Characteristics for Wide Slotlines on Low-Permittivity Substrates", *IEEE Trans. Microwave Theory Tech.*, Vol. MTT-33, No. 8, pp. 723-726, Aug. 1985.
- [5] R. Janaswamy and D.H. Schaubert, "Characteristic Impedance of a Wide Slotline on Low-Permittivity Substrates", *IEEE Trans. Microwave Theory Tech.*, Vol. MTT-34, No. 8, pp. 900-902, Aug. 1986.
- [6] J.C. Coetzee and J.A.G. Malherbe, "Analysis of a semi re-entrant microstrip coupler", *J. Electromagnetic Waves Appl.*, Vol. 7, No. 4, pp.513-531, 1993.
- [7] T. Itoh, *Numerical Techniques for Millimeter-Wave Passive Structures*, Wiley, New York, 1989.
- [8] G.B. Arfken, *Mathematical Methods for Physicists*, Academic Press, New York, 1970.
- [9] IMSL MATH/LIBRARY, Version 2.0, IMSL, Houston, 1991.
- [10] I.S. Gradshteyn and I.M. Ryzhik, *Tables of Integrals, Series and Products*, Academic Press, New York, 1965.
- [11] M.R. Spiegel, *Mathematical Handbook of Formulas and Tables*, McGraw-Hill, New York, 1968.

# PARALLEL IMPLEMENTATION OF THE NUMERICAL ELECTROMAGNETICS CODE

D.C. Nitch and A.P.C Fourie  
Department of Electrical Engineering  
University of the Witwatersrand  
South Africa

## ABSTRACT

NEC2 is a 10 000 line, public domain, FORTRAN IV program for electromagnetic analysis. This program has been adapted for use on transputer networks of various dimension. The FORTRAN code has been modified and translated into OCCAM where necessary. Parallel algorithms were developed and implemented for each NEC2 function in order to optimise efficiency. Execution efficiencies in excess of 80% were attained.

## 1 INTRODUCTION

The Numerical Electromagnetics Code NEC2 (Burke, 1981a, 1981b, 1981c) was originally intended to run on Mainframe computers but has recently been ported to run on personal computers (PC). The main problem with running NEC2 on a PC is that it is exceedingly slow and insufficient memory limits the size of structures that can be analyzed. Stellenbosch University (Le Roux, 1988) compiled NEC to run on a single T800 INMOS transputer and showed that this ran much faster than the PC version. NEC2 was later extended (Nitch and Fourie, 1990) to run on a fixed 16 transputer network with only two of the main algorithms rewritten to execute in parallel. The following disadvantages were apparent:

- The matrix was returned in full to the host transputer which meant that problem size was limited by the memory on the host transputer.
- Many algorithms were still sequential.
- The transputer network was of fixed dimension

This paper presents solutions to these problems. It is acknowledged that the transputer (T800) is quite an old chip and is relatively slow. The parallel algorithms discussed in this paper, however, may also be applied to contemporary distributed-memory parallel processing machines.

## 2 BACKGROUND TO NEC

Structures are modelled by wire segments with options to include sources, loads and networks. These structures may be analyzed in various environments (free space, ground etc). Essentially NEC calculates the interaction between the  $N$  wire segments making up the structure and hence obtains an  $N \times N$  matrix. An excitation vector is then calculated as a function of the sources. Solving this matrix equation yields the currents on each segment in the structure. Mathematically this may be expressed as :

$$\begin{bmatrix} Z_{11} & Z_{12} & \dots & Z_{1N} \\ Z_{21} & Z_{22} & \dots & Z_{2N} \\ \cdot & \cdot & \cdot & \cdot \\ \cdot & \cdot & \cdot & \cdot \\ Z_{N1} & Z_{N2} & \dots & Z_{NN} \end{bmatrix} \times \begin{bmatrix} I_1 \\ I_2 \\ \cdot \\ \cdot \\ I_N \end{bmatrix} = \begin{bmatrix} E_1 \\ E_2 \\ \cdot \\ \cdot \\ E_N \end{bmatrix}$$

where  $Z_{ij}$  is the interaction between segment  $i$  and  $j$  and is a function of the wire geometry  
 $I_i$  is the current on segment  $i$ , which is obtained by solving the equation.  
 $E_i$  is the excitation on segment  $i$  which is calculated from the specified sources.

Once the currents on the segments are found, other electromagnetic characteristics such as electromagnetic (EM) fields may be found.

The sequence of possible events carried out by the program is as follows:

- The structure geometry is read from a file
- The  $Z$ -matrix is filled by calculating the interaction between segments. This requires  $N^2$  operations each of which involves numerical integration.
- The  $Z$ -matrix is factorized which requires  $N^3$  simple operations.
- The  $E$ -vector is calculated from the sources.
- Solve for currents which requires  $N^2$  simple operations.
- The effect of  $I$  networks are found by  $I$  solve operations on the  $Z$ -matrix and modifications of the  $E$ -vector.

- A single EM field value is calculated by summing the effect of the structure currents at that point. This involves  $MN$  operations for  $M$  field points.

NEC allows structure symmetry to be exploited in order to reduce computational effort for filling and factoring the matrix. This involves alteration to the fill, factor and solve of the matrix which will be discussed in more detail.

### 3 PARALLEL ARCHITECTURE AND COMMUNICATION

The transputer (INMOS, 1989) is a single chip micro-processor with 4 communication links for direct communication to other transputers. The general architecture used for the parallel implementation is shown in Figure 1. It should be noted that this architecture may be generalised for processors that have more than 4 communication links.

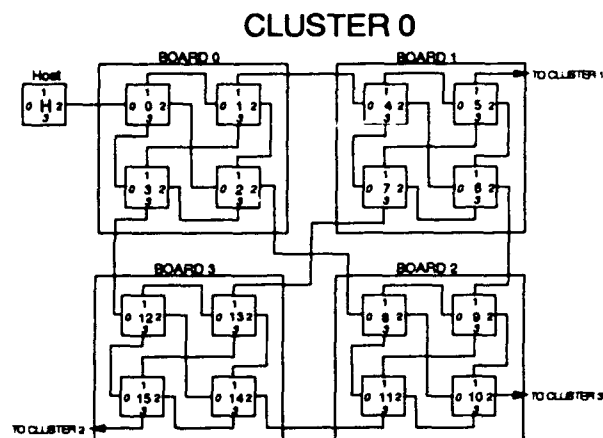


Figure 1: The transputer network.

The reasons for choosing this architecture are :

- the path from any processor to any other processor in the network is minimized when compared to other networks investigated (various meshes, hypercubes etc.).
- the algorithm controlling the communication is simple.
- extending or reducing the network dimension is easy. This extension or reduction may, in most cases, be achieved by adding or removing single processors from the network.

Three general communication strategies were required:

- Broadcast from host to network.
- Send from all transputers to host.
- Broadcast from any transputer to the rest of the network.

Each transputer has knowledge of the network size and a number identifying its position in the network. From this information it is possible to deduce the network interconnections for any processor. All unconnected links are ignored when executing the algorithms described below.

#### 3.1 Broadcast from host to network.

All transputers wait on link 0 for a message. Upon receipt:

- the main transputer on a board whose identity is ( $proc.id \text{ REM } 4 = 0$ ) sends the message on links 1 to 3. (The variable  $proc.id$  is the number identifying the processor in the network, whilst the  $REM$  function calculates the remainder of the division of  $proc.id$  and 4.)
- otherwise if the processor is not the main transputer on a board, then send out to next board or cluster if connected.

#### 3.2 Send from all transputers to host

All transputers send their own message out on link 0. Transputers listen on links 1 to 3 for messages which will be routed through them and passed on through link 0.

#### 3.3 Broadcast from any transputer to network

The broadcasting transputer sends its message on all four links. Other transputers redirect the message in the following way:

- If the broadcaster is on the same board as the receiver then only redirect to other boards or clusters
- If the broadcaster is not on the same board as the receiver then the receiving processor redirects the message to the rest of the processors on its board and to connected clusters (not other connected boards).

### 4 IMPLEMENTATION OF PARALLEL ALGORITHMS

#### 4.1 Matrix filling

Inherently the matrix filling requires each transputer to have knowledge of the structure and the environment in which it is situated. This information is broadcast from the host to the transputer network. This enables each transputer to calculate any matrix element independently of other transputers. It is important to decide on which part of the matrix each processor should fill. The following points require consideration :

- Each processor should calculate approximately the same number of matrix elements.

- Each processor should calculate that part of the matrix which it requires for later operations. The reason being that the matrix occupies a large portion of the memory and hence it is difficult to reshuffle efficiently. In the previous implementation (Nitch and Fourie, 1990), the matrix was returned to the host for reordering. This method obviously did not make efficient use of the distributed memory.

The matrix was filled by rows because:

- both column and row distribution reduce the communication overhead during matrix factoring when compared to the overhead when the matrix is divided into blocks.
- later factoring of the cyclic block matrix (as a result of structure symmetry) requires that it be in row form to reduce communication overhead.

Wrap mapping of rows was employed for load balancing in the factoring algorithm since the diagonal elements of the Z-matrix were generally the largest.

## 4.2 Matrix factoring

The matrix in NEC is solved using Gaussian elimination with back substitution. The parallel implementation of this algorithm was based on the algorithm presented in a paper by Giest and Romine (1988) and is shown in Figure 2.

```

FOR k = 0 TO n-1
  determine pivot row using parallel search
  update permutation vector
  IF (I own pivot row)
    broadcast pivot row
  ELSE
    receive pivot row
  ENDIF
  FOR (all rows i>k that I own)
     $l_{ik} := a_{ik}/a_{kk}$ 
    FOR j = k+1 TO n-1
       $a_{ij} := a_{ij} - l_{ik}a_{kj}$ 
    ENDFOR
  ENDFOR
ENDFOR

```

Figure 2: The parallel algorithm presented by Giest and Romine.

Where  $l$  is a temporary vector housing the pivot column.

Implementing this algorithm on a network of transputers requires that, for good load balancing, the rows of the matrix are wrapped onto the processors (i.e for a network of 16 processors the first processor should have rows 1, 17, 33 etc the second processor should have rows 2, 18, 34 and so on). The reason for the wrapped row mapping is that once a processor has operated on the pivot column (column  $k$ ), row  $k$  is not used in any calculation for the completion of the algorithm. The

work load of the processor is therefore reduced. Thus to ensure that the processors each have equal loads throughout the execution of the algorithm, a wrapped row mapping is employed.

The communication between processors during the computation involves only the broadcast and reception of the pivot column.

## 4.3 Matrix solve

Consider the lower triangular linear system

$$Lx = b$$

where  $L$  is a lower triangular matrix of order  $n$   
 $b$  is the right-hand side vector of dimension  $n$   
 $x$  is the unknown solution vector

The serial solution of this system may be represented by the code

```

FOR i = 1 TO n
  FOR j = 1 TO i-1
     $b_i = b_i - x_j L_{ij}$ 
  ENDFOR
   $x_i = b_i/L_{ii}$ 
ENDFOR

```

Parallel matrix solve algorithms have been developed by Guangye and Coleman (1988), and Heath and Romine (1988), and others. The matrix solve routine used in this implementation was based on an algorithm presented by Heath and Romine (1988) and is shown below :

```

FOR j = 1 TO n
  IF (I have row j) THEN
     $x_j = b_j/L_{jj}$ 
  ENDIF
  fan-out ( $x_j$ ,  $map(j)$ )
  FOR (all rows i>j that I own)
     $b_i = b_i - x_j L_{ij}$ 
  ENDFOR
ENDFOR

```

The function  $map(j)$  relates a processor to the row  $j$ . Thus the line  $fan-out(x_j, map(j))$  sends the message  $x_j$  to the processor with row  $j$ .

## 4.4 Field calculations

Given below is the sequential code used in NEC for the far field calculation.

```

FOR phi = 1 TO noOfPhiPoints
  FOR theta = 1 TO noOfThetaPoints
    FOR i = 1 TO N
      calculate field at (phi,theta) due to current
    i
      vectorially add field at (phi, theta)
    ENDFOR
    write out field at (phi, theta)
  ENDFOR
ENDFOR

```

At the end of a single pass through the inner loop, the results are written to disk.

#### 4.4.1 Field calculation code for the network processors

There are a number of ways one can split up the nested *FOR* loops for execution in parallel. Either the phi, the theta or both loops may be divided amongst the processors. The number of theta and number of phi points are not necessarily the same for each radiation pattern request. Thus splitting the phi or theta loops could produce very poor performance figures.

The method that is employed finds the total number of radiation points for the field calculation and hence reduces it to a single loop. These points are divided amongst the processors and each processor finds the field at these points. Implementing this method requires the decoding of radiation pattern point number to the (theta, phi) point in space.

```

FOR points = 1 TO noOfPhiPoints*noOf-
ThetaPoints
  calculate phi
  calculate theta
  FOR i = 1 TO N
    calculate field at (phi,theta) due to current
  i
    vectorially add field at (phi, theta)
  ENDFOR
  write out field at (phi, theta)
ENDFOR

```

Splitting the loop amongst transputers in order to achieve parallel execution has some difficulties. The transputers in the network do not have access to disk and memory will be wasted if all the fields are stored. The loop must hence be further subdivided such that a specified number of fields are calculated before information is relayed to the host.

An algorithm employing this subdivision was developed for the transputer network.

#### 4.4.2 Field calculation code for the host processor

The principle behind the algorithm for the host processor is as follows :

```

FOR i = 1 TO noOfGroupsOfPoints
  request network to find radiation pattern
  for
  group of points
  FOR p = 1 TO noOfProcessors
    FOR j = 1 TO noOfPointsPerProcessor
      receive radiation pattern
      write result to disk
    ENDFOR
  ENDFOR
ENDFOR

```

The deficiency in this algorithm is that it has two main serial components. The first is the request to the network to find the radiation pattern for a group of points and the second is the writing of the results to disk. Thus the network waits for the host to write the results to disk before computing the next set of fields.

This serial component can be masked by buffering the radiation patterns received from the host. A request to find the next set of radiation pattern points may be made before writing the present results to disk. Thus at the expense of memory, the parallel execution can be sped up. An algorithm employing such a buffering scheme was implemented in the parallel NEC.

#### 4.5 Networks

Networks are evaluated in NEC through the use of a small network matrix with dimension equal to the number of networks.

The following steps need to be performed for the networks in the structure:-

```

Generate the RHS vector of the network matrix
equation (Step a)
Fill network matrix (Step b)
FOR i = 1 TO noOfNetworks
  Solve the Z-matrix to get a modification vector
  (Step c)
  use modification vector to adapt network matrix
  (Step d)
ENDFOR
Factor the network matrix (Step e)
Modify RHS of network matrix equation (Step f)
Solve network equations for voltage across ports of
those networks without voltage sources. (Step g)

```

The computationally time consuming portion of this solution is filling the network matrix (steps b, c and d). Steps a and b are carried out by the host while the transputer network is filling and factoring the Z-matrix. Step c requires the use of the factorised Z-matrix to find the modification vector. While c is performed in parallel on the network, d can be made to execute concurrently on the host.

Arranging the code in this manner enables the host processor and the network to work in parallel. First, the host processor fills the network matrix while the network fills and factors the much larger Z-matrix. Then the network finds the modification vector (using the parallel algorithm for solving discussed before), while the host processor uses a previously computed modification vector to update the network matrix. Using this technique the time required to fill the network matrix is approximately equal to the time required to find the modification vectors.

The remaining steps are comparatively fast. There is little point in factoring the network matrix on the transputer network since the matrix is generally of small dimension (30x30) and the efficiency of the network when factorising such matrices is low. The solution of a matrix of this dimension is not very time consuming.

#### 4.6 Cyclic Block matrices

Memory and Computation time is saved when the structure being simulated is symmetric. The time required to fill the matrix is reduced since only the interactions between those segments in the first symmetric section and the structure are calculated. Hence the filling routine is simplified to :

```

FOR i = 1 TO noOfSegs
  FOR j = 1 TO noOfSegsInSymSection
    find interaction between segments i and j i.e
    Zij
  ENDFOR
ENDFOR

```

The resulting matrix is structured as shown below.

$$[A_1 \ A_2 \ \dots \ A_M] \times \begin{bmatrix} I_1 \\ I_2 \\ \cdot \\ \cdot \\ \cdot \\ I_N \end{bmatrix} = \begin{bmatrix} E_1 \\ E_2 \\ \cdot \\ \cdot \\ \cdot \\ E_N \end{bmatrix}$$

where

$$A_i = \begin{bmatrix} Z_{11} & Z_{12} & \dots & Z_{1s} \\ Z_{21} & Z_{22} & \dots & Z_{2s} \\ \cdot & \cdot & \cdot & \cdot \\ \cdot & \cdot & \cdot & \cdot \\ \cdot & \cdot & \cdot & \cdot \\ Z_{s1} & Z_{s2} & \dots & Z_{ss} \end{bmatrix}$$

and s is the number of segments in a symmetric section.

The solution of this system of equations is accomplished using the following steps:

- Each submatrix is combined using the formula

$$A_i = \sum_{k=1}^M S_{ik} A_k.$$

where  $A_i$  is the  $i^{\text{th}}$  submatrix.

$S_{ik}$  are factors calculated according to the type of symmetry.

$M$  is the number of submatrices

- Each submatrix is factored.
- The excitation vector is filled in the normal fashion.
- Each submatrix equation is solved.
- The resulting solutions are combined using

$$I_i = \sum_{k=1}^M S_{ik} I_k \text{ to find the currents on the segments.}$$

where  $I_i$  is the solution to the  $i^{\text{th}}$  submatrix equation.

Execution of these steps in parallel may be considered in two sections, namely, the filling and the solution of the submatrices.

The filling of the matrix is split up by asking each processor in the network to fill specific rows. It is important that processors fill rows of the Z-matrix, since the formula used to combine the submatrices operate on the rows of the submatrices. Thus, once the matrix has been filled, each processor can combine the elements of its portion of the submatrices without having to communicate with other processors.

Solving the submatrix equations is accomplished by sequentially factoring and solving each of the submatrix equations on the network. The resulting solutions are

then combined using  $I_i = \sum_{k=1}^M S_{ik} I_k$  to give the currents on the structure.

#### 5 PARALLEL PERFORMANCE

In assessing the performance of an algorithm on a network of transputers, it is useful to compare the time taken to complete the task on the network to the time taken on one

processor. Thus in gauging the performance of the parallel NEC, the efficiency and speedup of the computation were calculated.

Efficiency and speedup are defined as follows :-

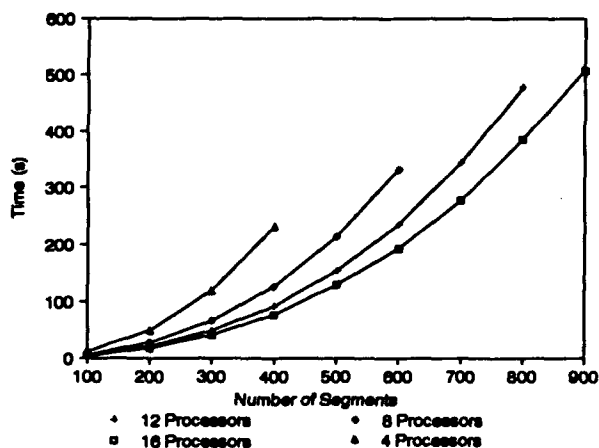
$$\text{Efficiency} = \frac{\text{time taken to complete task on one processor}}{(\text{time taken to complete task on } p \text{ processors}) \times p}$$

$$\text{Speed Up} = \frac{\text{time taken to complete task on one processor}}{\text{time taken to complete task on } p \text{ processors}}$$

where the time taken to complete the task on p processors is made up of the time spent communicating between processors and the time spent doing the computation.

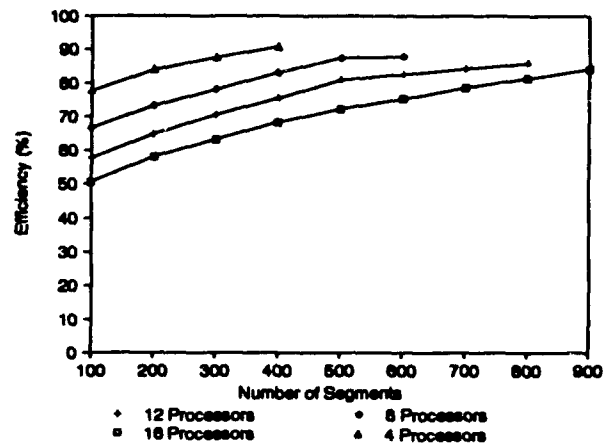
Calculating the efficiency and speedup of the parallel NEC requires the times for simulating problems on both a single processor and on the network. Since full use of the distributed memory is used in the simulations, a single transputer with the same amount of memory as the network should be used. However, a processor with this amount of memory was not available. It is possible to predict the time that it would take for a single processor to do a simulation. Thus the efficiency and speedup graphs use some predicted values.

Graph 1 shows the times taken to simulate structures of various electrical size on processor networks consisting of 4, 8, 12, and 16 processors.

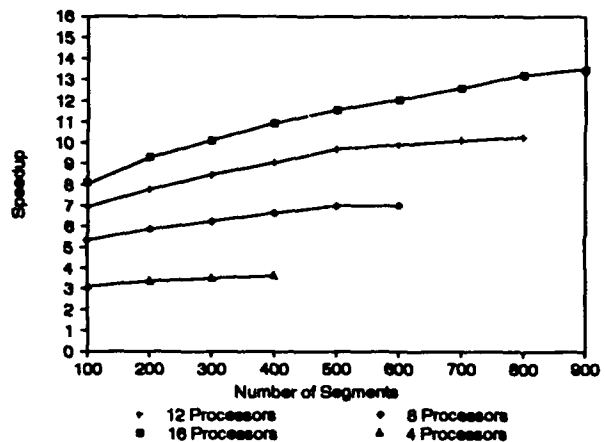


Graph 1 : The times taken to simulate structures of varying electrical size.

Graph 2 gives the efficiency of the transputer networks and graph 3 gives the speedup of the simulations.



Graph 2 : The efficiency of the transputer network.



Graph 3 : The speedup of various transputer networks for structures of varying electrical size.

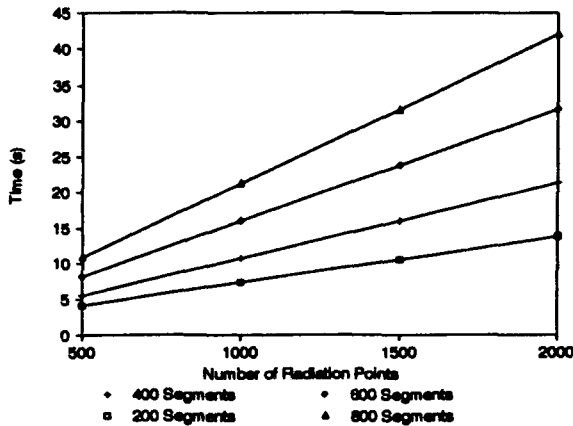
### 5.1 Radiation Pattern Performance

Analysis of the performance of the transputer network when calculating radiation patterns is difficult since there are many factors influencing the performance. These factors include :

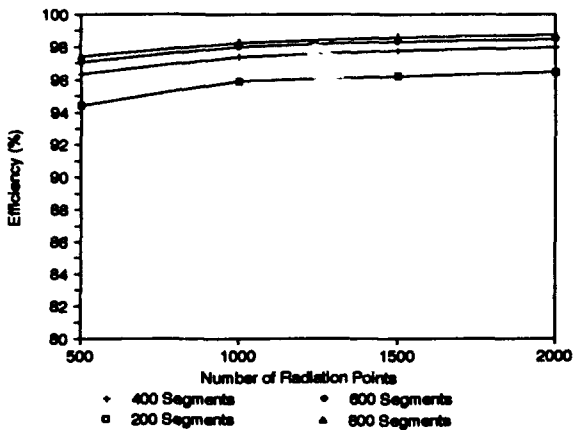
- the number of radiation pattern points requested.
- the number of segments in the structure.
- the number of processors in the network.
- the number of points returned to the host at a time.
- the speed of the disk.

When computing a large number of radiation pattern points for a structure consisting of a few segments there is a bottle-neck at the disk since the network calculates the points faster than they can be output to disk.

The performance of the far field algorithms are illustrated in graphs 1 and 5. Graph 4 shows the time required to find a number of radiated fields on structures of varying dimension on 16 processors. Graph 5 gives the efficiency of the process.



Graph 4 : The time required to find a radiation pattern on a 16 processor network.



Graph 5 : The efficiency of the radiation pattern calculation on a 16 processor network.

## 6 CONCLUSION

The speedup attained by the transputer network indicate that it is possible to significantly reduce the execution time of NEC by distributing the program onto a network of processor and executing the code in parallel. Full use of the distributed memory was made by careful consideration of the operations to be performed on the largest data structure (the interaction matrix).

## 7 REFERENCES

Burke G.J., Poggio A.J. (1981a) "Numerical Electromagnetics Code (NEC2) - Method of Moments; Part I : Program Description - Theory", San Diego : Naval Oceans Systems Center, Tech Doc 116.

Burke G.J., Poggio A.J. (1981b) "Numerical Electromagnetics Code (NEC2) - Method of Moments; Part II : Program Description - Code", San Diego : Naval Oceans Systems Center, Tech Doc 116.

Burke G.J., Poggio A.J. (1981c) "Numerical Electromagnetics Code (NEC2) - Method of Moments; Part III : Program Description - User Guide", San Diego : Naval Oceans Systems Center, Tech Doc 116.

Giest G.A., Romine C.H. (1988) "Parallel LU Factorization", *SIAM J. Sci. Statist. Comput.*, Vol.9, No.4, pp.639-649.

Guangye L.I., Coleman T.F. (1988) "A Parallel Triangular Solver for a Distributed Memory Multiprocessor", *SIAM J. Sci. Statist. Comput.*, Vol.9, No.3, pp.485-502.

Le Roux J.J. (1988) "Numerical Electromagnetics Computation using the INMOS T800 Transputer on an Olivetti M24 Personal Computer", *Applied Computational Electromagnetics Society Journal and Newsletter*, Vol.3, No.2, pp.88-94.

Heath M.T., Romine C.H. (1988) "Parallel Solution of Triangular Systems on Distributed Memory Multiprocessors", *SIAM J. Sci. Statist. Comput.*, Vol.9, No.3, pp.589-600.

Nitch D.C., Fourie A.P.C. (1990) "Adapting the Numerical Electromagnetics Code to Run in Parallel on a Network of Transputers" *ACES Journal*, Vol.5, No.2, pp.76-86.

# VALIDATION OF THE MININEC3 CODE FOR COMPLEX RADIATING STRUCTURES

K.P.Murray and B.A.Austin  
Department of Electrical Engineering and Electronics  
University of Liverpool  
PO Box 147  
Liverpool L69 3BX  
United Kingdom

## Abstract

The ability of the MININEC3 code to accurately model complex radiating structures was previously unknown because computer compiler constraints limited the size of analyzable configuration. With the conversion of the code from BASIC to FORTRAN however it is now feasible to use it to simulate such structures. This paper presents the results of a validation exercise aimed at assessing the code's suitability for modelling configurations which involve hundreds of segments.

## 1 Introduction

The MININEC moment method code is sometimes considered erroneously to be merely a more compact version of the widely known Numerical Electromagnetics Code (NEC). There are though significant differences between the algorithms used in the two codes. Of particular importance are the expansion and testing functions used in the representation of the current distribution. MININEC uses a modified Galerkin approach with pulse expansion and testing functions whereas NEC's employs constant-sine-cosine expansion functions and delta testing functions. In certain moment method applications however it is desirable to use a code where the same expansion and testing functions are employed in the representation of the current distribution. One particular application, of interest to the authors, is the calculation of the so-called characteristic modes (Harrington 1975) of a radiating structure. This is facilitated by the solution of a weighted eigenvalue equation involving its generalized impedance matrix  $[Z]$ . If a Galerkin or modified Galerkin moment method code is used in the initial determination of  $[Z]$  then reciprocity between segments is enforced and the matrix is symmetrical. This is highly advantageous as it ensures that the

characteristic modal currents and their associated eigenvalues are real, giving them a clear physical meaning and hence allowing greater insight into a structure's radiation characteristics.

The results presented in this paper relate to a research program concerned with the investigation of the characteristic modes of complex vehicular structures (Murray and Austin 1993) at HF and VHF frequencies. This involved the use of a moment method code with the ability to model such configurations accurately. The need also for identical expansion and testing functions effectively eliminated the use of NEC. Hence the MININEC code was chosen as the basis of the work. A useful feature of NEC and MININEC is the similarity of geometry definition which means that the wide range of available NEC pre- and post-processors could be employed with minimal modification. The one major drawback of using MININEC was that it had not previously been used to model complex geometrical configurations because it was written in BASIC and compiler constraints imposed severe segmentation limits. Conversion of the code to FORTRAN however, as described by Miller (1989a), effectively removed this constraint but its ability to model complex structures accurately was unknown. This paper addresses this issue by showing the results of a MININEC3 validation exercise. Three approaches were adopted using appropriate analytical, NEC-generated and available experimental data.

## 2 Development of the MININEC3 Code

The Mini-Electromagnetics Code (MININEC) was initially developed by Julian *et al* (1982) as a Method of Moments code for the analysis of simple, relatively small (in terms of wavelengths), antenna structures. The original purpose of the code was to provide a tool for the rapid analysis of such simple antennas on small micro or desktop computers. It

allowed the computation of a number of the basic characteristics such as current distribution, input impedance and far-field pattern of an antenna situated in either free space or over an infinite, perfectly conducting ground-plane. There were many limitations to the initial version of MININEC. Point reactive loading was available, although this was not allowed for wire segments intersecting the perfectly conducting ground plane. Also any wire that did intersect the ground plane had to do so at an angle of  $90^\circ$ . In addition computer technology of the time introduced further constraints. Computer memory and the available BASIC compilers limited the size of analyzable geometries to around 30 segments. This meant that the maximum size of antenna that could be handled confidently was of the order of 1 wavelength.

A second version of the code was developed by Li *et al* (1983) which addressed some of the ground plane constraints listed above. The next major step in the progression of the code however was the development of MININEC3 by Logan and Rockway (1986), together with the rapid development of computer technology. Although the program was still written in the BASIC language, compilers were available that could address up to 64k of memory, enabling antenna structures of up to 125 segments or of the order of 8 wavelengths to be analyzed. The relative increase in desktop computer speed also made the analysis of such structures feasible within a reasonable period of time.

This third version of MININEC also included many more of the features that are available with the mainframe NEC code. As with the previous codes, current distribution and hence input impedance, along with far field patterns could be calculated. The feature of point loading the antenna was improved to include the ability to add either fixed or frequency dependant s-domain loading. The antenna could now be situated in either free space or over a perfect or finite conducting ground plane. This feature used the Fresnel reflection coefficient approximation to allow five changes in ground impedance with distance using either circular or linear boundaries. Near fields were also computed, if required.

Other variants of the MININEC code have been developed that have improved the interface with the user and also presented improved routines for the display of calculated data. Such codes are described by Lewallen (1991) and include The MININEC System (Logan 1988), MN4 (Beezley 1992) and ELNEC (Lewallen 1991). Although not improving the capabilities of the basic algorithm or speed, they present an attractive, "user friendly" interface and rapid methods for displaying calculated data graphically.

The algorithms used in the MININEC3 code and its variants provide a reliable, stable method for the calculation of generalized antenna characteristics. There is no theoretical limit to the size of geometry that can be analyzed using these algorithms, although it is limited by two external factors. Firstly, as discussed above, the size of core memory that a BASIC compiler can address limits the physical size of the problem. Secondly, the speed of operation of the computer on which the software is mounted places a further practical constraint on the time available.

The first of these constraints was addressed with the implementation of a version of MININEC3 in FORTRAN as described by Miller (1989a). The FORTRAN programming language overcomes all the inherent constraints of BASIC compilers. There is no theoretical limit to the size of memory that can be addressed and the greater efficiency of the language for numerical calculations improves execution time. Also the code may be used with a wider range of computers including mainframes.

### 3 Validation of MININEC3

Three different approaches will be used in the assessment of the ability of MININEC3 to model complex antenna structures. Firstly the analytical results for the input impedance of a V-dipole antenna are examined. This configuration, with an acute angle between two conductors, has been reported to produce erroneous impedance results with some moment method codes (Austin 1993). Since wire grid models of complex structures frequently contain such acute angles it is therefore important that the ability of MININEC3 to model the situation is considered. Secondly MININEC3 was used to calculate the radiation characteristics of a number of complex wire grid models representing continuous surfaces. These are compared to the results obtained using NEC. Finally the experimentally-determined input impedance of a monopole mounted on a conducting box is compared to the results obtained with MININEC3.

### 4 The V-dipole Antenna

The input impedance of a centre-fed V-dipole antenna in free space was determined analytically by Jones (1976). His results showed excellent agreement with experimentally determined data for a base fed monopole antenna positioned at various angles over a large conducting ground plane. The antenna

configuration used by Jones is shown in figure 1. He varied the angle  $\Psi$  between the two wires from  $30^\circ$  to  $180^\circ$  in  $30^\circ$  increments.

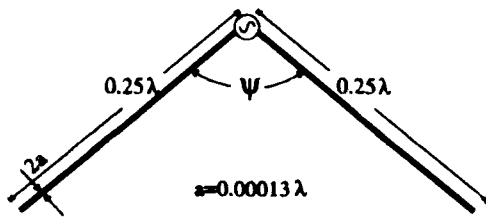


Figure 1. V-dipole antenna.

For the MININEC3 model three uniform and one tapered segmentation scheme were employed and are shown in table I. Schemes 1, 2 and 3 are the uniform segmentation configurations. Notice that schemes 2 and 3 involve higher densities than the generally accepted MININEC3 "rule of thumb" of 20 segments per wavelength of wire. Scheme 4 is the graded segmentation case. This consists of dividing each wire into two equal sections. For the section including the feed-point a higher segmentation density was employed. Figures 2 and 3 then show the predicted input impedances obtained using these four schemes and compares them to those of Jones.

Table I. V-dipole segmentation schemes.

Scheme	1	2	3	4
Total segments	12	20	40	30
Segmentation density (per wavelength)	24	40	80	80 - Region 1 40 - Region 2

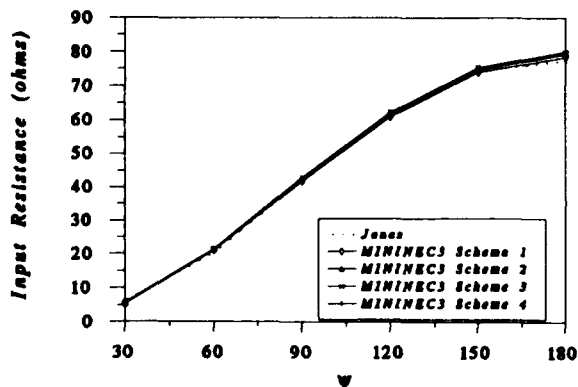


Figure 2. Comparison of analytical and MININEC3 predicted input resistance.

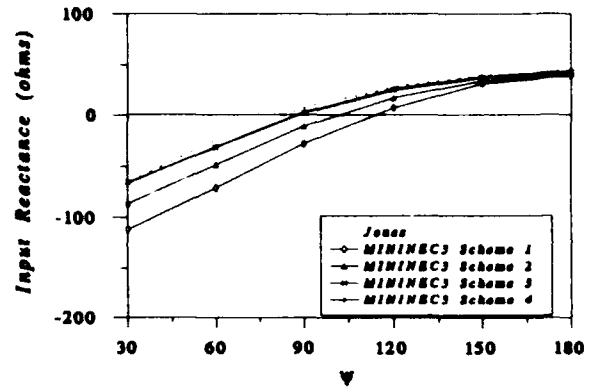


Figure 3. Comparison of analytical and MININEC3 predicted input reactance.

Figure 2 shows that the MININEC3 input resistances obtained with all of the segmentation schemes are virtually indistinguishable from those of Jones. For the input reactance, shown in figure 3, however it is noticeable that as  $\Psi$  is reduced the difference between MININEC3 and the analytical results is substantial for 12 and 20 segments. By contrast schemes 3 and 4 are in excellent agreement for all  $\Psi$ .

It is apparent from these results that MININEC3 is capable of accurately modelling wires with an acute angle provided that an appropriate segmentation scheme is employed. The results here suggest however that only in the local region around the junction between the wires is it necessary to use this relatively dense segmentation scheme. Thus for  $\Psi < 90^\circ$ , schemes 3 and 4 show good agreement compared to the poor agreement of schemes 1 and 2. The advantage of scheme 4 compared to scheme 3 is the reduction in computation time. Tapering the segments in the vicinity of the feed has also been shown by Lewallen (1991) to improve the accuracy significantly.

## 5 Comparison with NEC

The NEC program is the one of the most widely used and highly regarded moment method codes for the analysis of complex antenna systems. Comparing its results to those of MININEC3 is therefore a useful validation exercise. A wide range of continuous surfaces represented by wire grid models were therefore modelled using both codes. This section compares both the predicted far-field patterns and input impedances of two specific geometrical configurations. The first is a  $0.4\lambda \times 0.6\lambda$  flat plate with a monopole mounted in the centre as shown in figure 4. The second is a more

complex box structure containing a aperture and two vertical monopoles as shown in figure 5. Wire grid models of these structures were developed using the mesh generator of Najm (1991). The grid spacing is  $0.1\lambda$  and the so-called equal-area rule was applied to determine the wire radius. Figures 6 and 7 show the resulting wire meshes.

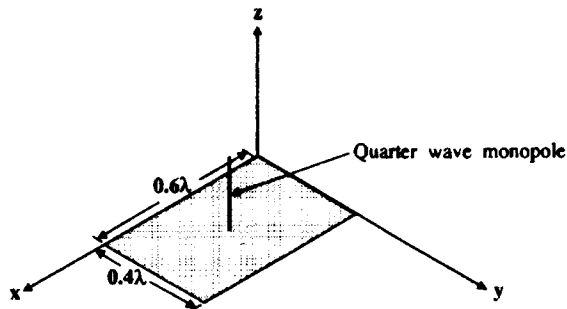


Figure 4. Flat conducting plate with centre mounted monopole.

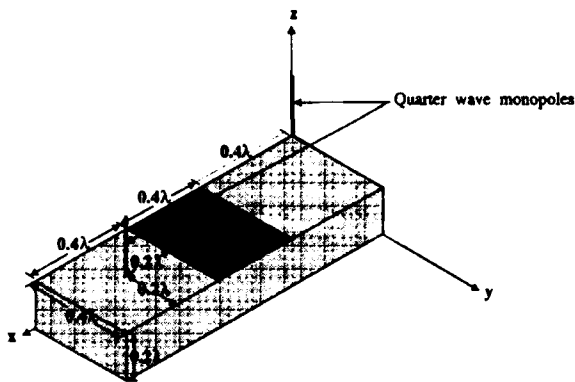


Figure 5. Conducting box with aperture and two monopoles.

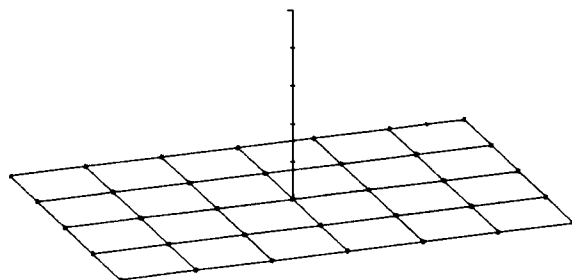


Figure 6. Wire grid model of the geometrical configuration shown in figure 4.

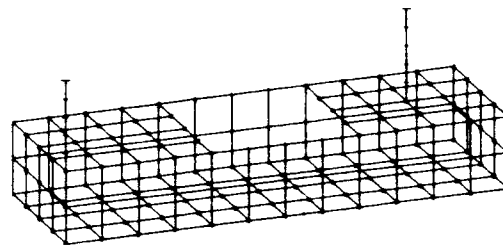
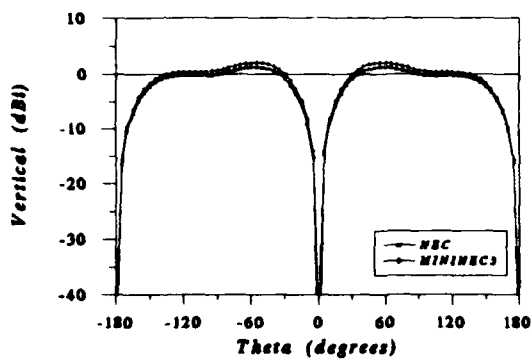


Figure 7. Wire grid model of the geometrical configuration shown in figure 5.

For the first model the monopole was excited with a single voltage source situated at its base. The two monopoles of the second configuration however allowed them to be base fed with voltage sources of different magnitude and phase. This is clearly useful in a validation exercise as numerous dissimilar far-fields are obtainable, as well as complex current flow on the whole structure.

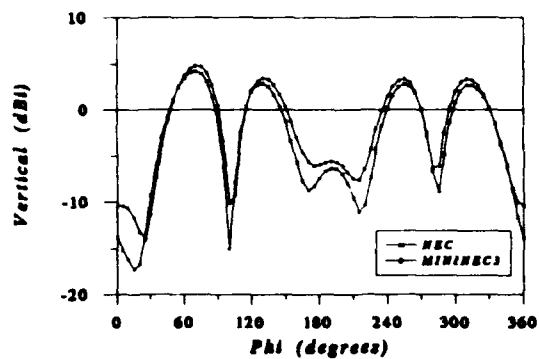
Considering firstly the predicted radiation patterns in free space of the simpler plate configuration, figure 8 shows the variation in elevation of the vertical  $E$ -field component, while figure 9 shows the azimuthal variation of the horizontal  $E$ -field component. Excellent agreement is achieved in each case with a maximum difference of less than 1dB at any point. Next considering the more complex box structure figures 10 and 11 show the azimuthal variation of the vertical  $E$ -field component with the monopoles fed firstly in-phase and secondly in anti-phase. Figures 12 and 13 show the variation in elevation of the horizontal  $E$ -field component for the same feed configurations. Overall the agreement shown for this configuration is reasonably good with the patterns, in general, exhibiting the same shape with nearly identically positioned peaks and nulls. The most noticeable difference in the pattern plots is in the depth of the nulls which in the worst case is up to 5dB. Overall though both codes are predicting substantially similar spatial distributions of power.

Next we consider the input impedance where table II shows the values predicted by both codes. It is noticeable that the largest difference between the two sets of results is in the reactive component. MININEC3 consistently predicts an input reactance that is substantially more capacitive than that of NEC. Miller (1989b) identified a similar effect where different computer models occasionally produce similar results but with a noticeable frequency shift from one another. The overall dimensions of the structures considered here are around the first natural resonance where generally the reactive component of the input impedance is changing rapidly.



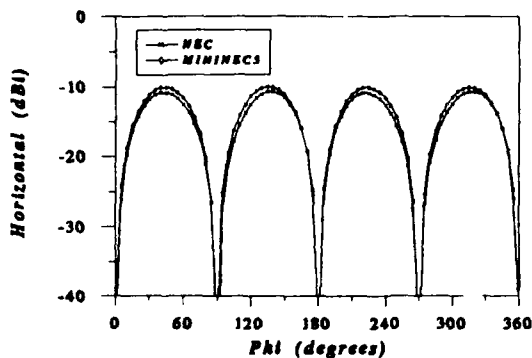
( $\phi=0^\circ$ )

Figure 8. Variation in elevation of the MININEC3- and NEC-predicted vertical  $E$ -field component for the flat plate.



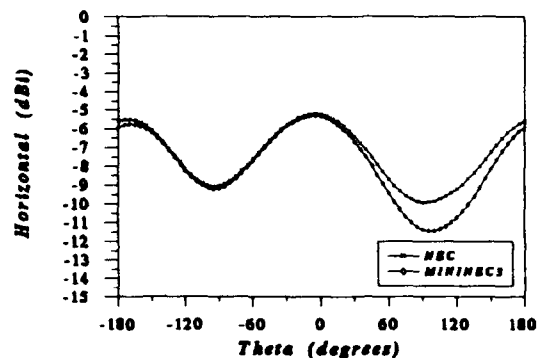
( $\theta=90^\circ$ )

Figure 11. Azimuthal variation of the MININEC3- and NEC-predicted vertical  $E$ -field component for the box with aperture with the monopoles fed in anti-phase.



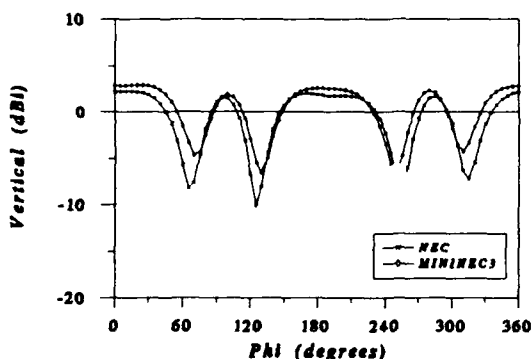
( $\theta=90^\circ$ )

Figure 9. Azimuthal variation of the MININEC3- and NEC-predicted horizontal  $E$ -field component for the flat plate.



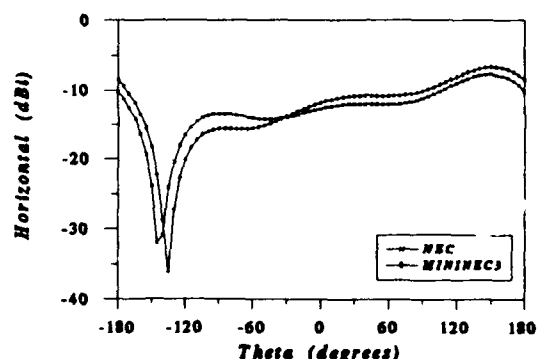
( $\phi=90^\circ$ )

Figure 12. Variation in elevation of the MININEC3- and NEC-predicted horizontal  $E$ -field component for the box with aperture with the monopoles fed in phase.



( $\theta=90^\circ$ )

Figure 10. Azimuthal variation of the MININEC3- and NEC-predicted vertical  $E$ -field component for the box with aperture with the monopoles fed in phase.



( $\phi=90^\circ$ )

Figure 13. Variation in elevation of the MININEC3- and NEC-predicted horizontal  $E$ -field component for the box with aperture with the monopoles fed in anti-phase.

**Table II. NEC and MININEC3 predicted input impedances.**

Geometrical Configuration	NEC	MININEC3
Flat plate	43.34 + j42.43	37.66 + j18.08
Box with cavity (fed in-phase)		
Monopole 1	151.64 + j25.55	148.88 + j7.14
Monopole 2	57.10 + j22.26	39.80 - j1.73
Box with cavity (fed in anti-phase)		
Monopole 1	66.46 + j21.87	54.64 + j1.28
Monopole 2	36.59 + j15.21	27.45 - j4.98

**Table III. NEC and MININEC3 predicted input impedances with an empirically determined frequency shift in the NEC results.**

Geometrical Configuration	NEC Frequency = $0.95f_0$	MININEC3 Frequency = $f_0$
Flat plate	34.46 + j23.21	37.66 + j18.08
Box with cavity (fed in-phase)		
Monopole 1	150.70 + j9.21	148.88 + j7.14
Monopole 2	52.15 + j7.26	39.80 - j1.73
Box with cavity (fed in anti-phase)		
Monopole 1	64.39 - j1.42	54.64 + j1.28
Monopole 2	35.12 - j1.34	27.45 - j4.98

Hence reducing the frequency of the NEC models by an empirically determined value of 5% gives the input impedances shown in table III. The original MININEC results are also shown for comparison.

The frequency shift of 5% clearly reduces the difference between the two sets of impedance results. Whereas the resistive component of the NEC results generally changes negligibly, the NEC-predicted input reactance of each feed-point is reduced considerably. Good agreement is now achieved between the two sets of results. The shift was first thought to be possibly due to the sparseness of the mesh used in the models. It was however, consistently present using mesh densities of up to  $\lambda/60$ .

The closeness of the NEC and MININEC3 far-field and impedance results shown here suggests that MININEC3 is capable of the comparable emulation of the current distribution on complex structures when compared to NEC. The codes use dissimilar expansion

and testing functions to model the current distribution and minor differences in results would therefore be expected. The level of agreement obtained though, especially with the far-fields, proves the validity of using MININEC3 to model complex structures represented as wire grid models.

### 6 Comparison with Experimental Data

As a final test of the ability of MININEC3 to model complex antenna structures accurately we used an appropriate set of experimental data as a reference. Bhattacharya *et al* (1987) measured the input impedance of a monopole antenna mounted on a conducting metal box. The structure was a five sided 10cm cube attached centrally to a 105cm square conducting ground plane. A base-fed 6cm vertical monopole was mounted at

various positions on the upper face of the cube. The radiation patterns of the same configuration were later measured by Chu *et al* (1990) in the same frequency range as Bhattacharya, 1-2GHz.

To model this configuration with MININEC3 a wire grid model was again set up. Each surface of the box was divided into a 6x6 mesh and the equal-area criterion was enforced to calculate the wire radius. The resulting wire grid model is shown in figure 14 with the monopole mounted in the centre. Two simplifications were also made with the MININEC3 model. Firstly the wires of the grid were assumed to be perfectly conducting and secondly the finite conducting ground plane was assumed large enough, in term of wavelengths, to be replaced by a infinite, perfectly conducting ground plane.

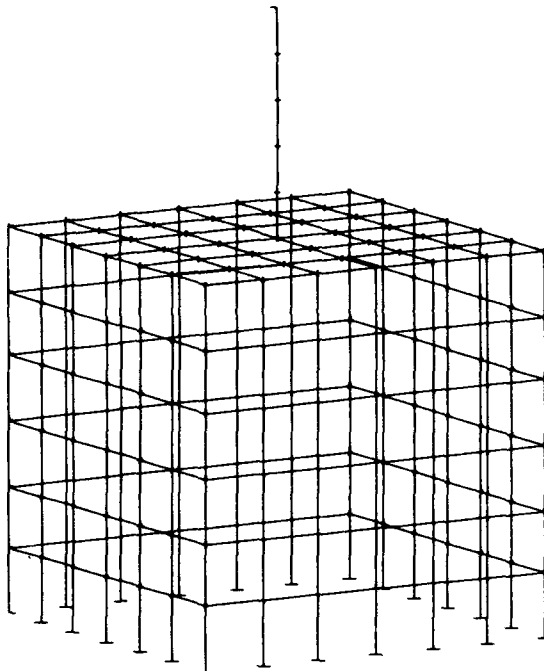


Figure 14. Wire grid representation of the conducting box with centre-mounted vertical monopole.

Figures 15 and 16 compare the MININEC3 predicted input conductance and susceptance with the experimental results of Bhattacharya *et al*. It is noticeable that both the computed and experimental results have a similar trend with a clear, well defined resonance. For both  $G$  and  $B$  however the peak values differ somewhat and there is a noticeable difference between predicted and measured resonant frequency.

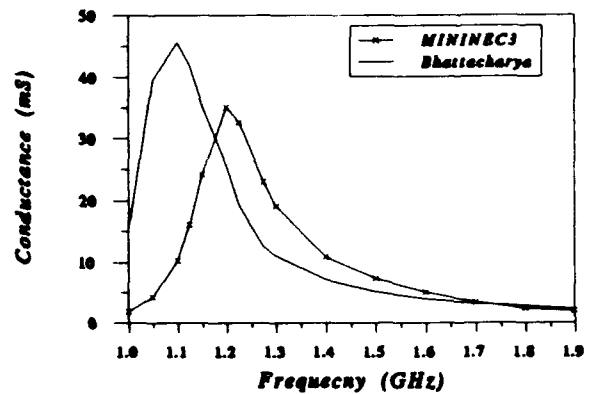


Figure 15. Comparison of experimental and MININEC3-predicted input conductance.

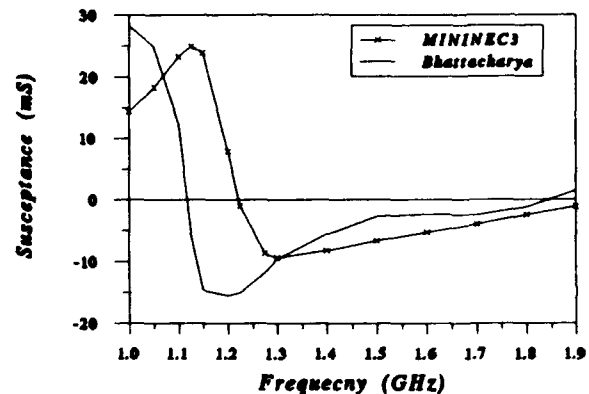


Figure 16. Comparison of experimental and MININEC3-predicted input susceptance.

To test if this difference was due to the inability of the chosen wire grid to represent the continuous surface accurately two further models were developed. Firstly the mesh density was doubled, using a 12x12 grid to model each surface of the cube. Secondly the twice surface area rule was enforced and this yielded a larger wire grid radius. Both of these more refined models however only marginally improved the agreement of the MININEC3 results. These results therefore proved that the MININEC3 model had converged in terms of the necessary grid density and area factor. The discrepancies are therefore probably due to two further factors. Firstly, the assumption made regarding the replacement of the finite ground plane with an infinite, perfectly conducting one may not be valid. Secondly external, unspecified factors due to the measurement system are another probable cause. Cox (1991) compared the measured and NEC-predicted input impedances of a number of HF antennas on aircraft. He attributed differences which existed between predicted and experimental input impedance to dissimilarities in

the modelled and actual feed-points. He also showed how slight differences in the position of the actual point of measurement introduced a predominantly reactive differential between results. Considering the MININEC3 model of the centre-mounted monopole the difference between the predicted and experimental reactance at each frequency corresponded, within  $\pm 5\%$ , to an inductive offset of  $L=2.938\text{nH}$ . Introducing this inductance in series with the MININEC3 predicted results produced the  $G$  and  $B$  plots shown in figures 17 and 18. Clearly this empirically determined reactive shift reduces the frequency offset of the resonance significantly. Also the difference in the magnitude of  $G$  is reduced substantially.

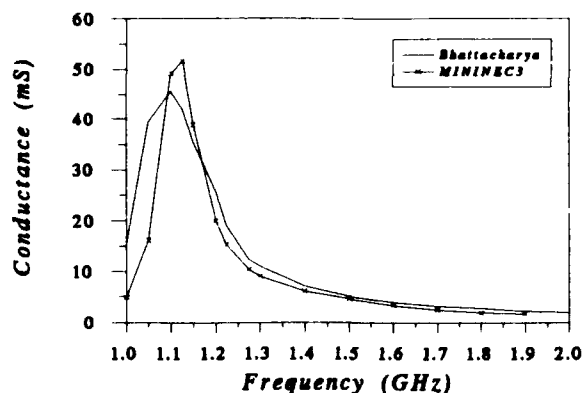


Figure 17. Comparison of experimental and MININEC3-predicted input conductance with an empirically determined inductive offset in the predicted results.

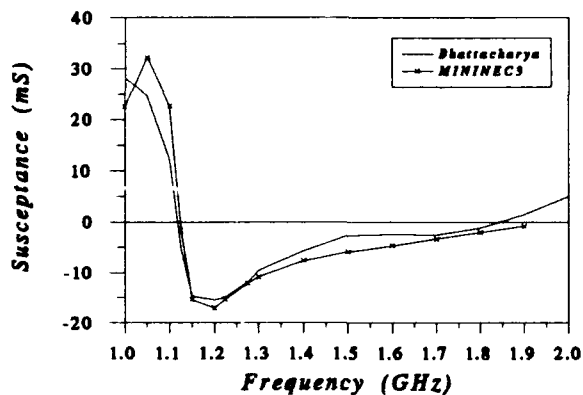


Figure 18. Comparison of experimental and MININEC3-predicted input susceptance with an empirically determined inductive offset in the predicted results.

## 7 Conclusions

This paper has addressed the validation of an expanded MININEC3 method of moments computer code. The antenna structures used in the validation were particularly appropriate for assessing the code's ability to model complex radiating systems accurately. Until its recent conversion from BASIC to FORTRAN it was impossible to use this code for such applications because of the computer CPU time and compiler constraints. The three techniques used in this validation exercise show that MININEC3 may be used with confidence to model electrically large structures. Firstly, excellent agreement was obtained with analytical results for the input impedance of a V-dipole antenna. This was achieved even at the most acute angle considered of  $30^\circ$ , provided adequate segmentation was employed at the junction of the wires. Secondly, good agreement was obtained with the NEC-predicted results for the radiation patterns and input impedances of two wire grid models of typical vehicular type structures. An important finding however was the noticeable frequency shift between the two codes. Although this was most noticeable because of the near-resonant structures that were used in the simulation it must clearly be considered when employing the code. Finally the good agreement with the experimental data for the input impedance of a monopole antenna on a conducting box again demonstrated the usefulness of this modified MININEC3 code.

## 8 Acknowledgement

Acknowledgement is made to the Science and Engineering Research Council for supporting this work.

## 9 References

- Austin, B.A., (1993). "An assessment of MININEC and its use in the teaching of antenna theory", *ACES Journal*, Special issue on Computer Applications in Electromagnetics Education, vol.8, no.1, pp.7-28.
- Beezley, B., (1992). "The MN4 Manual", Brian Beezley, 507 Taylor Street, Vista, Calif., CA 92084, USA.

Bhattacharya, S., Long, S.A. and Wilton, D.R., (1987). "The input impedance of a monopole antenna on a cubical conducting box", IEEE Trans. on Antennas and Propagation, vol.AP-35, pp.756-762.

Chu, W.C., Long, S.A. and Wilton, D.R., (1990). "The radiation pattern of a monopole antenna attached to a conducting box", IEEE Trans. on Antennas and Propagation, vol.38, pp.1907-1912.

Cox, J.W.R., (1991). "Comparison of predicted aircraft wire antenna terminal impedance (using NEC) with measurement in the HF band", 7th International Conference on Antennas and Propagation, IEE Conference Publication no.333, vol.2, pp.717-720.

Harrington, R.F., (1975). "Characteristic modes for antennas and scatterers", Topics in Applied Physics - Numerical and Asymptotic Techniques in Electromagnetics, vol.3, pp.52-87, Springer-Verlag.

Jones, J.E., (1976). "Analysis of a symmetric centred V-dipole antenna", IEEE Trans. on Antennas and Propagation, vol.AP-24, pp.316-322.

Julian, A.J., Logan, J.C. and Rockway, J.W., (1982). "MININEC: A Mini-Numerical Electromagnetics Code", Naval Ocean Systems Center Technical Document 516.

Lewallen, R., (1991). "MININEC: The other edge of the sword", QST, pp.18-22, Feb. issue.

Li, S.T., Logan, J.C., Rockway, J.W. and Tam, D.W.S., (1983). "Microcomputer Tools for Communication Engineering", Artech House.

Logan, J.C. and Rockway, J.W. (1986). "The new MININEC (version 3): A Mini-Numerical Electromagnetics Code", Naval Ocean Systems Center Technical Document 938.

Logan, J.C. (1988). "The MININEC System: Microcomputer Analysis of Wire Antennas", Artech House.

Miller, E.K. (1989a). "MININEC in FORTRAN", IEEE Antennas and Propagation Society Newsletter, vol.31, no.6, pp.28-29.

Miller, E.K. (1989b). "Characterizations, comparison, and validation of electromagnetic modeling software", ACES Journal, Special issue on Electromagnetics Computer Code Validation, pp.8-24.

Murray, K.P. and Austin, B.A., (1993). "Synthesis of radiation patterns for HF mobile communications using characteristic modes", 8th International Conference on Antennas and Propagation, IEE Conference Publication no. 370, pp.904-907

Najm, R.K. (1991). "Simplified 3-D mesh generator", ACES Journal, vol.6, no.2, pp.86-98.

# SOME EXAMPLES OF THE PREDICTION AND VALIDATION OF NEAR-FIELD DEPENDENT AIRCRAFT HF ANTENNA PARAMETERS USING NEC

J. W. R. Cox  
Air Tactical Communications Division  
Space & Communications Department  
Defence Research Agency  
Farnborough  
Hampshire, UK

## ABSTRACT

Examples are presented of the application of a moment-method modelling procedure (using NEC) to calculate the near-field dependent parameters of aircraft HF antennas. The overall aim of the work from which the examples are drawn is to provide a 'recipe'; the application of which will generate predictions of parameters of interest which are both credible and sufficiently accurate for engineering purposes. A feature of the procedure is that no empirically derived information is incorporated. The examples encompass a range of generic aircraft and antenna types: both fixed and rotary wing airframes, and electric (wire) and magnetic (loop and notch) primary radiators. Particular emphasis is placed upon validation of the predictions. This is performed by direct measurement where possible, but where this is not practicable simple, but independent, calculations are performed based upon equivalent circuits. As for the moment-method procedure, these corroborative calculations do not depend upon empirical information.

## INTRODUCTION

At HF (2-30 MHz) airframes are resonant at numerous frequencies throughout the band and modelling procedures must be sufficiently sound to predict such resonances and their effect upon parameters of interest. Thus, near-fields must be calculated accurately for this general reason as well as the more particular one of predicting the actual value of parameters which depend upon the near-field (eg antenna reactance, coupling between antennas etc). Accurate calculation of the near-field requires good solutions for the body surface currents and this implies high sampling densities. There are, however, limitations to the sampling density which can be contemplated. The more obvious practical limitations are:

- (i) time taken to construct mathematical models;
- (ii) run times;
- (iii) factors depending upon machine precision, basis functions, matrix size, and the possible consequences for solution stability.

For those involved in practical calculations pertinent questions therefore are:

- (a) How high does the sampling density need to be for engineering purposes?
- (b) How credible are the results?

The answers to these questions depend of course upon particular circumstances and requirements, but it is hoped that the following examples might be of some use in this regard.

In evolving the methods described here, it was considered important that the modelling procedure would be truly predictive: that is, it should not involve any empirically derived information. For the examples cited below, construction of the mathematical model is performed only with the aid of general arrangement drawings and (when available) photographs or models. The reason for this is that predictions of the likely performance of a proposed antenna system are usually required early in a project cycle prior to the airframe

being available for measurement, or even in existence at all. Indeed if circumstances are otherwise it is sometimes better to generate the required information by other means. Thus, the same modelling procedure was used without *ad hoc* modification for each of the examples, and is as follows.

## **MOMENT-METHOD MODELLING PROCEDURE**

For aircraft-like (that is, non-voluminous) structures in the HF band, the solution stability problems of the magnetic field integral equation (MFIE) preclude its use unless prohibitively high sampling densities are adopted. Use of the electric field integral equation was therefore considered necessary. The aircraft surface is modelled as a wire-mesh and discretized with the aim of producing an approximately square mesh (becoming triangular when required by local topology) with a mesh side of about 0.0025 wavelength (0.3 to 0.4 m) at the bottom of the band (2 MHz). The solution code is a single precision version of NEC3(1) with modifications to facilitate running on a Cray 1 machine. The sampling density was made one match point per mesh side. The radii of the mesh wires are such that the resulting surface area of each wire when notionally 'unwrapped' is the same as that of the surface that it replaces. In effect this represents an attempt to satisfy (approximately) the MFIE, the first term of which represents Ampere's law at a portion of a perfectly conducting closed surface. That is, the magnetic field boundary conditions are approximately satisfied, in addition to the electric field boundary conditions that are imposed at the match points.

## **VALIDATION OF MOMENT-METHOD PREDICTIONS**

A means of quantitatively assessing the validity of moment-method calculations for small-scale problems is to examine the convergence of solution. That is, the discretization is successively refined and the predicted result of some parameter of interest examined after each calculation. The anticipation is that the result at each stage will converge asymptotically to the 'true' value. This is not a practical proposition for large scale problems of the type considered here: the constraints of successively longer periods for model construction and run times preclude this. Thus, experimental and/or independent theoretical means must be sought for validation.

A major problem in assessing the credibility of predictions concerning aircraft HF antennas by experimental means is the frequently encountered impracticability of measuring some parameters of engineering interest. An obvious example is radiation resistance: at the low frequency end of the band this is, in the vast majority of cases, much smaller than the airframe loss resistance and cannot be determined by a measurement made at the antenna terminals. It is clearly not a practical proposition to measure the total radiated power in order to deduce the radiation resistance. In addition, to measure those parameters which could be determined experimentally is often prohibitively expensive because of engineering work which must first be performed upon the aircraft. This is particularly true of smaller aircraft where antenna terminals are often located at positions which are inaccessible when the aircraft is in flight. Thus, independent supporting evidence against which the credibility of predictions can be assessed is usually meagre and so, whatever direct or circumstantial information and physical insight which is available must be exploited: these difficulties have been considered elsewhere (2).

In the examples considered below only in one case was direct (that is, in flight) experimental evidence obtainable for corroboration of near-field parameters. This was because the subject was a medium-size passenger aircraft and the terminals were easily accessible from within the fuselage. In another example, terminal measurements were only practicable for the aircraft located on the ground; this involves additional effects and complications which are not easy to quantify. In another case indirect evidence is sought from radiation patterns: predicted patterns were compared with those derived from measurements made upon a physical scale model, and upon a real aircraft in flight. Although a far-field dependent property, radiation patterns show evidence of airframe resonances and therefore give an indication of the accuracy with which near-fields are calculated.

Where experimental corroboration is not practicable, equivalent circuit models are derived to assess the credibility of the moment-method calculations. The circuit parameters for these models are derived in a logical manner and not simply adjusted to fit the moment method predictions. These circuits, however, involve the application of insight in their construction, considerable simplification to maintain tractability (and therefore the introduction of an element of subjectivity), and can only be convincingly produced for certain antenna types and configurations. It is of course unreasonable to expect good agreement between the moment-method calculations and those derived from an equivalent circuit. In fact the circuit model can really serve to give only an indication as to whether the moment-method calculations are, or are not, credible. One reason for this is that in those cases where the construction of a simple equivalent circuit is possible, the antennas are located near, but not precisely at, the electrical centre of the fuselage. The readily obtainable usable expressions or tabulated values for  $Z$ , the impedance of the dipole representing the fuselage (see below) are, however, derived for centre excitation. Fortuitously for the two examples (2,9) in which equivalent circuits are constructed the antennas are located at approximately 40% along the electrical length of the fuselage. In addition, in both of these cases the resulting circuit component values are such that  $Z$  does not exercise a dominating influence on the final result. Thus, notwithstanding these shortcomings, it is expected that, when applicable, quantitative agreement between the moment-method calculation and the equivalent circuit would be to better than an order of magnitude. By this means therefore, a relatively crude, but independent, piece of theoretical supporting evidence can be produced.

The calculations (that is, moment-method and equivalent circuit) share a common deficiency: neither incorporate any allowance for the effects of non-zero impedance of the mechanical joints which unavoidably exist on real aircraft. As far as HF aircraft antenna performance in general is concerned these extraneous impedances are a perennial source of difficulty. This is because throughout much of the band most aircraft are not electrically large. This inevitably implies that radiation resistance and, in practice radiation efficiency, tends to be relatively small: estimated values of below 0.1% are not uncommon at the bottom of the band. Not only are joint impedances unknown (and, for practical purposes, unknowable) but they vary between nominally identical aircraft and, in the mechanically harsh environment experienced by aircraft, change over time. Thus the assumption of perfect conductivity for calculations is practically inevitable as far as such joints are concerned. Since the extraneous resistance due to joints is usually dominant over much of the band (experience indicates that measured terminal resistance is much greater than that calculated on the assumption of no joints at all), there is little to be gained by assuming other than a perfectly conducting airframe. That is, the calculated terminal resistance is the radiation resistance here.

In one of the airframe examples there are significant portions of the aircraft skin made from non-metallic material. It was noted, however, that large areas of metal existed immediately behind the skin. It was therefore considered realistic, at least at HF, to neglect the skin and treat the surface as perfectly conducting and electrically bonded to the rest of the airframe. It is expected that such bonding of internal metal structures will be arranged to afford protection against lightning strike.

#### **Example 1: Terminal reactance of a medium-size passenger aircraft.**

Three 'long-wire' antennas are fitted to the aircraft: the arrangement is shown in Fig 1. The model comprises 7736 segments and this is the number of unknown currents. This antenna type and configuration presents potential sources of computational difficulty. These are considered more fully elsewhere (3) but briefly they are connected with:

- (1) The very close electrical proximity of the match points in the region of the antenna feed point and near the antenna anchoring point at the tail fin. The match point separation distances are around  $1/3000$  and  $1/1500$  of a wavelength respectively for these two regions.

(2) The problem of distribution of electric charge between wires of disparate radii at junctions. An incidental advantage of adopting a very fine mesh is that the radii of the wires simulating the fuselage become smaller. In addition, the ratio of the radius of the wires simulating the fuselage to that of the antenna wire falls as the mesh is made finer. For the junction treatment (based upon a study of the tapered antenna by Wu and King (Ref 4)) used in NEC, when the wires become electrically very thin the linear charge density at each of the wires at a junction is the same and does not depend strongly on the wire radii. Thus for finer meshes it is anticipated that the solutions become less dependent upon the arrangement made for dealing with junctions. Even with the high sampling densities used here, however, the ratio referred to above is still about 19. The concern is that if unrealistic charge distributions at the base (that is, the terminals) of a wire antenna are computed, these may be expected to have a significant effect upon the calculated terminal impedance.

Comparison between prediction and measurement for the terminal reactance is depicted in Fig 2 with allowance made for the presence of the lightning spark gap and other measured stray reactances present in the real installation (in effect a 'front-end' network to the actual antenna terminals) but which cannot easily be incorporated directly in a moment-method model (see Ref 3). It is seen that the resonances are predicted to within about 10% of the measured values.

**Example 2:** Calculation of maximum mutual coupling between two HF loop antennas mounted upon a helicopter at the bottom of the HF band.

The arrangement is depicted in Fig 3. There are 2250 segments in the model. The maximum mutual coupling is a function of the Y parameters of the configuration (see Ref 2) and its estimation is sensitive to the accuracy with which these parameters are calculated. Validation of the moment-method calculations was attempted by the derivation of an equivalent circuit. Below the first airframe resonance physical considerations suggest that the airframe resembles an electric dipole which is shunt fed by the driven loop antenna. Thus the dominating elementary radiating modes would be expected to be as indicated in Fig 4. In this spectral region, and for this type of antenna, it is expected that the coupling mechanism between the driven antenna and the non-driven antenna is primarily magnetic. That is the driven antenna excites the other principally by transformer action. The equivalent circuit for the arrangement is illustrated in Fig 5. An approximate estimate of the mutual inductance,  $M$ , between the two tail-cone mounted antennas, was made by treating the arrangement as a DC quasi-two-dimensional problem and performing a moment-method calculation. An elementary calculation of the remaining inductances was made using the method of images in conjunction with a procedure which has been termed by Roters (5) as 'estimating the permeances of probable flux paths'. The radiation resistance,  $r_1$ , of the loop is estimated using the well-known expression for an electrically small magnetic dipole with allowance made for the fact that it is mounted on a conducting surface. A more detailed account of the derivation of the equivalent circuit is given in Ref 2. The impedance,  $Z$ , of the dipole representing the fuselage was estimated using the following analytical expression (6).

$$Z = R(k\ell) - j[120(\ln(\ell/a) - 1) \cot(k\ell) - X(k\ell)], \quad (1)$$

where  $\ell$  is the half length of the dipole,  $a$  its radius, and  $k$  the free space wave number of the excitation, the functions  $R(k\ell)$  and  $X(k\ell)$  are tabulated in Ref (6). This expression is not, however, valid at frequencies higher than the first resonance.

Comparison of the maximum mutual coupling calculated by the two methods is shown in Fig 6. The error bars in Fig 6 are a consequence of the uncertainty in assigning a figure to the equivalent radius of the dipole representing the fuselage, and indicate the extreme possible values.

An indicator of solution quality can also be made by examining compliance with reciprocity. This is shown in the following table.

Frequency (MHz)	Current at antenna 2 terminals while short-circuited and antenna 1 driven with excitation	Current at antenna 1 terminals while short-circuited with antenna 2 driven with excitation
	of 1V (A)	of 1V (A)
2	$-0.72 \times 10^{-7} + j 0.15 \times 10^{-3}$	$-0.85 \times 10^{-7} + j 0.17 \times 10^{-3}$
3	$0.59 \times 10^{-6} + j 0.12 \times 10^{-3}$	$0.62 \times 10^{-6} + j 0.13 \times 10^{-3}$
4	$0.57 \times 10^{-5} + j 0.11 \times 10^{-3}$	$0.61 \times 10^{-5} + j 0.12 \times 10^{-3}$
5	$0.42 \times 10^{-4} + j 0.13 \times 10^{-3}$	$0.46 \times 10^{-4} + j 0.14 \times 10^{-3}$
6	$0.51 \times 10^{-4} + j 0.33 \times 10^{-4}$	$0.73 \times 10^{-4} + j 0.42 \times 10^{-4}$

**Table 1 Compliance with reciprocity**

**Example 3:** Determination of antenna impedance for a notch antenna installed on a variable geometry aircraft.

The model is constructed in such a way that it can be reconfigured as a real aircraft of this type might change its geometry. That is, alterations to the model for various positions of the moveable parts correspond exactly to the geometrical changes of the wing or taileron positions alone; there is no remeshing or any other *ad hoc* alternations made to the model (9,10). Figs 7 and 8 indicate the model with the wings in the fully forward and swept back positions. There are 3293 segments in the model. It was considered that the following factors might be a potential source of computational difficulty.

- (i) The moveable surfaces clear the rest of the airframe by electrically very small distances (of the order of 1/1500 of a wavelength at 2 MHz). In addition this necessitates the use of very short segments (representing pins for mechanical pivoting) in the model which are of a similar electrical length to this figure.
- (ii) The area of the notch antenna is of the order of the mesh size. In the context of running NEC on 32-bit machines, difficulties have been indicated for problems involving small loops (7). Although the work reported here was performed with single precision on 64-bit machines, it is considered that calculations should be regarded with caution particularly in view of the large and complex nature of the structures.

Validation of predictions of the terminal impedance made for the aircraft in flight was attempted by two methods. The first was to derive an equivalent circuit in a manner similar to that indicated for the previous example. The second was by measurement of terminal impedance with the aircraft on the ground.

The equivalent circuit is show in Fig 9. As indicated above, the use of equation (1) to calculate  $Z$  is limited to frequencies below the first airframe resonance. In addition to using equation (1),  $Z$  was also estimated assuming that the effect of dipole thickness on the antenna terminal impedance is not too great. This is, of course, a rather gross approximation, but it does permit values of  $Z$  to be obtained beyond the first airframe resonance using tabulated results using Wu's theory (8).

The ground measurements were performed using a vector impedance meter (VIM). Such measurements are not entirely straightforward because the effects of the cable which is required to connect the VIM to the antenna terminals must be removed from the data in order

to extract the terminal impedance. This aspect is reported in more detail, along with checks of the experimental method, in Ref 10.

Comparison between the NEC calculation, the equivalent circuit model, and the ground measurements are depicted in Fig 10 for the terminal reactance. As indicated above it is not possible to extract the radiation resistance from the measured terminal resistance; hence for the former parameter, the moment-method predictions can only be compared with those of the equivalent circuit (see Fig 11). Elementary considerations suggest that the reactance should increase monotonically throughout the band and remain positive. This is observed for the calculations and measurements. It is seen that the values derived by measurement are about 36% below those of the NEC calculation over that part of the band which is approximately linear. This figure is comparable with a similar difference (26%) between measured and theoretical values (from an analytical expression) performed as a check of the measurement procedure and made on a circular loop having an area comparable to that of the notch (10).

It is expected from simple physical considerations that the longitudinal airframe resonances will occur around those frequencies at which the electrical length of the airframe is an integer multiple of half the radiation wavelength. They are approximately 7.6, 15.2 and 22.8 MHz for this example. The form of the equivalent circuit (see Fig 9) and the fact that the radiation resistance of the dipole is always significantly greater than that of the notch ( $r_1$ ), suggests that such effects are expected to be noticeable in the NEC calculations even though resonance is a phenomenon associated with the near-field whereas radiation resistance is a far-field property. It is seen in Fig 11 that the results of the NEC calculation show disturbances which occur close to the above values of resonant frequency. Such effects are not observed for the reactance (Fig 10) because the component values are such that the shunting effect of  $Z$  is not such as to be large at any frequency in the band; not even at a series resonance. The pronounced oscillations seen in Fig 11 for the equivalent circuit model are a result of the thin wire approximation for the fuselage. Such oscillations would not be expected to be so marked in the case of a large diameter dipole such as that forming the real fuselage and it is seen in Fig 11 that they are only just perceptible on the curve for the NEC calculation. Interestingly, the two methods display a reasonable agreement at the series resonances (7.6 and 22 MHz). At such frequencies the representation of the fuselage by a thin wire would not be expected to exert a great influence to the radiation resistance estimated using the equivalent circuit.

**Example 4:** Inference of first longitudinal airframe resonant frequency from radiation patterns.

This helicopter was fitted with a loop antenna and is as depicted in Fig 12. There are 2682 segments in the model. The example is included to indicate that, as far as validation is concerned, radiation patterns can be used to indicate quality of solution even though radiation patterns depend upon the far-field. This is because, at HF, airframes are generally resonant at numerous frequencies throughout the band. For this example measurements of radiation patterns were made both using a scale physical model and with a real aircraft in flight. Details of this study along with a set of radiation patterns throughout the HF band is recorded elsewhere (11). The first airframe resonance is usually apparent in azimuthal radiation patterns for horizontal polarisation. It is characterised by a deep null in the general nose and tail directions. The nulls do not lie exactly on the nose-tail axis unless the antenna itself is also located symmetrically about this line. Greater complexity of the patterns at higher frequency resonances renders such unambiguous interpretation less likely than in the case of the first airframe resonance. This is due to the corresponding increase in the number of possible radiation modes which will, in general, be present. For the antenna orientation adopted here, the length of the probable RF current path indicates that the first longitudinal airframe resonance should be in the region of 6 MHz. Figs 13 -15 indicate a succession of such patterns as the frequency is increased through the first airframe resonance. These figures show the anticipated resonance occurs around 5.6 MHz. In passing it is noted that the patterns display the fact that the antenna is located on the left side of the aircraft. This is

seen from the slightly higher levels of radiation on this side and if no experimental evidence was available would provide a simple but nevertheless useful additional indicator of the credibility of the calculations.

Examination of Figs 13-15 indicate in addition an aspect which is of some practical importance; namely that there is a level of precision in calculations beyond which there is only limited practical benefit in proceeding at least in the case of radiation pattern prediction at HF. This is due to the difficulty of making measurements reliably and repeatably with real aircraft and is in part due to the stochastic nature of the propagation conditions in this spectral region. Thus, there is some uncertainty as to what the 'correct answer' actually is.

## CONCLUSIONS

For the examples presented, the moment-method calculations seem generally consistent with such attempts at validation as could be made, and it is considered that they enhance the degree of confidence which can be placed in the prediction of near-field dependent parameters for large scale problems involving aircraft. For the aircraft HF case at least, the difficulty of quantifying the electrical properties of joints present on the airframe, and the variability of the propagation conditions, limit the precision which is, in practice, useful when calculations are required for the estimation of certain system parameters such as link budgets and for the prediction of radiation patterns.

## REFERENCES

- 1 Burke, G.J. and Poggio, A.J., "Numerical Electromagnetic Code – Method of Moments", NOSC Technical Document 116, Vols.1 and 2, January 1981
- 2 Cox, J.W.R., 1993, "Corroboration of a moment-method calculation of the maximum mutual coupling between two HF antennas mounted upon a helicopter", IEE Proc. Part H, Vol.40, No.2, April 1993, pp 113-120
- 3 Cox, J.W.R., "Comparison of predicted aircraft wire antenna terminal impedance (using NEC) with measurement in the HF band", Proc. 7th Int. IEE Conf. on Antennas and Propagation, York, UK, 1991, Conf. Publication No.333, pp 717-720,
- 4 Wu, T.T. and King, R.W.P., "The tapered antenna and its application to the Junction problem for thin wires", IEEE Trans. Antennas and Propagation, AP 24, pp 42-45, January 1976
- 5 Roters, H.C., "Electromagnetic devices", Wiley, New York, 1944, Chapter 5.
- 6 Johnson R. and Jasik, H., "Antenna Engineering Handbook", McGraw-Hill, 1984, pp 4.4-4.6
- 7 Burke, G.J., "Recent advances to NEC: applications and validation", AGARD Lecture Series No.165 – "Modern antenna design using computers and measurement: Application to problems of military interest", pp 3-1 to 3-25
- 8 King, R.W.P. and Harrison, C.W., "Antennas and waves: a modern approach", Table A.4.2, pp 753-757, The MIT Press, 1969
- 9 Cox, J.W.R., "Calculation of HF notch antenna terminal impedance for variable geometry aircraft", Proc. 8th Int. IEE Conf. on Antennas and Propagation, Edinburgh, UK, 1993, Conference Publication No.370,, pp 912-916
- 10 Cox, J.W.R., "Problems concerning the validation of moment-method models of small aircraft in the HF band", IEE Colloquium on validation and application of design tools for antennas, IEE London, June 1993, Digest No.1993/147, pp 6.1-6.8
- 11 Cox, J.W.R. and Vongas, G., 1991, "Calculated and measured radiation characteristics of an HF loop antenna mounted upon a helicopter", Proc. 5th Int. Conf. on HF Radio Systems and Techniques, Edinburgh, UK, 1991, Conf. Publication No.339, pp 73-78,

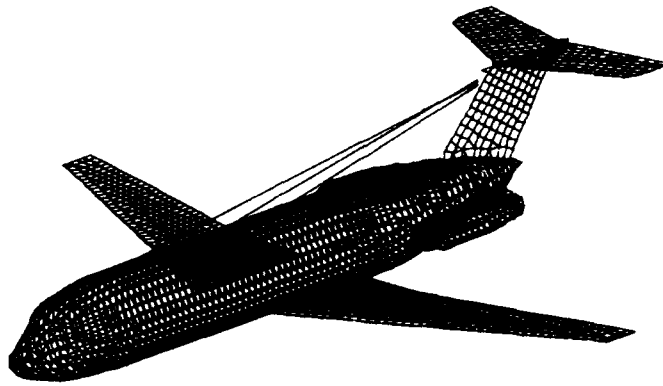
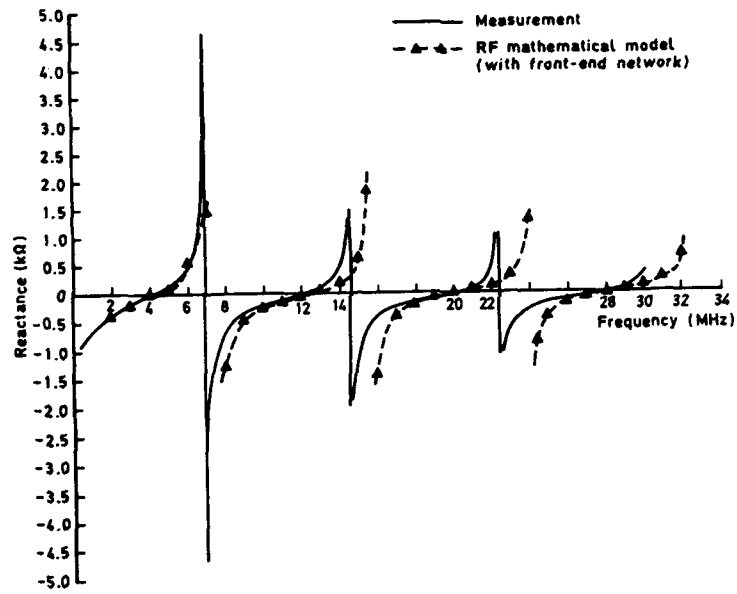


Fig 1



Terminal reactance versus frequency for RF mathematical model with front-end network compared with measurement

Fig 2

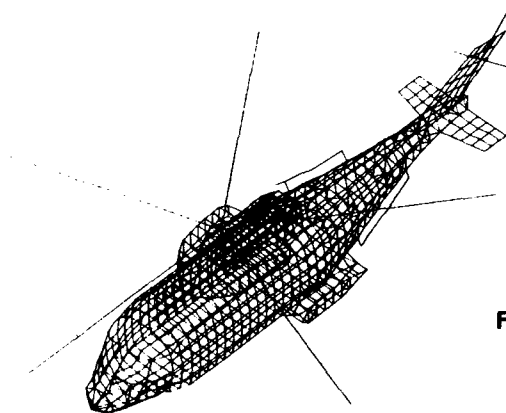
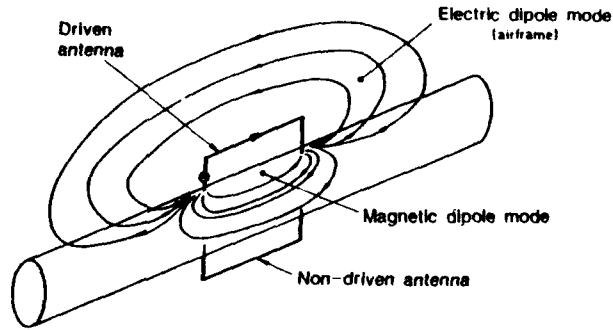
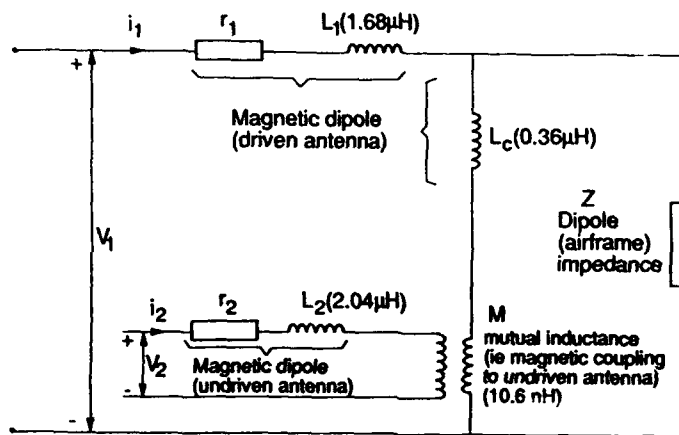


Fig 3



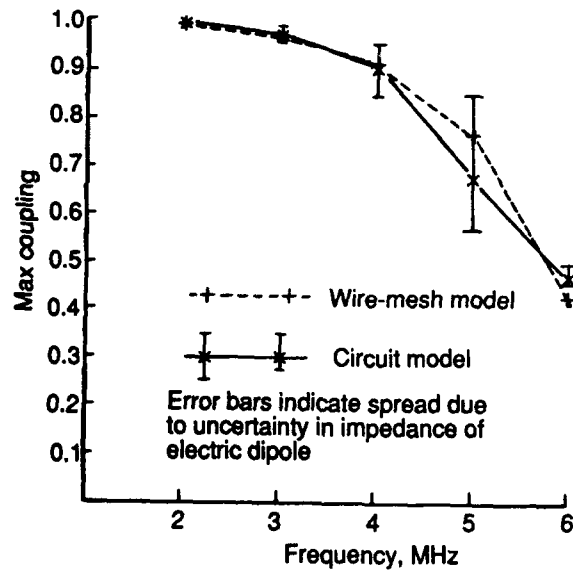
Elementary radiating modes at frequencies below the first longitudinal airframe resonance

Fig 4



Approximate equivalent circuit for elementary radiating modes and coupling to undriven antenna

Fig 5



Variation of maximum coupling between antennas versus frequency for wire-mesh and circuit models

Fig 6

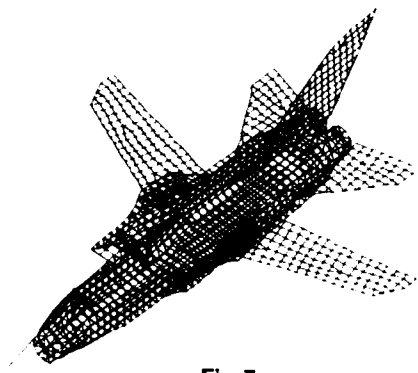


Fig 7

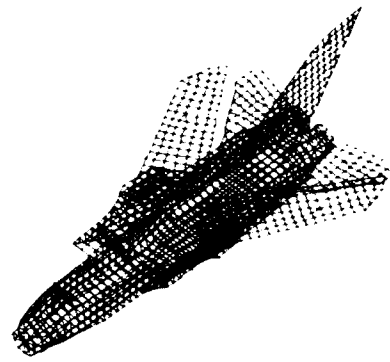
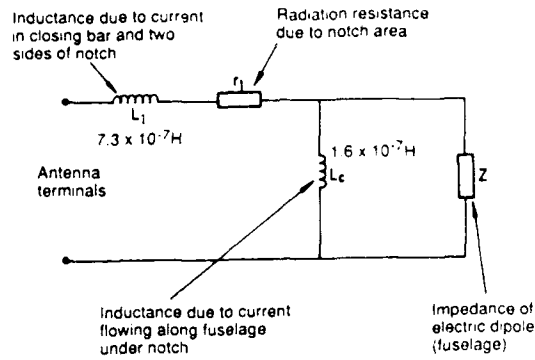
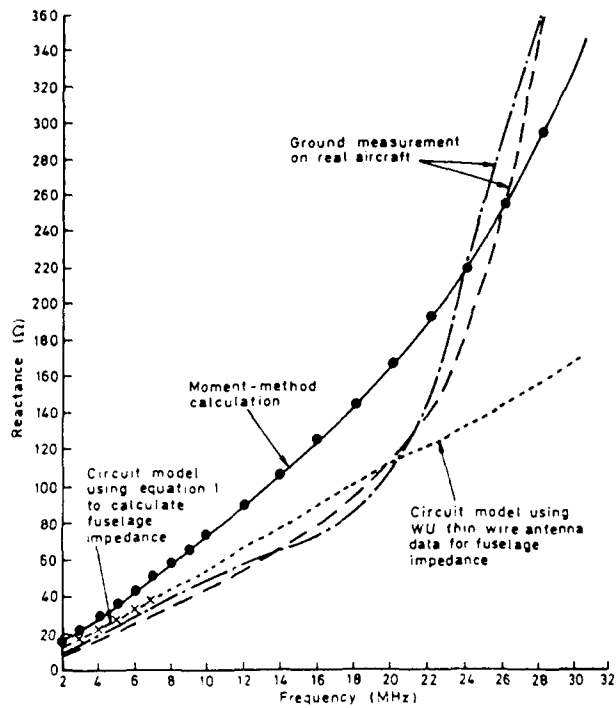


Fig 8



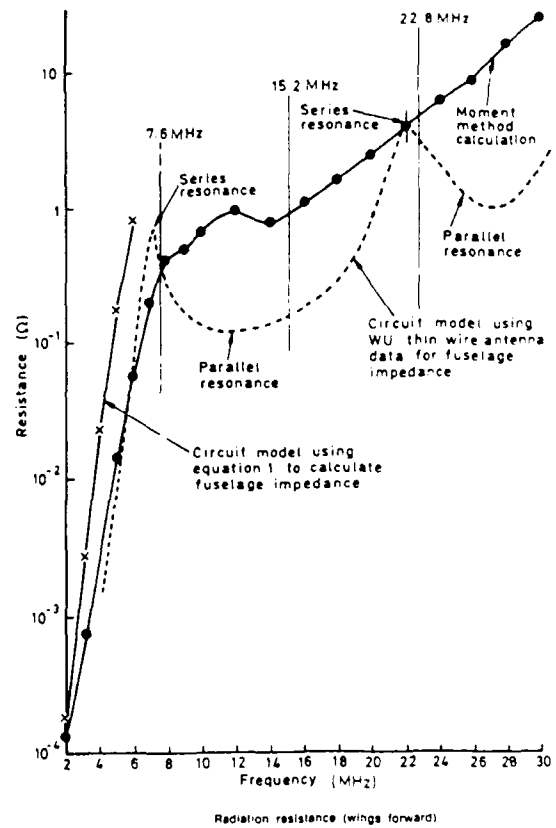
Approximate equivalent circuit of notch antenna and fuselage

Fig 9



Terminal reactance - frequency (wings forward)

Fig 10



Radiation resistance (wings forward)

Fig 11

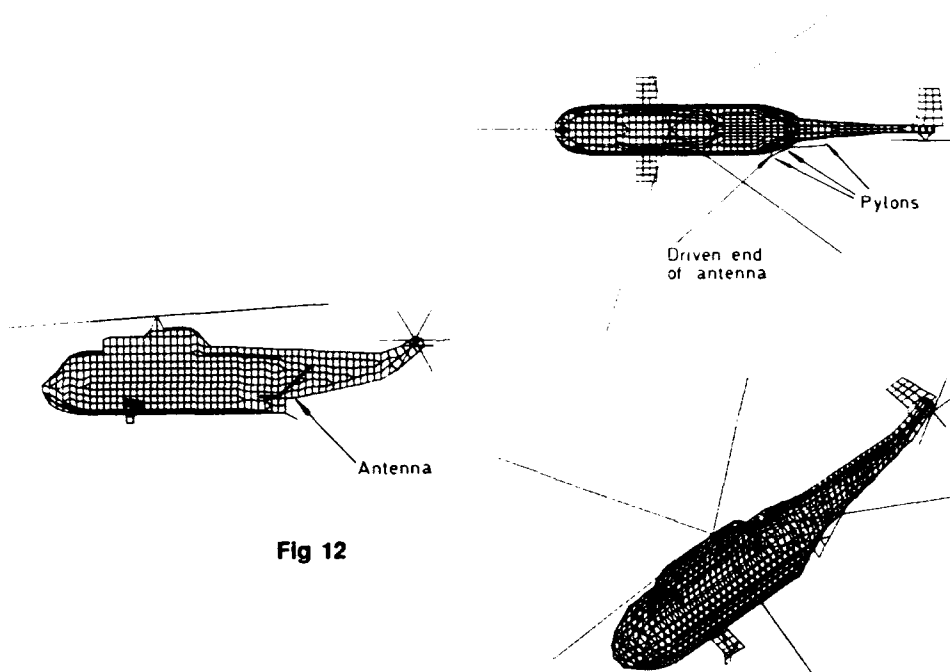


Fig 12

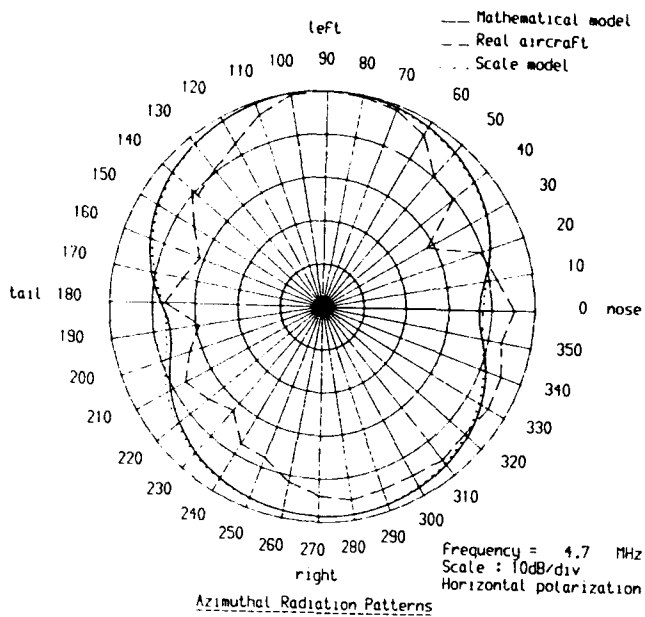


Fig 13

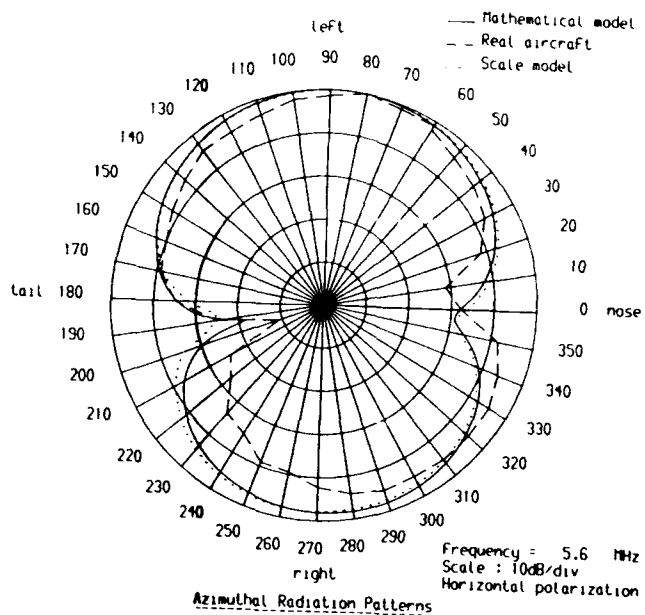


Fig 14

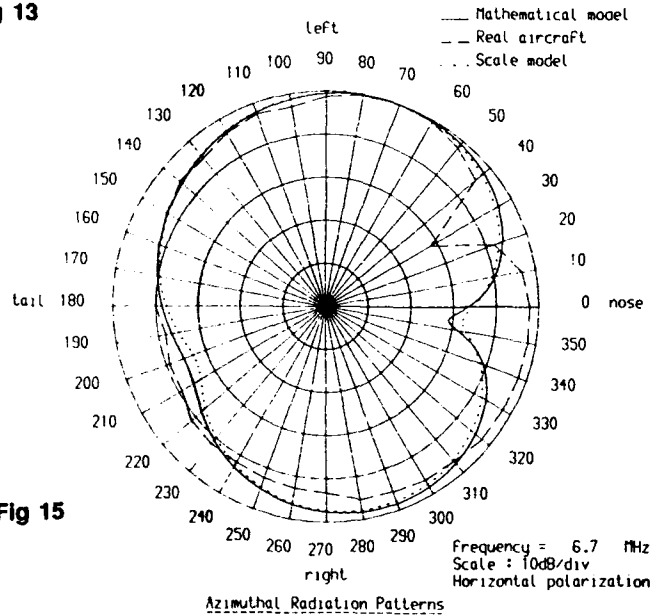


Fig 15

# Use of a stealth boundary with finite difference frequency domain simulations of simple antenna problems

R.B. Thompson, F.S. Chute, and F.E. Vermeulen

Department of Electrical Engineering  
University of Alberta  
Edmonton, Alberta, Canada T6G 2G7  
(403) 492-3332

## Abstract

A direct method for the numerical solution of Maxwell's equations in the frequency domain (sinusoidal steady state), for radiation problems of cylindrical symmetry, is incorporated into a finite difference program called HERZ, coded in FORTRAN. The termination of the fields on the outer boundary of the problem domain is accomplished via an absorptive layer, labelled a *stealth layer*, which attenuates the incident fields to insignificant amounts in a small computing space, without causing significant reflections that would disturb the near field solutions. No radiation boundary condition is specified on the problem domain, rather, the transmission of the fields to the stealth layer is optimized by specifying its electrical properties. To validate HERZ as a useful electromagnetic modeller for thin wire antennas, driving point admittances and surface current distributions for several configurations were compared to both theoretical and measured values, with good agreement.

## Introduction

In the numerical modeling of radiation problems, particularly those of isolated thin wire antennas, specific radiation boundary conditions allow finite difference or finite element techniques to be applied (Ramahi *et al.* 1991). The implementation of non-local boundary conditions such as boundary integral formulations or moment method techniques is useful for infinite homogeneous configurations but bounded methods are typically incorporated in conjunction with these techniques if inhomogeneities exist, such as in the case of a dielectrically coated antenna (McDonald and Wexler 1972, Morgan *et al.* 1984, Yuan *et al.* 1990). To avoid the complication of coupling a bounded problem to an unbounded problem, specific radiation boundary conditions are formulated in conjunction with finite element techniques (Sumbar *et al.* 1990).

While finite element techniques allow for very flexible grid density and are straightforward in their treatment of inhomogeneities, the complex nodal grids which must be generated lack the physical transparency and

simplicity of a finite difference grid system. In this paper an absorbing layer adjacent to the problem space boundary is used in place of an explicit radiation boundary condition. Rather than specifying a radiation condition to terminate the fields of the antenna, shown in Fig. 1, on the problem domain, the transmission of the fields from the problem domain to a lossy layer enveloping the problem domain is modelled, as illustrated in Fig. 2. The problem domain's boundaries are then in an interior grid location, as the grid encompasses both the problem domain and it's surrounding lossy layer, which will now be referred to as the *stealth layer*. The near-field problem can then be solved at the expense of the far-field solutions, which will be attenuated in the stealth layer, without disturbing the field distributions within the initial problem domain. A related technique for truncating the solution domain in finite element scattering problems has been discussed in the literature (Jin *et al.* 1991, 1992).

This methodology is incorporated into a FORTRAN program, called HERZ (H field E field, R - Z geometry), which is executed on a Macintosh II personal computer. The finite difference implementation of Maxwell's equations and the use of the absorptive stealth layer are described in the following sections. Several antenna configurations are modelled with HERZ to validate this approach, comparing field related values such as driving point admittances and surface current distributions to published theoretical and measured results.

## Finite difference implementation of Maxwell's equations

Cylindrically symmetric metallic antennas operating in cylindrically symmetric inhomogeneous materials, with geometries as shown in Fig. 1, will have simplified electric and magnetic field orientations when the electrical properties of these materials are isotropic. The electric fields will have radial and axial components ( $r, z$ ), and the magnetic fields only an azimuthal component ( $\theta$ ).

The general time-harmonic solutions will be of the form

$$\mathbf{E} = E_r(r,z)\hat{\mathbf{a}}_r + E_z(r,z)\hat{\mathbf{a}}_z \quad (1)$$

$$\mathbf{H} = H_\phi(r,z)\hat{\mathbf{a}}_\phi \quad (2)$$

Assuming an  $e^{j\omega t}$  time dependence, the integral form of Maxwell's equations can be expressed as

$$\oint \mathbf{E} \cdot d\mathbf{l} = -j\omega\mu \iint \mathbf{H} \cdot d\mathbf{S} \quad (3)$$

$$\text{and} \quad \oint \mathbf{H} \cdot d\mathbf{l} = (\sigma + j\omega\epsilon) \iint \mathbf{E} \cdot d\mathbf{S} \quad (4)$$

The solution technique adopted uses these integral equations to form surfaces and contours accommodated by the finite difference grid structure (Albani and Bernardi 1974), providing an algorithm to compute the azimuthal magnetic field component,  $H_\phi$ , at the center of every gridblock. (3) was discretized to express the  $H_\phi$  field in a gridblock center in terms of the four  $E$  field values which surround it, as is displayed in Fig. 3, the finite difference grid implementation in HERZ. The resulting linear equation is of the form

$$a_{i,j} E_{zi,j} + b_{i,j} E_{ri,j+1} + c_{i,j} E_{zi+1,j} + d_{i,j} E_{ri,j} = e_{i,j} H_\phi'_{i,j} \quad (5)$$

where the coefficients  $a_{i,j}$  to  $e_{i,j}$  depend on the grid dimensions  $\Delta r_i$  and  $\Delta z_j$  (Nachai *et al.* 1992). The gridblocks have been assumed to be small enough that the electric field components are constant along each line segment of the gridblock  $i,j$  and the magnetic field is uniform over its cross section. In this equation

$$r H_\phi = H_\phi'$$

where  $r$  is the radial distance to the center of the gridblock where  $H_\phi$  is being calculated.

By applying (4) to appropriate surfaces and contours, the various electric field components in (5) can be written in terms of the magnetic fields at the centers of the surrounding gridblocks. For example, with reference to Fig. 3,  $E_{zi,j}$  can be expressed in terms of  $H_\phi'_{i-1,j}$  and  $H_\phi'_{i,j}$  by applying (4) to the contour consisting of two concentric circular paths of radii  $r_{i-1}$  and  $r_i$  to compute the total axial current (conduction and displacement) through the enclosed surface. The equation that results for the magnetic field is

$$A_{i,j} H_\phi'_{i,j} + B_{i,j} H_\phi'_{i-1,j} + C_{i,j} H_\phi'_{i+1,j} + D_{i,j} H_\phi'_{i,j-1} + E_{i,j} H_\phi'_{i,j+1} = 0 \quad (6)$$

where the coefficients  $A_{i,j}$  to  $E_{i,j}$  are given in terms of the frequency  $\omega$ , the electrical properties  $\sigma$ ,  $\epsilon$  and  $\mu$  and the radial locations and dimensions of the pertinent gridblocks (Nachai *et al.* 1992). The discretizations of (3) and (4) are particularly transparent and easy to implement because all electric and magnetic field components are tangential to material interfaces and the difficulties that can be encountered in handling inhomogeneous problem domains in three dimensions do not arise.

Each of the  $N$  gridblocks, referred to by indices  $i,j$ , will have an associated equation of the form of (6), providing the  $N$  unknown  $H$  fields with  $N$  linearly independent equations, resulting in a determined system. To completely specify the problem, conditions must be provided on the problem boundary. Excitation by electric fields on the grid's outer domain, the Neumann boundary condition, requires an adjustment of the LHS of (6), as one of the terms  $E_r$  or  $E_z$  in (5) is then predetermined. The excitation electric field appears on the RHS of (6).

Electric field excitation is specified exclusively on the perimeter of the problem domain, where it may, for instance, be set to zero to signify the presence of a perfectly conducting boundary. At all other locations in the problem domain the electric field excitation is zero. Magnetic field excitation may be applied at the center of any gridblock by specifying a value of  $H_\phi$ .

The set of  $N$  equations for  $H_\phi'$  represents a banded symmetric system which can be stored in the computer in a compressed coefficient matrix,  $K$ . The unknown values of  $H_\phi'$ , and hence  $H_\phi$ , are obtained by Gaussian elimination. The solution  $H_\phi$  is then used in (4) to obtain the electric field values on the perimeter of every gridblock, and simple averaging is used to obtain the values of the electric fields at the gridblock centers.

Typical grids consist of approximately 75 x 75 gridblocks, with no more than 15 gridblocks per wavelength. Blocks are chosen with a consideration of the radiation wavelength, the radius and length of the antenna being modeled, as well as the gap size used to excite the antenna.

#### Incorporation of stealth boundary conditions

As was stated earlier, no radiation boundary condition was directly applied at the problem domain's outer surface. Rather, optimal transmission of the fields into the stealth layer was sought. The tangential electric field at the outer boundary of the stealth layer was set to zero, which is equivalent to bounding the stealth layer with a perfect conductor.

The transmission of radiation normally incident upon a boundary is determined by the wave impedances on both sides of the material interface, with matched wave impedances providing perfect transmission. To achieve normal incidence of the radiated wave at the stealth layer, the surface of the stealth layer should be a sphere centered at the antenna, with a radius many times the wavelength. In practice it was found sufficient to approximate the surface of the sphere by a cylindrical boundary, as shown in Fig. 2, and rely upon multiple reflections from the stealth layer to minimize the disturbances to the near fields. The distance from the center of the antenna to the stealth layer's surface was set at three wavelengths. A chamfer in the stealth layer, as indicated by the dotted line in the upper right hand corner of Fig. 2, was initially used to better approximate a spherical boundary. Only a small improvement was obtained, however, at the expense of a relatively complex design. The chamfer, therefore, was not used in any of the cases considered in this paper.

The wave impedance and propagation constant for a plane wave propagating in a general lossy medium are

$$\eta = \sqrt{\frac{\mu}{\epsilon}} = \sqrt{\frac{j\omega(\mu' - j\mu'')}{(\sigma + j\omega\epsilon)}} \quad (7)$$

$$\text{and } \gamma = \alpha + j\beta = \sqrt{j\omega(\mu' - j\mu'')(\sigma + j\omega\epsilon)} \quad (8)$$

where  $\eta_{\text{stealth}} = \eta_{\text{problem domain}}$  would maximize transmission for normal incidence at large distances from the antenna structure, and  $\alpha_{\text{stealth}}$  would define the attenuation rate in the absorbing layer. While it can be seen from Fig. 2 that waves will not impinge upon the stealth layer normal to its surface, it has been found that choosing the electrical properties to satisfy the foregoing provides satisfactory results, as exemplified by the case studies to follow. Given an excitation frequency,  $\mu'$ ,  $\mu''$ ,  $\sigma$ , and  $\epsilon$  in the fictitious stealth layer were chosen to obtain an impedance match, and to diminish the field strength to insignificant values in the allotted stealth layer thickness. When choosing the parameters  $\mu'$ ,  $\mu''$ ,  $\sigma$ , and  $\epsilon$  for the stealth layer, a great amount of flexibility was found to exist, even when specifying both the stealth layer wave impedance and attenuation per wavelength. The stealth layer was typically one wavelength (15 gridblocks) thick, measured in the stealth material. For this thickness, typically substantially less than 1% of the normally incident power was reflected from the surface of the stealth layer, and the absorbed radiation was reduced to approximately 1% of its original value, before impinging upon the perfectly conducting boundary which is assumed to bound the computational grid. Thinner stealth layers with increased attenuation per

wavelength, or thicker stealth layers with less attenuation generally also provide satisfactory results. Our own choice was made for convenience and with a view to not significantly increase computational times. For example, in the case of the monopole in free space  $\omega = 100$  MHz,  $\mu' = 1.0\mu_0$ ,  $\mu'' = 0.7\mu_0$ ,  $\sigma = 0.00389$  S/m, and  $\epsilon = 1.0\epsilon_0$  in the stealth layer. This matched the free space wave impedance and provided 98.8% attenuation per wavelength.

### Simulation results

This section presents some typical results of the thin wire antenna configurations modeled. Simulation results are compared to both experimental and theoretical data. HERZ was implemented in FORTRAN using Macintosh Programmer's Workshop (MPW) version 3.0 on a Macintosh II personal computer, with an RP88 coprocessor to increase performance, which resulted in execution times of approximately six minutes.

Three representative antenna configurations were considered: (1) A bare coaxially fed monopole over an infinite conducting plane operating in a lossless medium, (2) a bare center fed dipole operating in a lossy medium, and (3) a dielectrically coated monopole operating in air. Fig. 4 displays the general configurations modelled in each case.

To validate HERZ, the surface current distribution and input admittance for each antenna configuration were compared to available theoretical or measured values. The boundary condition for the tangential magnetic field at the antenna's surface,  $\mathbf{n} \times \mathbf{H} = \mathbf{J}_s$ , was used to determine the surface current  $I$ , directly from  $H_\phi = I/2\pi r$ . The driving point admittance was obtained by dividing the current on the antenna nearest the driving point by the voltage across the gap at that point, calculated from  $\int \mathbf{E} \cdot d\mathbf{l}$ , where  $d\mathbf{l}$  is perpendicular or parallel to the antenna axis, depending on whether the gap is coaxial or that of a center fed dipole. Fig. 4 displays the driving points for all configurations. HERZ calculates the fields at the gridblock centers, so to find  $H_\phi$  on the antenna's surface, a third-order polynomial was fitted to the field values in the neighboring blocks, extrapolating radially to the surface. The gridblock configuration in the excitation gaps will be given for each case.

Fig. 5(a) displays the driving point admittance versus antenna length for the monopole in free space. This thin antenna, with  $a/\lambda = 0.0064$ , and  $b/a = 1.189$ , was excited at 100 MHz. The theoretical curve, as determined by King (1971, p. 11), was matched very well by the output from HERZ, for all antenna lengths. Fig. 5(b) displays the normalized current distribution along a similar monopole in free space, with  $h/\lambda = 0.5$

and  $a/\lambda = 0.0254$ , also excited at 100 MHz. Here, HERZ agrees closely with the transmission line model by King (1971, p. 18). For both cases, the excitation was specified at the ground plane level, assuming a  $1/r$  coaxial voltage distribution across the gap, with only 2 gridblocks across this region. The formulas used in King's theory (1971, p. 9) rest on the assumption that a TEM mode exists at the junction of the coaxial feed and the antenna, justifying the  $1/r$  excitation used in HERZ.

Fig. 6(a) shows the excellent agreement between HERZ's calculated admittance and Scott's measured values and King's theoretical results (1981 p. 170) for a dipole radiating in a lossy medium, with a conductivity of  $5.35 \times 10^{-3}$  S/m, and relative dielectric constant of 6.0. For this trial,  $a/\lambda = 0.00265$ , and  $a/b = 0.07$ , at 114 MHz, where  $\lambda$ ,  $\alpha$ , and  $\beta$  are the wavelength, attenuation constant, and propagation constant of the radiation in the lossy medium (Ramo and Whinnery 1967). Examination of Fig. 6(a) shows that HERZ provides closer agreement with the measured values than do King's theoretical results.

King assumed a delta function generator in an infinitesimal gap in formulating his theoretical curve, but unfortunately, Scott's gap size is not specified in the forementioned reference. HERZ utilized a gap size (1.0 mm) of the same order as the antenna radius (2.65 mm) for this trial, but several other trials indicate that the gap size is not critical, with results remaining nearly constant for all gap sizes less than the antenna radius. The critical factor in modeling the gap was the number of blocks employed, with four radial and three axial blocks sufficiently representing this sensitive region for the trial represented, as the good results indicated. As the number of gridblocks in this region was decreased, the admittance results deviated from Scott's measured values, but increasing the number of blocks increased the simulation run time, while having insignificant effects on the simulation results. The normalized current distribution for this antenna configuration was also determined using HERZ, for an antenna of length  $\beta h = 0.315$ . Fig. 6(b) shows the simulation results versus both Scott's measured values and King's theoretical distribution (1981, p. 165).

Experimental results for dielectrically coated antennas by Lamensdorf (1967) were used to verify HERZ in this capacity. Figures 7(a) and 7(b) display Lamensdorf's measured input admittance for a monopole operating in free space at 600 MHz with  $2a = 6.35$  mm,  $2b = 19.05$  mm, and  $D/2a = 3.74$ , for two different dielectric coatings,  $\epsilon_r = 9.0$  and  $\epsilon_r = 15.0$ . Both dielectric coatings were modeled with conductivities of  $0.001$  S/m. This value was chosen to best represent the non-specific value of  $\sigma \leq 0.001$  S/m provided in the Lamensdorf publication. HERZ's

simulation results replicate the shape of Lamensdorf's measured distribution, providing a reasonable overall match in both cases. Unlike the monopole previously modeled, in which a TEM coaxial field distribution across the gap could be assumed, the coaxial line was modeled to best represent the actual fields across the gap at the ground plane level. The number of radial gridblocks used to model the coaxial line feeding the antenna depended on the ratio of the outer to inner coaxial radii,  $b/a$ . The previous monopole modeled had a  $b/a$  value of 1.189 so two grid blocks to represent the gap were sufficient. In the present example,  $b/a = 3.0$ , and trial and error indicated that six radial gridblocks were optimal in modeling the gap. TEM excitation was applied at one eighth of a wavelength of the coaxial line below the ground plane. This length of line was modeled in ten axial gridblocks. HERZ's current distribution on a similar antenna configuration with  $2a = 6.35$  mm,  $2b = 19.05$  mm and  $\sigma = 0.0032$  S/m, but with  $D/2a = 8$ , is displayed in Fig. 7(c) along with Lamensdorf's measured values. The agreement is reasonable, but not as good as in previous cases. This may reflect the difficulty of modeling a larger coaxial gap than previously considered, or the inhomogeneity associated with the long dielectric coating.

Additional antenna configurations, radiating into materials ranging from air to highly lossy, were tested along with those cases considered in this paper. Similar agreement with theoretical and measured data was obtained. This agreement was generally comparable to or better than that achieved earlier with a finite element program utilizing radiation boundary conditions (Sumbar *et al.* 1990).

## Conclusions

The use of stealth boundary conditions in the finite difference simulation of simple antenna problems appears to be very effective. The method is physically very transparent and the simplicity of the finite difference grid structure permits easy realization of the antenna configurations. The methodology was tested for a monopole in free space, a dipole in a lossy medium, and a dielectrically coated monopole in free space. In all cases, results agreed well with published theoretical and experimentally measured values.

## Acknowledgments

The authors wish to acknowledge the financial support of the Natural Sciences and Engineering Research Council of Canada and the help provided by a Faculty of Engineering Dean's Research Award to R.B. Thompson.

## References

Albani, M., and Bernardi, P., "A numerical method based on the discretization of Maxwell's equations in integral form," *IEEE Trans. Microwave Theory Tech.*, MTT-22, 446 (1974).

Jin, J.M., Volakis, J.L., Liepa, V.V., "An engineer's approach for terminating finite element meshes in scattering analysis," 1991 IEEE AP-S Symposium Digest, vol. 2, pp. 1216-1219, June 1991.

Jin, J.M., Volakis, J.L., Liepa, V.V., "Fictitious absorber for truncating finite element meshes in scattering," *IEE Proc. H*, vol. 139, pp. 472-476, Oct. 1992.

King, R.W.P., *Tables of Antenna Characteristics*, (IFI/Plenum, New York, 1971).

King, R.W.P., *Antennas in Matter: Fundamentals, Theory, and Applications*, (MIT Press, Cambridge, 1981).

Lamensdorf, D., "An experimental investigation of dielectric coated antennas," *IEEE Trans. Antennas Propagat.*, AP-15, 767 (1967).

McDonald, B.H., and Wexler, A., "Finite-element solution of unbounded field problems," *IEEE trans. Microwave Theory Tech.*, MTT-20, 841 (1972).

Morgan, M.A., Chen, C.H., Hill, S.C., and Barber P.W., "Finite element-boundary integral formulation for electromagnetic scattering," *Wave Motion* 6, 91 (1984).

Nachai, M., Chute, F.S., and Vermeulen, F.E., "On the radio-frequency heating of moist, porous earth-type materials by guided wave propagation along embedded parallel conductors," *J. Microwave Power and Electromagnetic Energy*, 27, No. 3, 143 (1992).

Ramahi, O.M., Khebir, A., and Mittra, R., "Numerically derived absorbing boundary conditions for the solution of open region scattering problems," *IEEE Trans. Antennas Propagat.*, AP-39, 350 (1991).

Ramo, S., Whinnery, J.R., and Van Duzer, T., *Fields and Waves in Communication Electronics*, 2nd Ed., (John Wiley & Sons, New York, 1984).

Sumbar, E., Chute, F.S., and Vermeulen, F.E., "A 2-D finite element model for wave propagation into arbitrary inhomogeneous materials," *ACES Journal*, 27 (1990).

Yuan, X., Lynch, D.R., and Strohbehn, J.W., "Coupling of finite element and moment methods for electromagnetic scattering from inhomogeneous objects," *IEEE Trans. Antennas Propagat.*, AP-38, 386 (1990).

**Figure 1**

The general antenna configuration and coordinate system used in HERZ.

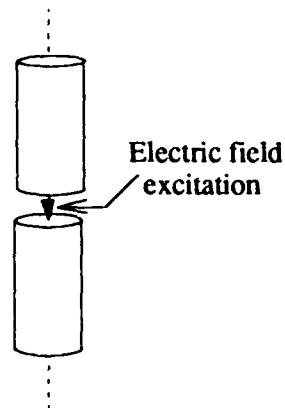
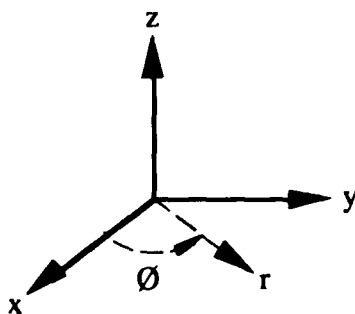


**Figure 2**

The outline of the finite difference grid system used to model the problem domain and stealth layer. All boundary conditions are specified on the outermost boundary, as indicated.

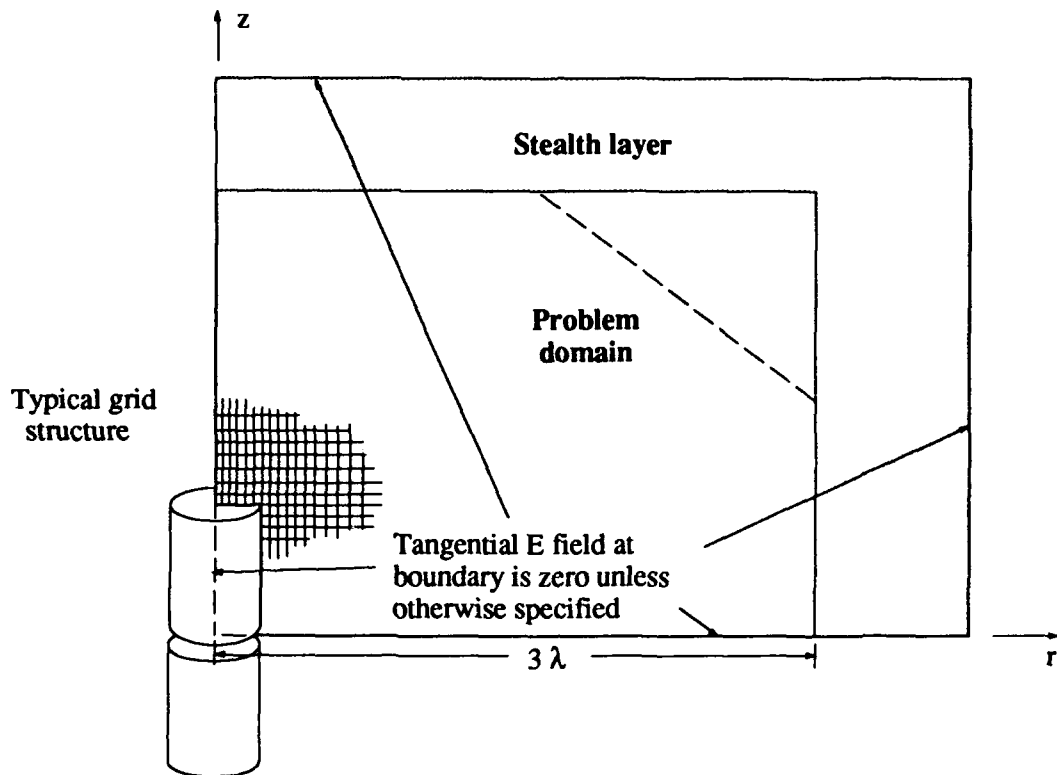


**Figure 3**

The finite difference grid structure used in HERZ. All magnetic field components are azimuthally directed and represented at the block centers, while the electric field components are represented on the block boundaries.

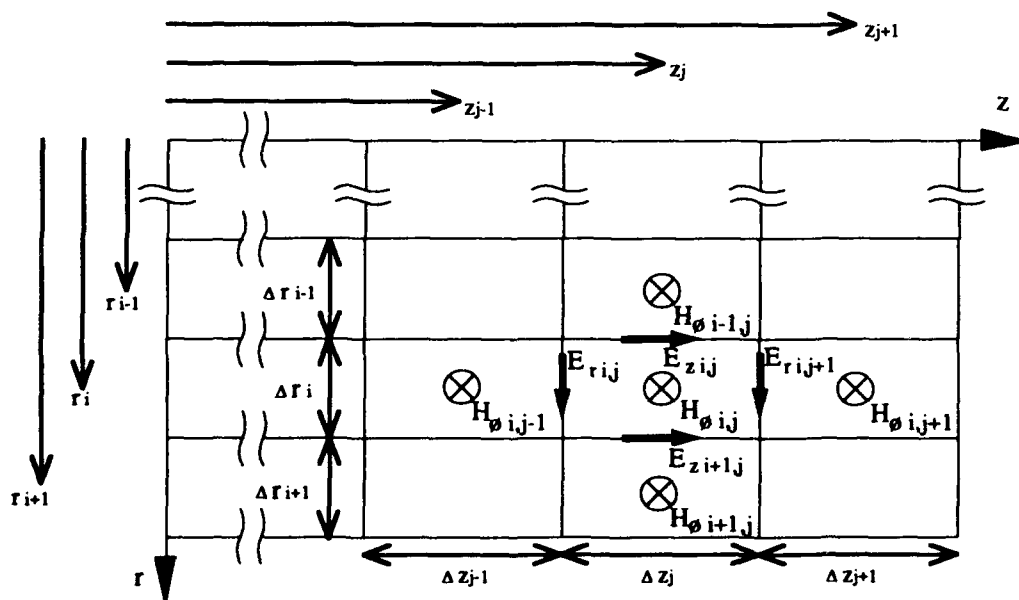
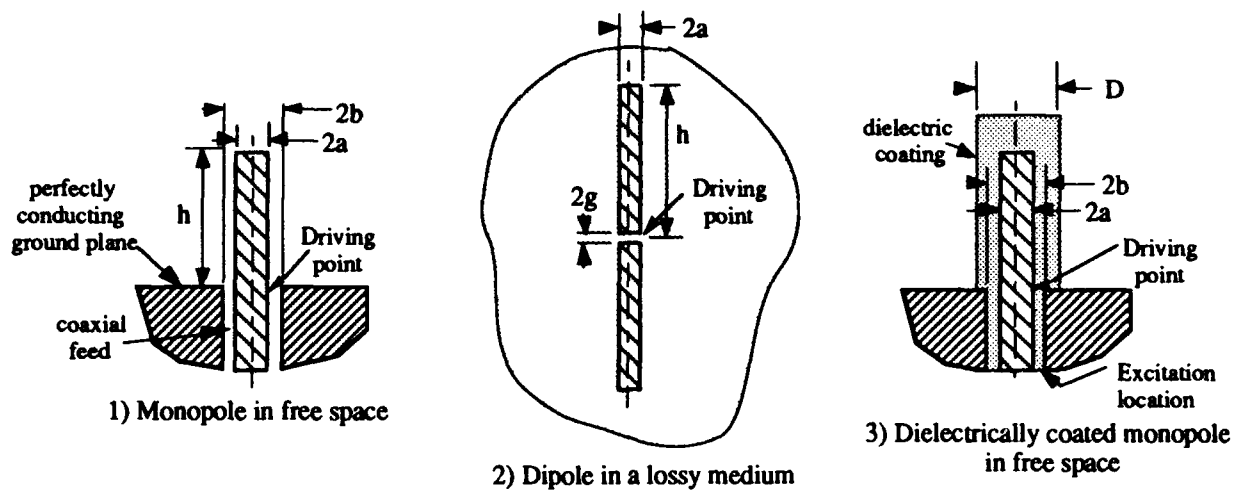


**Figure 4**  
Three antenna configurations modelled with HERZ



## RESULTS

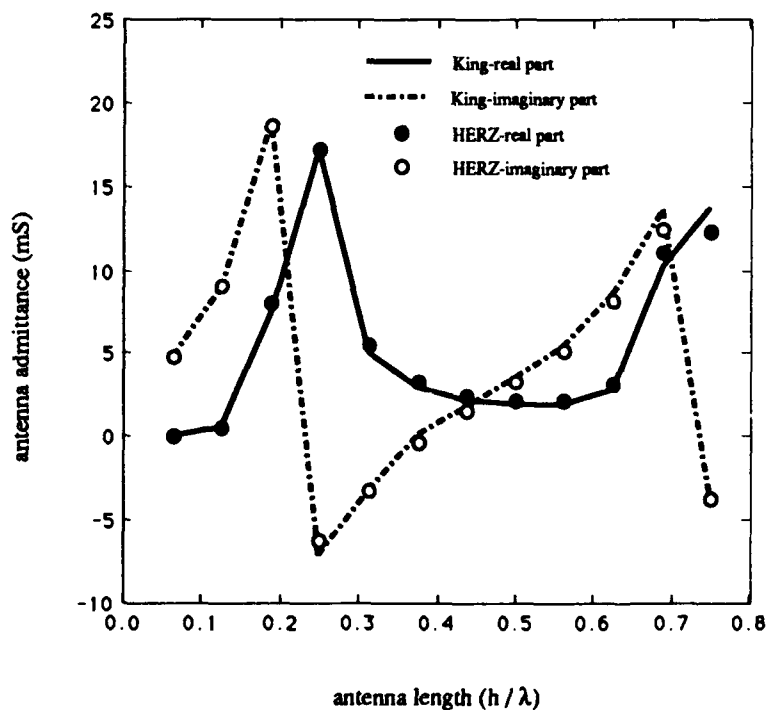


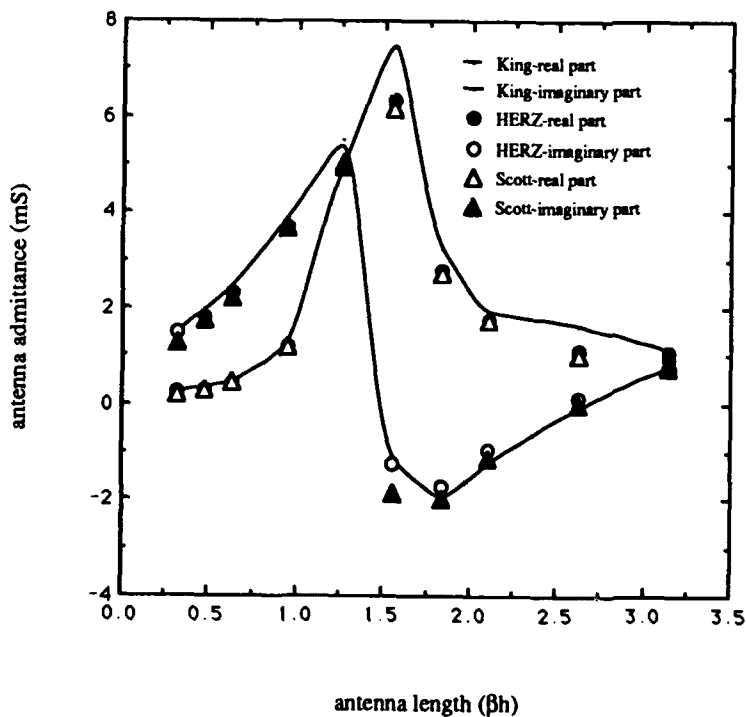
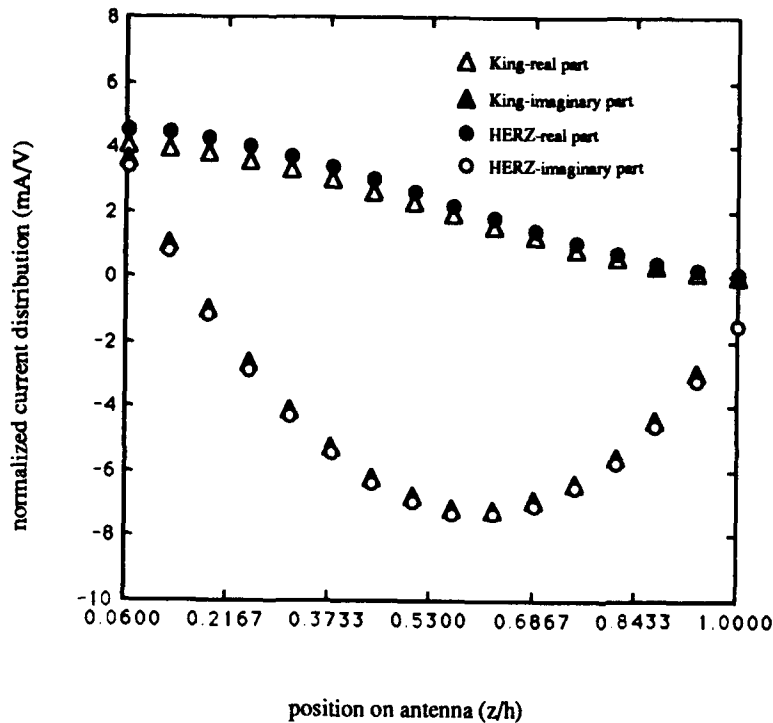
**Figure 5(a) Monopole in air**

The driving point admittance versus antenna length for a monopole on a conductive plane radiating into a lossless medium. Theoretical data published by King (1971, p.11) is used to validate HERZ's calculated values.

Frequency = 100 MHz

$a/\lambda = 0.0064$

$b/a = 1.189$



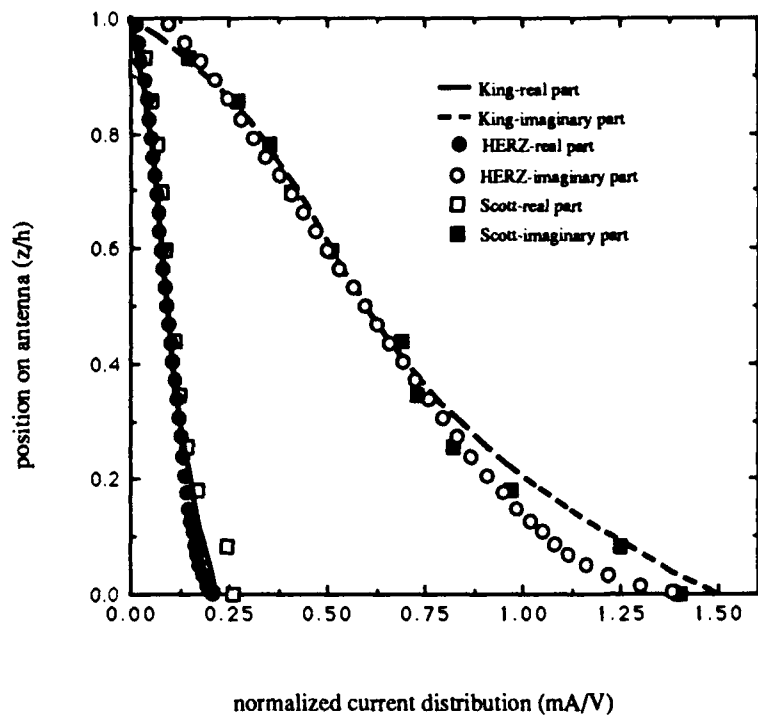


Figure 6(b) Dipole in a lossy medium

HERZ's normalized current distribution for a dipole radiating into a lossy medium is compared to theoretical data by King (1981, p.165) and the measured values by Scott.

Frequency = 114 MHz  
 $\beta\lambda = 0.315$   
 $a/\lambda = 0.0265$   
 $\alpha/\beta = 0.07$

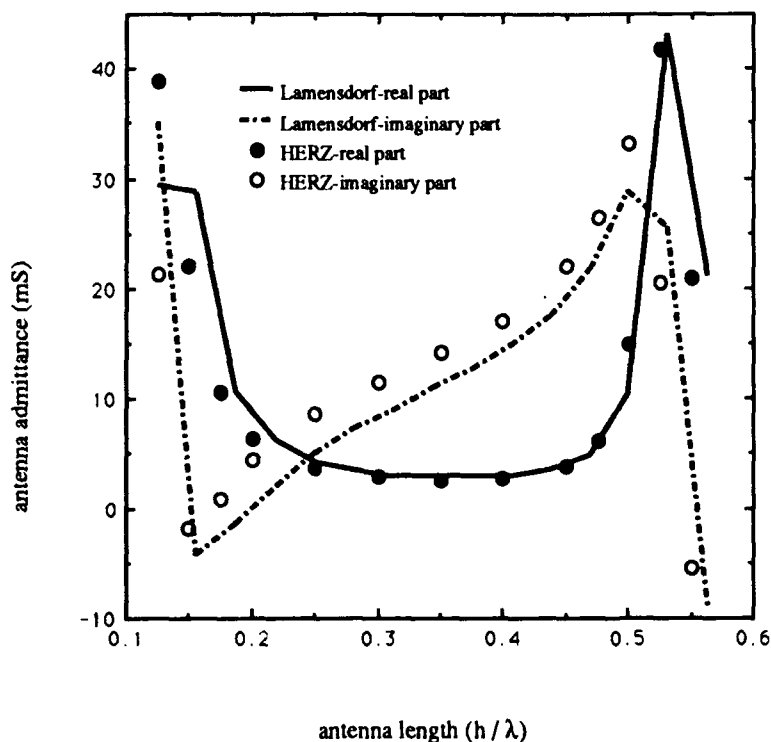
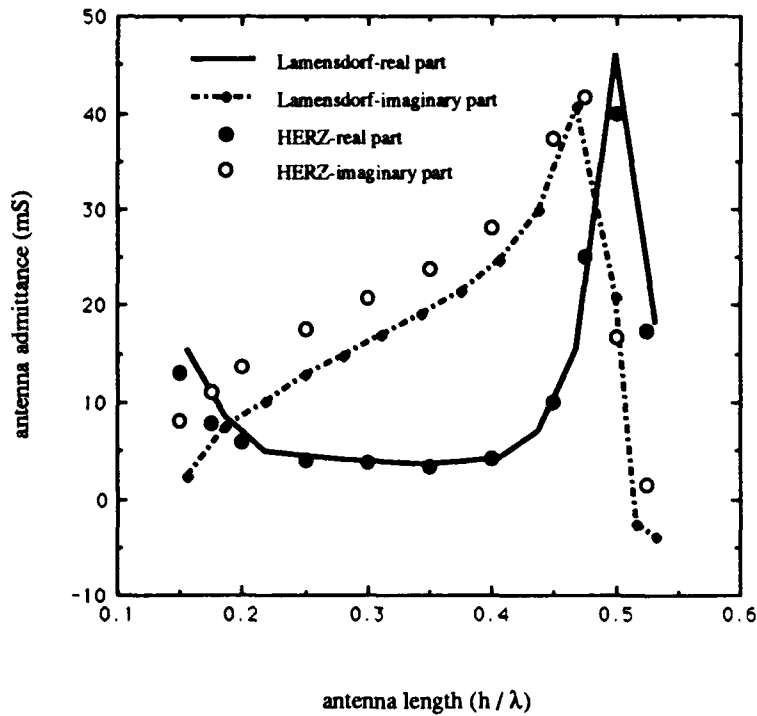


Figure 7(a) Dielectrically coated monopole in air

The driving point admittance versus antenna length for a dielectrically coated monopole in air as measured by Lamesdorf (1967) and calculated with HERZ.

Frequency = 600 MHz  
 $2a = 6.35$  mm  
 $2b = 19.05$  mm  
 $D = 23.77$  mm  
 $\epsilon_r = 9$   
 $\sigma = 0.001$  S/m



**Figure 7(b) Dielectrically coated monopole in air**

The driving point admittance versus antenna length for a dielectrically coated monopole in air as measured by Lamensdorf (1967) and calculated by HERZ.

Frequency = 600 MHz  
 $2a = 6.35$  mm  
 $2b = 19.05$  mm  
 $D = 23.77$  mm  
 $\epsilon_r = 15$   
 $\sigma = 0.001$  S/m

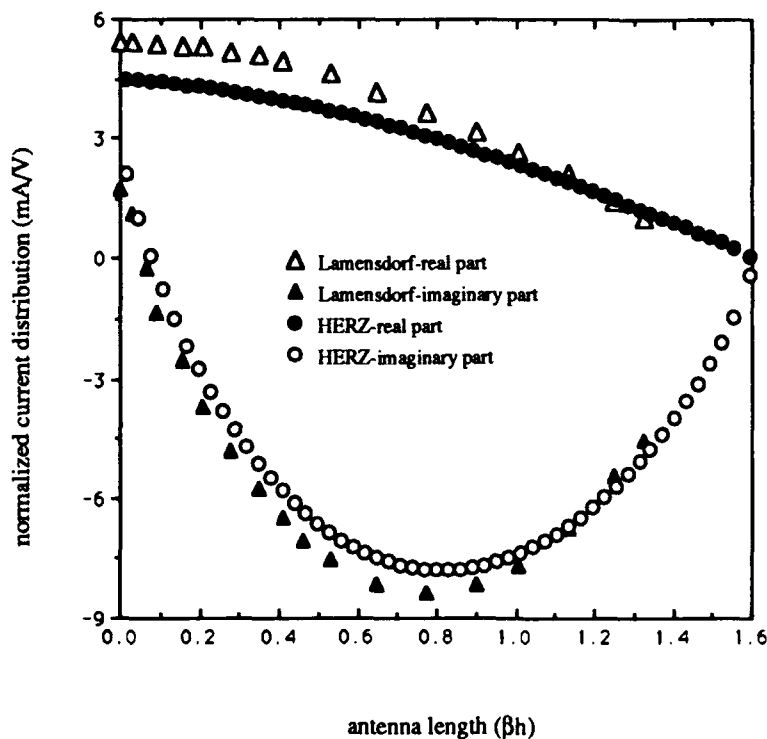


**Figure 7(c) Dielectrically coated monopole in air**

The normalized current distribution for a dielectrically coated monopole on a conducting plane operating in air. HERZ's calculated values are compared to Lamensdorf's measured values (1967).

Frequency = 600 MHz  
 $2a = 6.35$  mm  
 $2b = 19.05$  mm  
 $D = 50.79$  mm  
 $\epsilon_r = 3.2$   
 $\sigma = 0.0032$  S/m

# TWO WIRE RHOMBIC ILLUMINATOR PERFORMANCE AS PREDICTED BY THEORETICAL AND NUMERICAL MODELS

J. Patrick Donohoe<sup>\*</sup>  
Saad N. Tabet<sup>\*\*</sup>  
Clayborne D. Taylor<sup>\*</sup>

<sup>\*</sup>Department of Electrical and Computer Engineering  
Mississippi State University  
Mississippi State, Mississippi 39762

<sup>\*\*</sup>Department of Electrical Engineering  
FAMU/FSU College of Engineering  
Tallahassee, Florida 32316-2175

## ABSTRACT

*The two wire rhombic illuminator (RI) is a rhombic wire antenna located over a ground plane which is used to generate near uniform electromagnetic fields over a specified working volume located below the antenna. The RI can be modeled as a simple two-wire transmission line at low frequencies but the transmission line model becomes inadequate at higher frequencies due to the enhanced radiation properties of the antenna. The performance of the RI including radiation effects is evaluated numerically using the Numerical Electromagnetics Code (NEC-2) and compared to that of the transmission line model. The antenna in the presence of a perfectly conducting ground plane is analyzed at frequencies ranging from 1MHz to 500MHz. Various segmentation schemes are utilized in order to accurately predict the performance of the RI at frequencies where the dimensions of the structure are very large in terms of wavelength.*

## INTRODUCTION

The rhombic transmission line configuration has received much attention in recent years as an illuminator for surveillance testing of electromagnetic shielding. The first detailed study of such an illuminator was performed by Baum [1] and Shen and King [2,3,4]. The uniformity of the working volume fields for the two-wire rhombic illuminator were analyzed by Zuffada and Engheta [5] using a two-wire transmission line operating in the TEM mode. As noted in [5], the accuracy of the transmission line model diminishes as the frequency is increased due to the appearance of longitudinal modes.

In this paper, the validity of the RI transmission line model is investigated using a numerical solution technique. An illustration of the RI over a perfectly conducting ground plane is shown in Figure 1. The actual RI dimensions and working volume location are shown in Figure 2. All wires have a diameter of 3.175mm. The antenna current and the individual components of the working volume electric field are computed over a range of 1MHz to 500MHz. Several aspects of the RI performance are noted with regard to the behavior of the antenna currents and working volume fields with frequency.

The RI may be driven in the common-mode (push-push) configuration with respect to the ground plane. The four wires of the RI are denoted as wire #1 and wire #3 (which make up the launch region) which are connected with wire #2 and wire #4, respectively, (which make up the termination region).

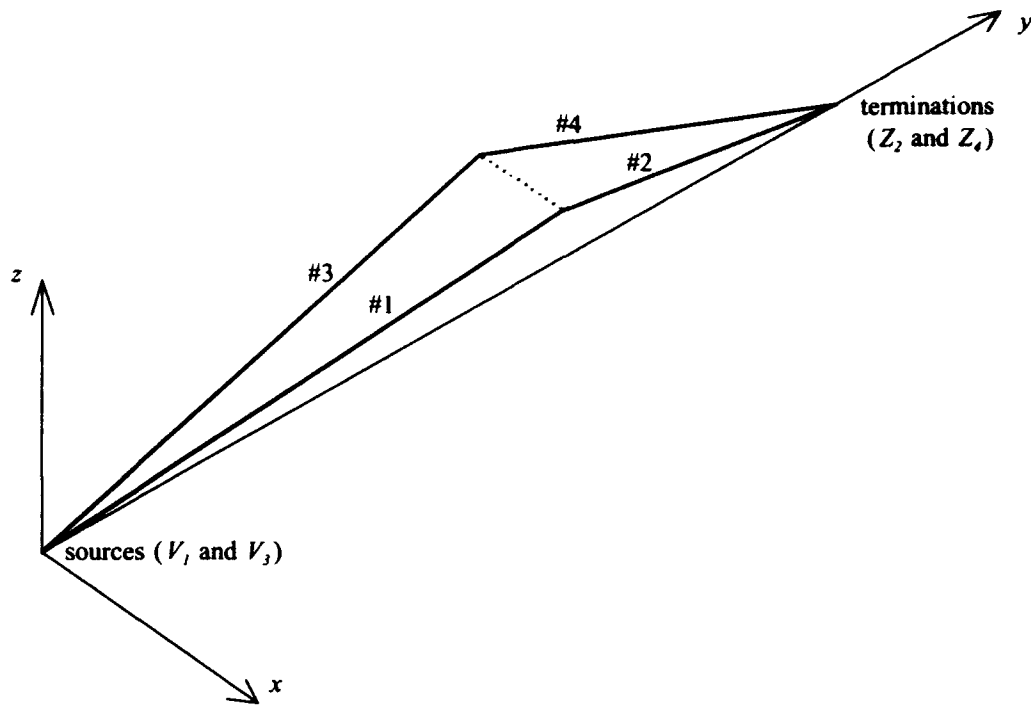


**Figure 1.** Rhombic illuminator (RI) wire configuration.

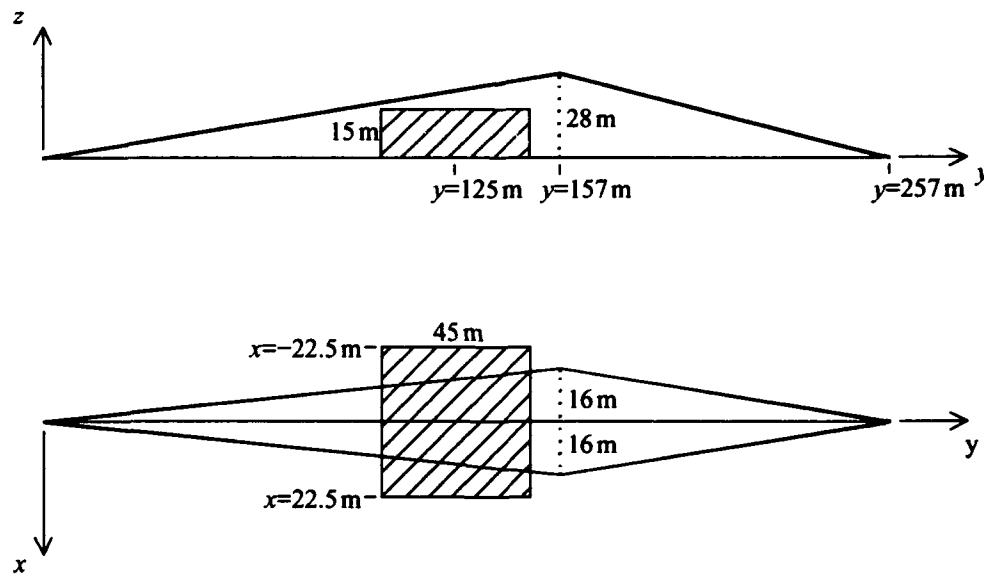


**Figure 2.** Rhombic illuminator and working volume dimensions.

The common mode excitation of the RI yields an electric field which is predominantly vertical in the given working volume.

### TRANSMISSION LINE MODEL OF THE RHOMBIC ILLUMINATOR

As previously mentioned, the RI may be modeled by a two-wire transmission line over a perfectly conducting ground plane at low frequencies. The TEM fields of the two-wire line under common-mode excitation are obtained by considering the static field of equivalent line charges over a perfectly conducting ground plane. For the given working volume dimensions, the values of the wire separation and wire height above ground may be optimized with regard to field uniformity [5].

The larger vertical component of the common-mode electric field is designated as the principal component while the smaller horizontal electric field component is referred to as the nonprincipal field component. The principal and nonprincipal fields ( $E_z$  and  $E_x$ , respectively) for the common-mode excitation [5,8,9] are given by

$$E_z = \frac{q}{2\pi\epsilon_0} \left[ \frac{(z-b)}{(x-a)^2+(z-b)^2} + \frac{(z-b)}{(x+a)^2+(z-b)^2} - \frac{(z+b)}{(x-a)^2+(z+b)^2} - \frac{(z+b)}{(x+a)^2+(z+b)^2} \right] \quad (1)$$

(Common-mode Principal Component)

$$E_x = \frac{q}{2\pi\epsilon_0} \left[ \frac{(x+a)}{(x-a)^2+(z-b)^2} + \frac{(x-a)}{(x-a)^2+(z-b)^2} - \frac{(x+a)}{(x-a)^2+(z+b)^2} - \frac{(x-a)}{(x-a)^2+(z+b)^2} \right] \quad (2)$$

(Common-mode Nonprincipal Component)

where  $q$  is the line charge density,  $\epsilon_0$  is the permittivity of vacuum,  $2a$  is the distance between the wire centers and  $b$  is the height of the wires above the ground plane. The value of the line charge density in (1) and (2) is related to the potential difference between each of the wires and ground ( $V$ ) and the characteristic impedance of the common-mode two-wire line shown in Figure 3 as given by

$$\frac{q}{2\pi\epsilon} = 30 \frac{V}{Z_{cm}} \quad (3)$$

The characteristic impedance of the two-wire line ( $Z_{cm}$ ) under common-mode excitation is

$$Z_{cm} = \frac{\eta_0}{4\pi} \left\{ \ln \left[ \frac{1 + [1 + (r/b)^2]^{1/2} - (r/b)}{1 - [1 + (r/b)^2]^{1/2} + (r/b)} \right] + \frac{1}{2} \ln [1 + (b/a)^2] \right\} \quad (4)$$

where  $\eta_0$  is the intrinsic impedance of vacuum and  $r$  is the radius of the wires.

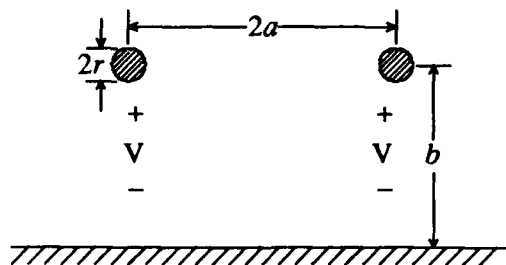


Figure 3. Common-mode two wire line over ground.

The principal and nonprincipal transverse electric fields in the working volume of the RI are symmetric about the  $y$ - $z$  plane given common-mode excitation. Therefore, the field behavior over the entire transverse cross-section of the working volume given by  $[-22.5\text{ m} \leq x \leq 22.5\text{ m}]$  and  $[0 \leq z \leq 15\text{ m}]$  is evident given the fields over the cross-section defined by  $[0 \leq x \leq 22.5\text{ m}]$  and  $[0 \leq z \leq 15\text{ m}]$ . The transverse cross-section located at the center of the working volume ( $y=125\text{ m}$ ) is designated as  $S_{wv}$  and is shown in Figure 4. For purposes of comparison, the individual electric field components are plotted over  $S_{wv}$ . The dimensions of the RI at  $y=125\text{ m}$  are  $2a=25.48\text{ m}$  (wire separation) and  $b=20.70\text{ m}$  (wire height above the ground plane).

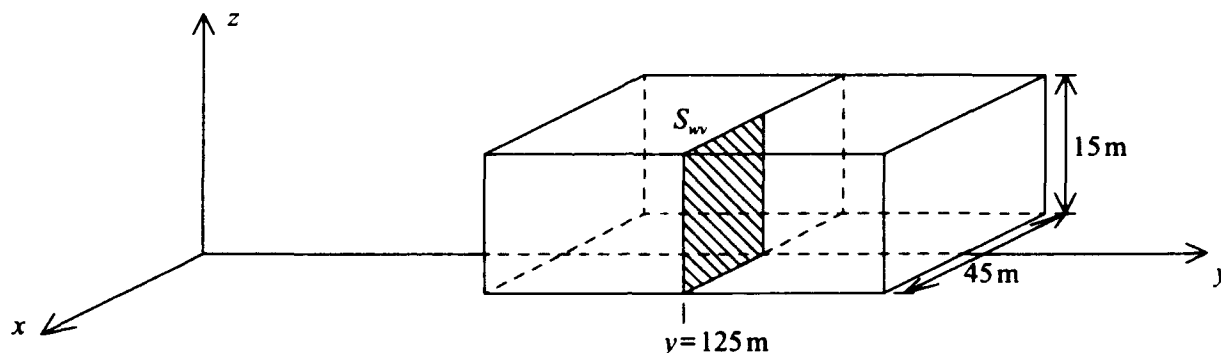
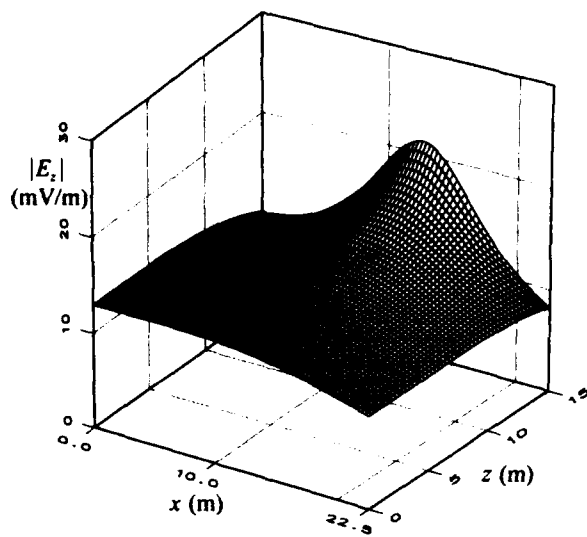


Figure 4. Working volume cross-sectional surface ( $S_{wv}$ ) over which fields are plotted.

The transverse electric field components of a similarly spaced two-wire transmission line over a ground plane ( $2a=25.48\text{ m}$ ,  $b=20.70\text{ m}$ ,  $r=1.5875\text{ mm}$ ) with  $V=1\text{ V}$  are shown in Figures 5 and 6. The principal electric field component of the transmission line model shown in Figure 5 contains a broad peak along the upper edge of the working volume ( $z=15\text{ m}$ ) which corresponds to points directly below the transmission line conductor. The principal electric field is relatively uniform over the remainder of the working volume. The nonprincipal electric field component shown in Figure 6 is zero-valued along the lower edge of the working volume (tangent to the ground plane) and increases in magnitude as the observation point is moved away from the ground plane. The nonprincipal electric field contains a null along the upper edge of the working volume which corresponds to the point where the horizontal components due to both wires and their images cancel one another. The  $x$ -coordinate of this null lies between the transmission line center point at  $x=0$  and the coordinate of the transmission line conductor at  $x=a$ . The transverse fields of the transmission line model are compared to the fields generated by the corresponding *NEC* thin-wire model of the RI described in the following section.

#### NUMERICAL MODEL OF THE RHOMBIC ILLUMINATOR

The number of segments required to model each of the four wires of the RI using *NEC-2* is based on the frequency of operation. In general, the segment lengths should be chosen in the range of  $0.001\lambda$  to  $0.1\lambda$  to maintain numerical stability [6]. This segment length requirement makes the analysis of electrically long thin-wire structures (such as the RI at high frequencies) computationally prohibitive. However, the segment lengths can be exponentially graded over the entire wire ("entire grading") or a portion of each wire ("partial grading") [7,8,9] to minimize the number of segments required for an accurate solution of the RI geometry. These segmentation schemes allow for electrically short segments in critical regions (source, termination, wire bends) while allowing for longer segments over the remainder of the structure.



**Figure 5.** Principal transverse electric field magnitude on  $S_{wv}$  (transmission line model).

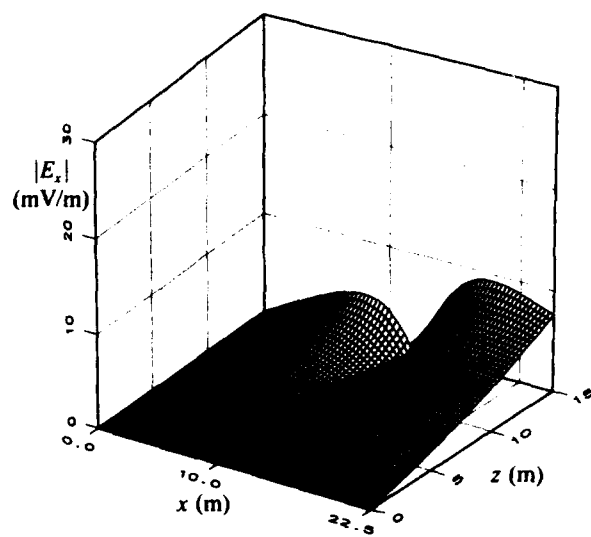


**Figure 6.** Nonprincipal transverse electric field magnitude on  $S_{wv}$  (transmission line model).

The segments on the launching region wires (#1 and #3) are numbered from the ground plane to the apex of the RI. That is, the first segment on each launch wire is connected to the ground plane while the last segment is connected to the termination wire at the apex. The segments on the termination region wires (#2 and #4) are numbered from the apex to the ground plane. The two common-mode voltage sources (applied electric-field sources),  $V_{S1}$  and  $V_{S2}$ , are placed on the second segment of wire #1 and wire #3, respectively. The magnitude of both voltage sources is one volt with a phase of zero degrees. The terminations placed on the last segments of wire #2 and wire #4 are lumped resistive loads of  $630\Omega$ . The  $630\Omega$  lumped resistive value corresponds to twice the average common-mode characteristic impedance along the length of the RI as given in Equation (4).

*NEC* allows for the utilization of structural symmetry to simplify the geometry input as well as the solution process. The RI configuration shown in Figure 1 is symmetric about the  $y$ - $z$  plane. Thus, using symmetry, only wire #1 and wire #2 are needed to describe the entire RI structure. The voltage sources are not reflected using symmetry so that both sources of the RI must be defined explicitly. *NEC* does, however, allow for the reflection of loaded segments so that the resistively-loaded segment on wire #2 is automatically reflected to wire #4 using symmetry.

The previously defined thin-wire model of the RI is analyzed using discrete *NEC* models over a frequency range of 1 MHz to 500 MHz. The *NEC* models developed for the RI are highly sensitive to the frequency of operation because of the critical nature of the segment length with regard to wavelength. For this reason, the RI model is analyzed at five distinct frequencies: 1 MHz, 10 MHz, 100 MHz, 300 MHz and 500 MHz. The RI current and electric field components over  $S_{wv}$  are computed at each frequency. The total number of unknowns ( $N_{total}$ ) is equal to the total number of segments required to model a symmetric cell (wire #1 plus wire #2). Within *NEC*, the maximum array dimension with regard to the number of segments must be  $2N_{total}$ . The total length of the RI symmetric cell is approximately 265 m. The total electrical lengths of the RI symmetric cell at the various frequencies of interest are listed in Table 1.

The RI at 1 MHz is easily modeled with "optimum" length segments of  $0.01\lambda$ . The length of  $0.01\lambda$  lies one order of magnitude above the recommended minimum segment length and one order of magnitude below the maximum recommended segment length. Wire #1 and wire #2 are divided into equal segments

of length approximately  $0.01\lambda$  which yields 54 segments on wire #1 and 35 segments on wire #2 for a total of 89 segments in a symmetric cell.

The total length of wire #1 plus wire #2 at 10MHz is approximately  $8.8\lambda$ . Thus, approximately 880 segments would be required to model the RI with  $0.01\lambda$  segments. Yet, the use of this many segments yields a solution which is unnecessarily lengthy. The accuracy of the *NEC* model for long straight wires is not appreciably affected by using segments which are longer than  $0.01\lambda$  away from the critical regions of the structure [6]. Thus, by exponentially grading the segments along the RI wires, the total number of segments required can be reduced significantly. The segments near the source must be short and of comparable length to yield accurate representations of the applied electric field sources. Therefore, the first segment on wire #1 is chosen to be  $0.01\lambda$  in length. The partial grading technique is then used with a grading factor of 1.1 (10% increase in length from segment to segment) until the segments reach a maximum length of  $\Delta_{max}=0.1\lambda$ . The same segment grading is used at the apex end of wire #1. The remaining midsection of wire #1 is modeled with uniform length segments of length  $\Delta_{max}$ . The same segmentation scheme is applied to the termination wire (wire #2) resulting in 83 segments on wire #1 and 65 segments on wire #2 for a total of 148 segments.

At 100MHz, the total electrical length of the symmetric cell is approximately  $88\lambda$ . In order to significantly reduce the number of segments required at this frequency, the partial grading scheme must be employed. As in the 10MHz case, the shortest segments on wire #1 and wire #2 are defined with lengths of  $0.01\lambda$  and a grading factor of 1.1 is used for the weighted portions of the wires. The maximum segment length is chosen to be  $\Delta_{max}=0.2\lambda$ . This segmentation results in 310 segments on wire #1 and 218 segments on wire #2 which yields  $N_{total}=528$ .

The total electrical length of the symmetric cell at 300MHz is approximately  $264\lambda$ . The same segmentation scheme as outlined for the 10MHz and 100MHz cases is used for the 300MHz case. The grading factor is again chosen to be 1.1 while the maximum segment length is chosen as  $0.3\lambda$ . The resulting segment totals on wire #1 and wire #2 are 585 and 400, respectively. Thus, the total number of segments in the symmetric cell is 985.

The previously defined segmentation scheme is applied to the RI at 500MHz. The electrical length of the RI symmetric cell at 500MHz is in excess of  $440\lambda$ . A grading factor of 1.1 and a maximum segment length of  $0.4\lambda$  are utilized. This model of the RI yields 724 segments on wire #1 and 493 segments on wire #2. Thus, the entire symmetric cell requires a total of 1217 segments.

The characteristics of the five *NEC* models are summarized in Table 1. The use of *NEC* models which contain segment lengths in excess of  $0.1\lambda$  requires special consideration with regard to the interaction approximation distance within *NEC*. When segments are separated by more than a prescribed distance (known as the interaction approximation distance), the source segment is modeled as an infinitesimal current element at the segment center. This approximation is accurate when using short segments. However, longer segments may have significant variation of current magnitude and phase along the length of the segment which makes this approximation inaccurate. Thus, when using longer segments, the interaction approximation must not be utilized. The interaction approximation distance may be defined by the user but a default value of 1m is assumed in *NEC*. In the results given here, the interaction approximation distance is defined large enough that the interaction approximation is not implemented.

## NUMERICAL RESULTS FOR THE THIN-WIRE RI MODEL

The magnitude of the resulting current along wire #1 and wire #2 of the RI is shown in Figure 7. The current magnitude at 1MHz exhibits a standing wave pattern that is very slightly damped along the length of the two wires. The principal transverse, nonprincipal transverse and longitudinal components of the electric field over  $S_w$  are shown in Figures 8, 9 and 10, respectively. The transverse electric field plots may be compared with those of the two-wire transmission line (Figures 5 and 6). As expected, the general distribution of transverse electric field components are nearly identical to those of the two-wire

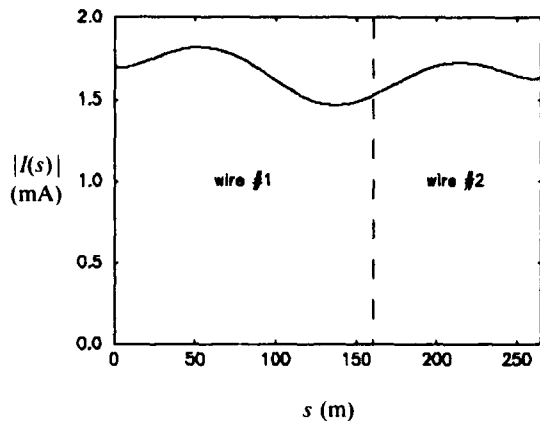


**Figure 7.** RI current magnitude on wires #1 and #2 at 1 MHz.

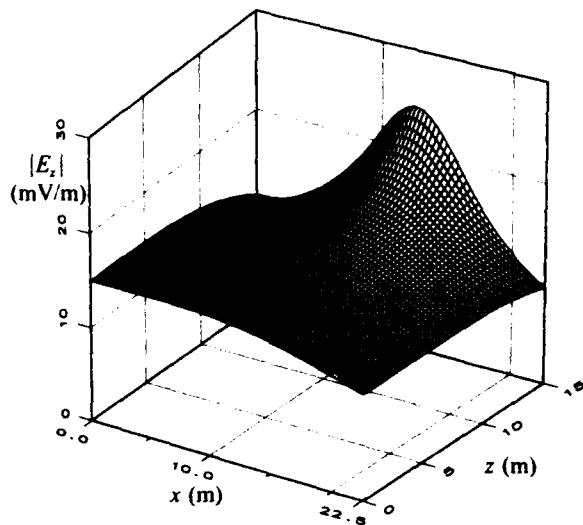


**Figure 8.** Principal transverse electric field magnitude on  $S_{wv}$  at 1 MHz.

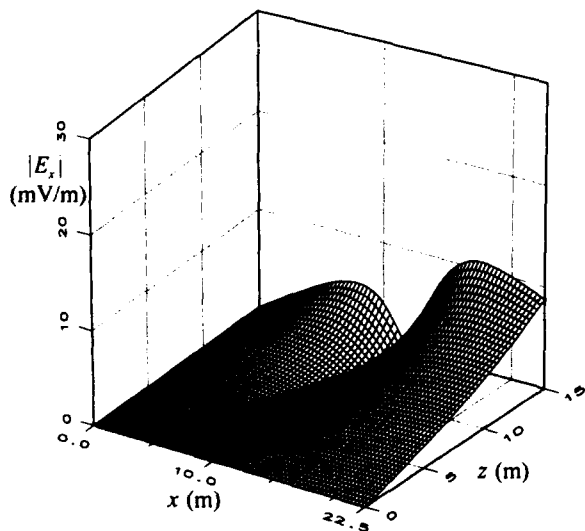


**Figure 9.** Nonprincipal transverse electric field magnitude on  $S_{wv}$  at 1 MHz.

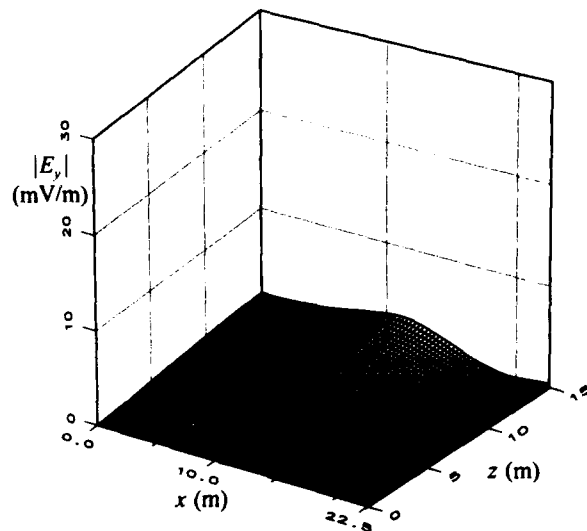


**Figure 10.** Longitudinal electric field magnitude on  $S_{wv}$  at 1 MHz.

$f$ (MHz)	Total length (wire #1 + wire #2)	Segment grading scheme	$\Delta_{max}$	$N_{total}$
1	0.8822 $\lambda$	none	0.01 $\lambda$	89
10	8.822 $\lambda$	partial	0.1 $\lambda$	148
100	88.22 $\lambda$	partial	0.2 $\lambda$	528
300	264.7 $\lambda$	partial	0.3 $\lambda$	985
500	441.1 $\lambda$	partial	0.4 $\lambda$	1217

**Table 1.** Descriptions of the RI *NEC* models.

transmission line TEM mode. The magnitudes of the transverse electric field components for the RI model are slightly higher than the corresponding transmission line values. The magnitude of the longitudinal electric field component is small in comparison with the transverse components.

The magnitude of the current along wires #1 and #2 of the RI at 10MHz is plotted in Figure 11. The corresponding electric field components are plotted over  $S_{wv}$  and appear in Figures 12, 13 and 14. The magnitude of the RI source current at 10MHz exhibits a significant increase when compared to the 1MHz value. Yet, the RI current at 10MHz exhibits a slightly higher rate of decay than the 1MHz distribution. The general shapes of the electric field components, both transverse and longitudinal, remain unchanged from the 1MHz values. The magnitudes of all three electric field components at 10MHz are slightly larger than the corresponding 1MHz values.

The 100MHz RI current magnitude is shown in Figure 15. The resulting 100MHz working volume electric field components are given in Figures 16, 17 and 18. An increase in the magnitude of the source current from 10MHz to 100MHz is observed. However, the damping factor of the 100MHz current is larger than that of the 10MHz current yielding only slightly higher values of current magnitude in the vicinity of the working volume (near the wire apex). The magnitudes of both the transverse and longitudinal components of the working volume electric field exhibit a slight increase over the corresponding values at 10MHz. The variation in the working volume field components with respect to wavelength becomes apparent at 100MHz as shown in Figures 16, 17 and 18.

The current magnitude along the RI wires at 300MHz is plotted in Figure 19, while the corresponding electric field components over  $S_{wv}$  are plotted in Figures 20, 21 and 22. A general trend is evident in the variation of the RI current and working volume field values as a function of frequency. As the frequency of operation is increased, the source current magnitude is increased. The standing wave pattern along the RI wires stays relatively constant with frequency. The resulting working volume electric field components exhibit a small increase in magnitude as the frequency is increased.

The magnitude of the current on wires #1 and #2 of the RI at 500MHz is shown in Figure 23. The electric field components in the working volume of the RI at 500MHz are shown in Figures 24, 25 and 26. The current magnitude at the source is slightly larger than that of the 300MHz case but the current distribution away from the source is quite similar to that of the 300MHz case. The standing wave amplitude is slightly higher than that of the 300MHz case. The working volume field components exhibit a small increase in amplitude over the 300MHz case as expected.

In order to test the convergence of the previous *NEC* solutions when using relatively long segments, the 300MHz and 500MHz cases are modeled with slightly shorter segments and the resulting currents are compared with the currents obtained with the initial models. These comparisons are shown in Figures 27 and 28. For both the 300MHz and 500MHz cases, the current distributions are quite similar with only minor variations in the standing wave amplitude.

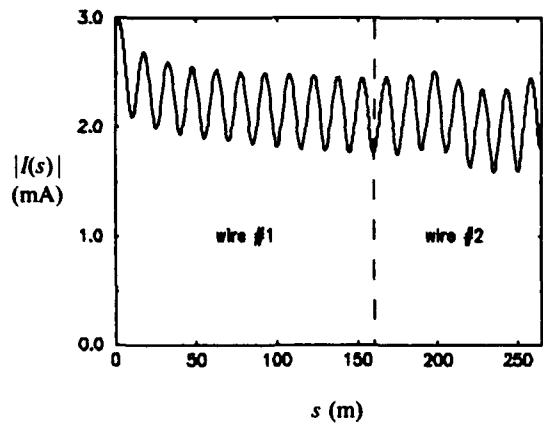


**Figure 11.** RI current magnitude on wires #1 and #2 at 10MHz.

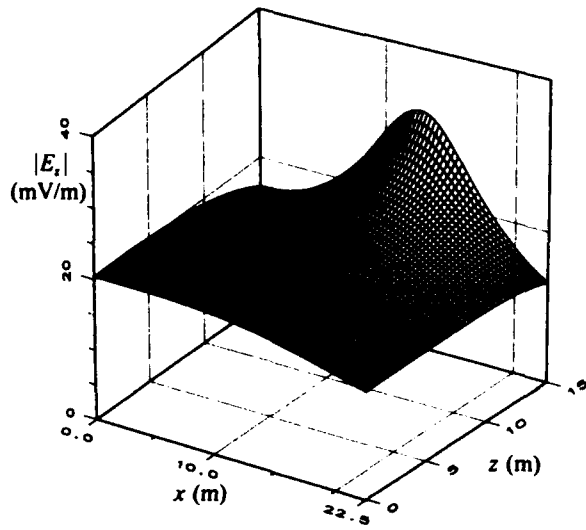


**Figure 12.** Principal transverse electric field magnitude on  $S_{wv}$  at 10 MHz.

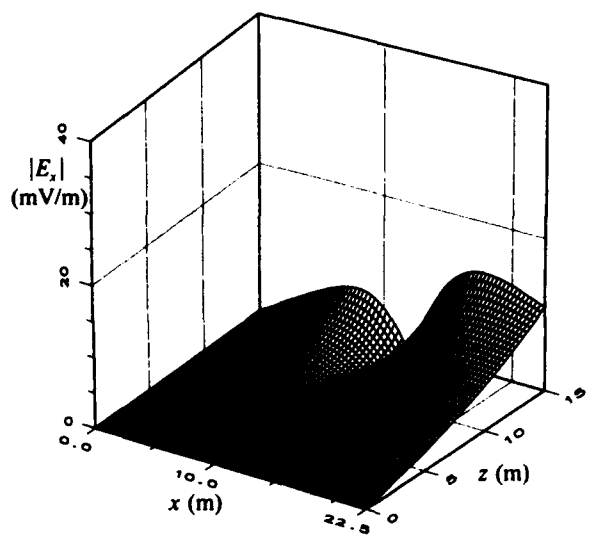


**Figure 13.** Nonprincipal transverse electric field magnitude on  $S_{wv}$  at 10 MHz.

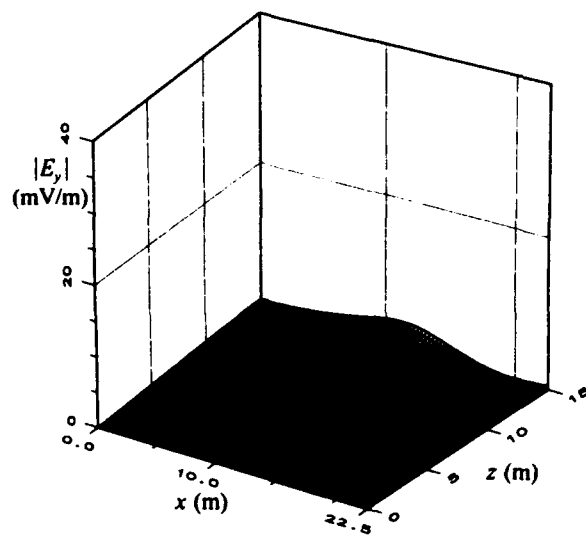


**Figure 14.** Longitudinal electric field magnitude on  $S_{wv}$  at 10 MHz.

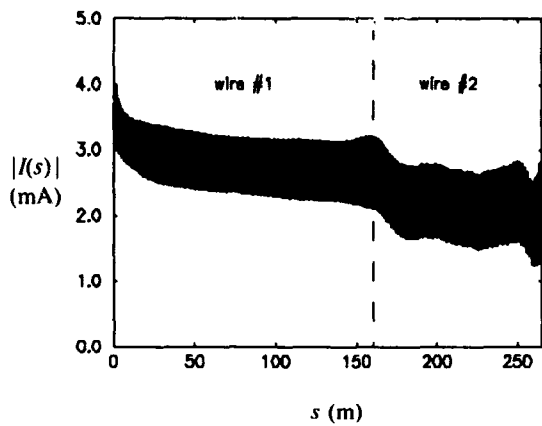


**Figure 15.** RI current magnitude on wires #1 and #2 at 100MHz.

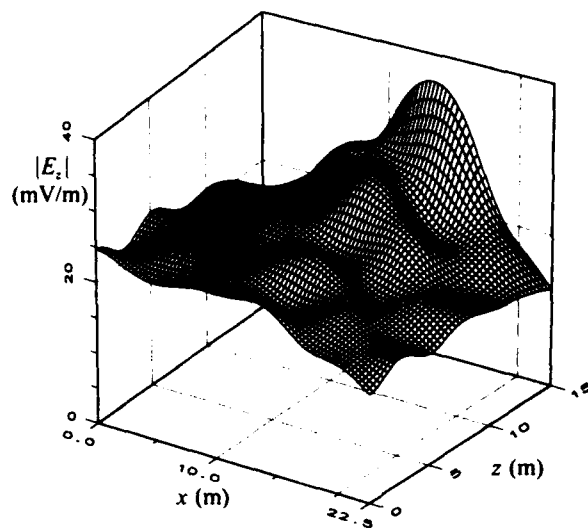


**Figure 16.** Principal transverse electric field magnitude on  $S_{wv}$  at 100 MHz.

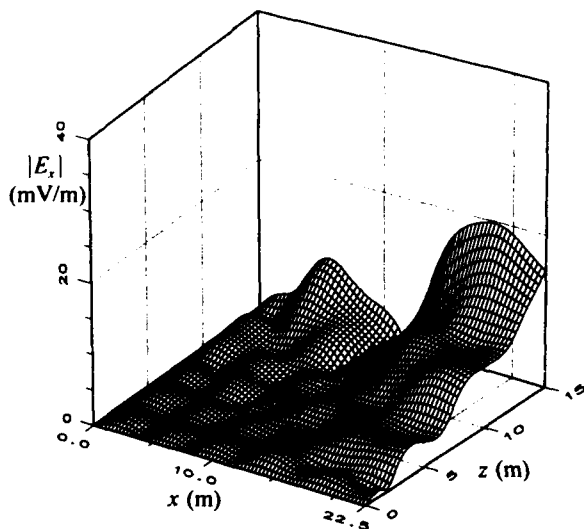


**Figure 17.** Nonprincipal transverse electric field magnitude on  $S_{wv}$  at 100 MHz.

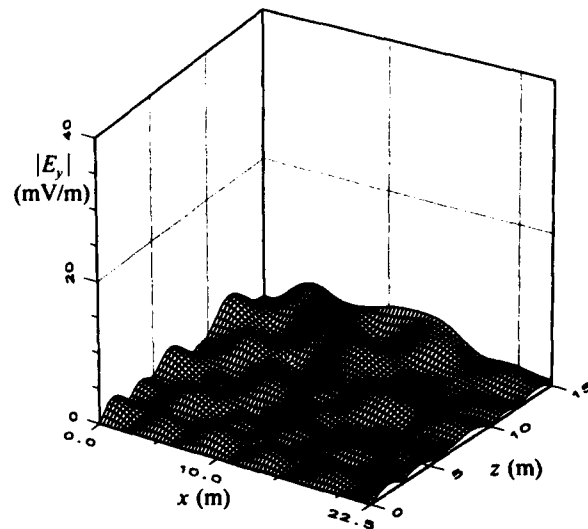


**Figure 18.** Longitudinal electric field magnitude on  $S_{wv}$  at 100 MHz.

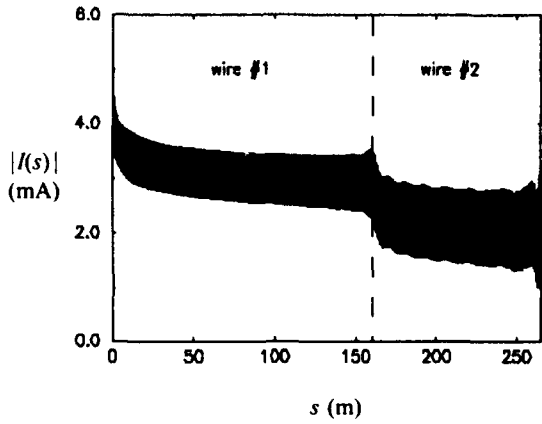


**Figure 19.** RI current magnitude on wires #1 and #2 at 300MHz.

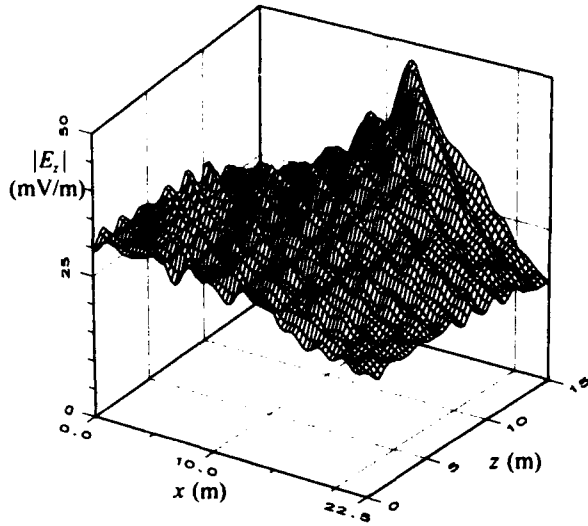


**Figure 20.** Principal transverse electric field magnitude on  $S_{wv}$  at 300 MHz.

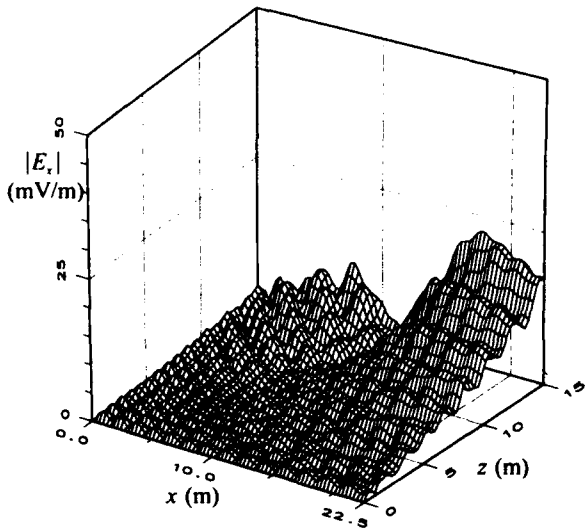


**Figure 21.** Nonprincipal transverse electric field magnitude on  $S_{wv}$  at 300 MHz.

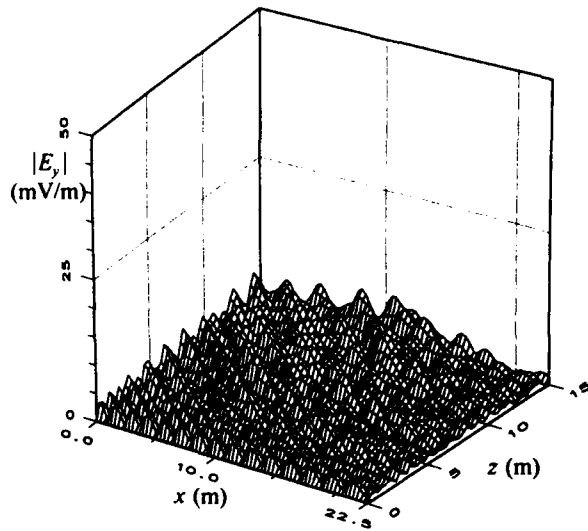


**Figure 22.** Longitudinal electric field magnitude on  $S_{wv}$  at 300 MHz.

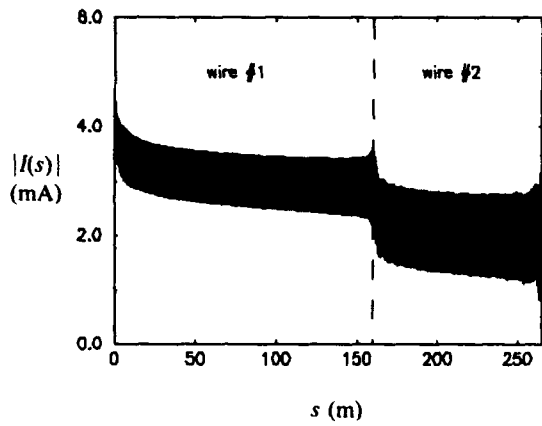


**Figure 23.** RI current magnitude on wires #1 and #2 at 500MHz.

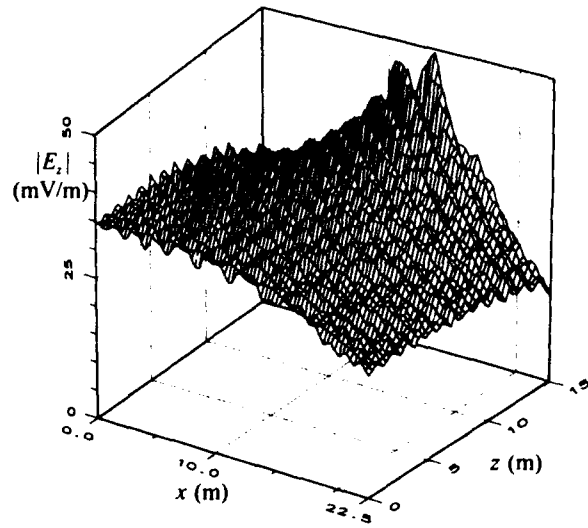


**Figure 24.** Principal transverse electric field magnitude on  $S_{wv}$  at 500 MHz.

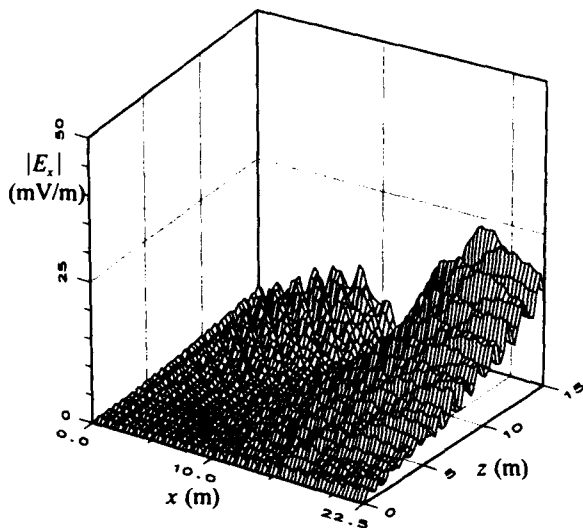


**Figure 25.** Nonprincipal transverse electric field magnitude on  $S_{wv}$  at 500 MHz.

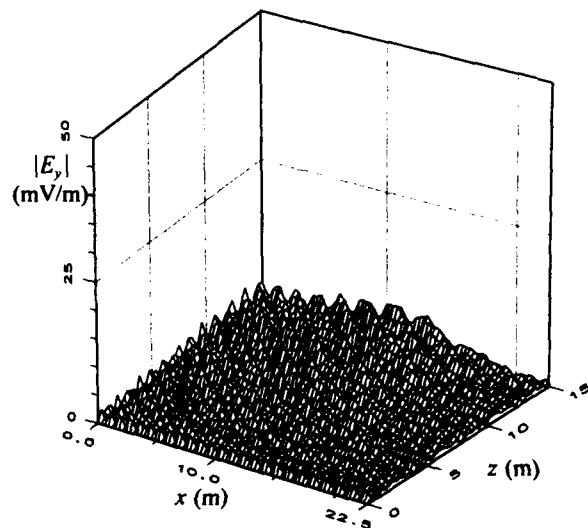


**Figure 26.** Longitudinal electric field magnitude on  $S_{wv}$  at 500 MHz.

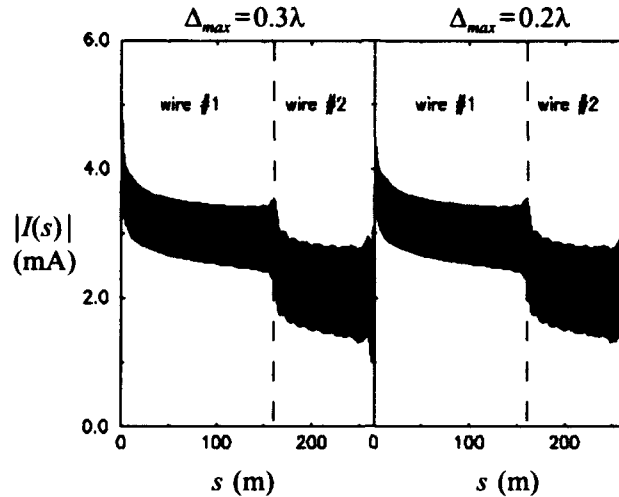


Figure 27. Comparison of RI current magnitude at 300MHz with  $\Delta_{max}=0.3\lambda$  and  $\Delta_{max}=0.2\lambda$

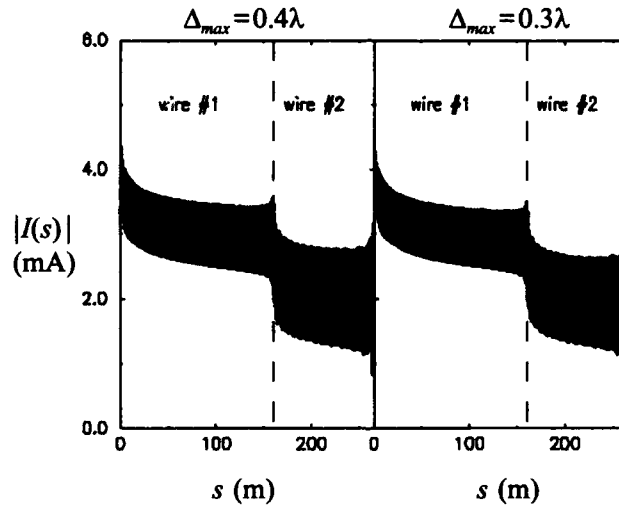


Figure 28. Comparison of RI current magnitude at 500MHz with  $\Delta_{max}=0.4\lambda$  and  $\Delta_{max}=0.3\lambda$

### ANALYSIS OF RESULTS AND CONCLUSIONS

The rhombic illuminator configuration has been analyzed using a numerical solution technique over the frequency range of 1MHz to 500MHz. The numerical solution is obtained using *NEC* with five discrete models at 1, 10, 100, 300 and 500MHz. The antenna current and the working volume electric field components were computed and compared to the fields obtained using the two-wire transmission line TEM model. The current along the wires of the illuminator was found to display several basic physical characteristics. The current exhibited a damped standing wave pattern which remains relatively constant over the frequency range of interest. Reflections from the wire bend become evident at frequencies of 100MHz and above. The current magnitude in the source region increases rapidly from 1 to 100MHz and at a slower rate at the higher frequencies. Overall, the average current magnitude along the RI wires is relatively constant over the given frequency range.

The electric field components in the working volume also exhibit several distinct characteristics. The magnitudes of the working volume fields increase with frequency since the peak currents on the antenna also increase with frequency. The general shapes of the field component distributions depend on the distribution of current on the illuminator wires. Since the current magnitude distribution is relatively constant over the frequency range of interest, the field component distributions also remain relatively constant. The magnitude of the longitudinal electric field component remains quite small in comparison to the principal transverse component indicating that no significant longitudinal modes are excited at frequencies of 500MHz and below. As shown in Figures 8, 12, 16, 20 and 24, the RI performance is satisfactory up to 500MHz with regard to the uniformity of the principal transverse field in the working volume. The transmission line model yields an accurate prediction of the general shape of the working volume transverse field component distributions but does not accurately predict the magnitudes of these fields [10]. At 500MHz, the transverse fields are roughly three times larger than those predicted by the theoretical model. It may be possible to reduce the standing wave amplitude along the structure at the various frequencies by improved load matching or through the use of distributed loading along the wires.

### REFERENCES

1. C. E. Baum, "Impedances and Field Distributions for Symmetrical Two Wire and Four Wire Transmission Line Simulators," *Sensor and Simulation Notes*, Note 27, AFWL, Kirtland AFB, June 1970.
2. H-M. Shen and R. W. P. King, "The Rhombic EMP Simulator," *IEEE Transactions on Electromagnetic Compatibility*, Vol. EMC-24, No. 2, pp. 255-265, May 1982.
3. H-M. Shen and R. W. P. King, "Experimental Investigation of the Rhombic EMP Simulator: Comparison with Theory and Parallel Plate Simulator," *IEEE Transactions on Electromagnetic Compatibility*, Vol. EMC-24, No. 3, pp. 349-355, August 1982.
4. H-M. Shen and R. W. P. King, "Theoretical Analysis of the Rhombic Simulator Under Pulse Excitation," *IEEE Transactions on Electromagnetic Compatibility*, Vol. EMC-25, No. 1, pp. 47-55, February 1983.
5. C. Zuffada and N. Engheta, "Field Uniformity Criteria for the Design of a Two-Wire EMP Simulator," *Electromagnetics*, Vol. 8, No. 1, pp. 29-35, 1988.
6. G. J. Burke and A. J. Poggio, "Numerical Electromagnetics Code (NEC) - Method of Moments," Vol. 2, Naval Ocean Systems Center, Technical Report NOSC TD 116, January 1981.
7. S. N. Tabet, J. P. Donohoe, and C. D. Taylor, "Using Nonuniform Segment Lengths with NEC to Analyze Electrically Long Wire Antennas," *Applied Computational Electromagnetics Society Journal*, Vol. 5, No. 2, pp. 2-16, Winter 1990.
8. S. N. Tabet, "High Frequency Performance of the Rhombic Illuminator," Doctoral Dissertation, Mississippi State University, December 1989.
9. J. P. Donohoe and S. N. Tabet, "HSI High Frequency Performance Verification/Upgrade," EG&G Projects, Final Technical Report, Contract No. F29601-88-0001, Subtask 03-05/00, November 1989.
10. B. D. Popovic, "Frequency-Domain Analysis of a Large NEMP-Simulator Wire Antenna," *IEE Proceedings*, Vol. 135, Pt. H, No. 2, April 1988.

## 1994 INSTITUTIONAL MEMBERS

<p>THE AEROSPACE CORPORATION PO Box 92957 Los Angeles, CA 90245-2957</p>	<p>ANDREW CORPORATION 10500 W 153rd Street Orland Park, IL 60462</p>	<p>ARC, INC 8201 Corporate Dr. Ste 3550 Landover, MD 20785</p>
<p>ASC &amp; ASSOCIATES, LTD 1201 Dawn Drive Belleville, IL 62220</p>	<p>ASELSAN INC. LIBRARY PO Box 101 Yenimahalle Ankara, TURKEY 06172</p>	<p>ATOMIC WEAPONS ESTAB UK Building E3, Awe Aldermaston Reading, Berkshire, UK RG7 4PR</p>
<p>AVTRONICS PO Box 8492 Hennopsmeer, S AFRICA 0046</p>	<p>BNR EUROPE LTD London Road Harlow, Essex, UK CM17 9NA</p>	<p>BRITISH BROADCASTING CO. Kingswood Warren Tadworth, Surrey, UK KT20 6NP</p>
<p>CAMBRIDGE CONSULTANTS LTD. Milton Road/Science Park Cambridge, Cambs, UK CB5 4DW</p>	<p>CSELT-RADIO Via Guglielmo Reiss Romoli 274 Turin, ITALY 10148</p>	<p>CULHAM LAB UK Atomic Energy Authority Abingdon, Oxford, UK OX14 3DB</p>
<p>DAWSON SUBSCRIPTION SERVICE PO Box 191 Mt. Morris, IL 61054-0191</p>	<p>DEFENSE RESEARCH ESTAB. 3701 Carling Ave. Ottawa, On, CANADA K1A 0K2</p>	<p>D L R OBERPFAFFENHOFEN Zentralbibliothek Wessling/Obb, GERMANY 8031</p>
<p>D S T O SALISBURY LIBRARY Box 1500 Salisbury, SA, AUSTRALIA 5108</p>	<p>DYNETICS, INCORPORATED PO Drawer B Huntsville, AL 35814-5050</p>	<p>ELECTRONICS RESEARCH INC. 108 Market Street Newburgh, IN 47630</p>
<p>ENGINEERING DEVELOPMENT EST. Private Bag 12 Ascot Vale, Victoria, AUSTRALIA 3032</p>	<p>ERIM INFORMATION PO Box 134001 Ann Arbor, MI 48113</p>	<p>FGAN/FHP Neuenahrer Strabe 20 D-5307 Wachtberg-Werthoven, GERMANY</p>
<p>GRUMMAN CORP. RES. CENTER Dept. 0582 Bethpage, NY 11714-3580</p>	<p>HARRIS CORPORATION LIBRARY PO Box 37 Melbourne, FL 32902-9739</p>	<p>HARRIS CORPORATION 1680 University Avenue Rochester, NY 14610-9983</p>
<p>HATFIELD &amp; DAWSON 4226 Sixth Avenue, NW Seattle, WA 98107</p>	<p>HKUST LIBRARY Clear Water Bay Road Kowloon, Hong Kong</p>	<p>HOKKAIDO DAIGAKU Nishi 8, Kita 13 Sapporo, JAPAN 060</p>
<p>HUGHES RESEARCH LIBRARY 3011 Malibu Canyon Road Malibu, CA 90255-4797</p>	<p>HUNTING ENGINEERING LTD Redding Wood Amphill, Bedford, UK MK45 2HD</p>	<p>IIT RESEARCH INST. LIBRARY 185 Admiral Cochrane Dr. Annapolis, MD 21401-7347</p>
<p>IMAGINEERING LIMITED 95 Barber Greene Rd. Suite 112 Don Mills, ON, CANADA M3C 3E9</p>	<p>KATHREIN-WERKE KG Postbox 260 Rosenheim 2, GERMANY D-8200</p>	<p>LINDA HALL LIBRARY 5109 Cherry Street Kansas City, MO 64110</p>
<p>LITTON ELECTRON DEVICES LIBRARY 960 Industrial Road San Carlos, CA 94404</p>	<p>LOCKHEED MISSILES AND SPACE 3251 Hanover Street Palo Alto, CA 94304</p>	<p>M/A COM INCORPORATED 100 Chelsford St. Lowell, MA 01851</p>
<p>MARCONI DEFENCE SYSTEMS The Grove, Warren Lane Stanmore, Middlesex, UK HA7 4LY</p>	<p>MARITELERADAR/BIBLIOTECA Viale Italia 72 Livorno 72, ITALY</p>	<p>MISSISSIPPI STATE UNIV LIBRARY PO Box 5408 Mississippi State, MS 39762</p>
<p>MIT LINCOLN LABORATORY LIBRARY 244 Wood Street Lexington, MA 02173-0073</p>	<p>MITRE CORPORATION LIBRARY 202 Burlington Road Bedford, MA 01730</p>	<p>MONASH UNIV/CAULFIELD PO Box 197/Caulfield East Melbourne, Vic, AUSTRALIA 3145</p>
<p>MOTOROLA INCORPORATED 1301 E Algonquin Road Schamburg, IL 60196</p>	<p>MPB TECHNOLOGIES INC. 151 Hymus Blvd. Pointe-Claire, Que, CANADA H9R 1E9</p>	<p>NAVAL RESEARCH LAB. 4555 Overlook Avenue SW Washington, DC 20375-5336</p>
<p>NORWEGIAN TELECOM RESEARCH PO Box 83 Kjeller, NORWAY N-2007</p>	<p>OCEAN APPLIED RESEARCH CORP. 10447 Roselle Street San Diego, CA 92121</p>	<p>OFFICE OF RESEARCH PO Box 15183 Arlington, VA 22215-0183</p>

### 1994 INSTITUTIONAL MEMBERS (Continued)

<p>PARAMAX SYSTEMS CANADA 6111 Royalmount Avenue Montreal, Que. CANADA H4P1K6</p>	<p>PENNSYLVANIA STATE UNIVERSITY Pattee Library University Park, PA 16802</p>	<p>QUEEN MARY &amp; WESTFLD COLL. Mile End Road London, UK E1 4NS</p>
<p>RACAL-REDAC GROUP LIBRARY Newton Croydon, Victoria, AUSTRALIA</p>	<p>RADIO FREQUENCY SYSTEMS Box 191 Croydon, Vic. AUSTRALIA 3136</p>	<p>SAAB-SCANIA AB Tusta 5 Linköping, SWEDEN S-58188</p>
<p>SAIC 300 Nickerson Road Marlborough, MA 01752</p>	<p>SERCO SERVICES Cheeseman's Lane Hambrook, W Sussex, UK</p>	<p>STG NATIONAL LUCHT-EM Ruimtevaart Lab. A Fokkerweg 2 Amsterdam, NETHERLANDS 1059</p>
<p>SWETS SUBSCRIPTION SERVICE 440 Creamery Way Suite A Exton, PA 19341</p>	<p>SYRACUSE RESEARCH CORPORATION Merrill Lane Syracuse, NY 13210-4080</p>	<p>TASC LIBRARY 55 Walkers Brook Drive Reading, MA 01887</p>
<p>TECHNION-ISRAEL INST OF TECH Faculty of Electrical Engineering Technion City, ISRAEL 32000</p>	<p>TECHNICAL RESEARCH CENTRE Telecom Lab/Otakaari 7B Espoo, FINLAND SF-01250</p>	<p>TELECOM AUSTRALIA 770 Blackburn Road Clayton, Victoria, AUSTRALIA 3168</p>
<p>TELEX COMMUNICATIONS INC. 8601 E. Cornhusker Highway Lincoln, NE 68505</p>	<p>THE MOTOR INDUSTRY Watling Street Nuneaton, Warwicks, UK</p>	<p>UNIV. OF CENTRAL FLORIDA LIB. PO Box 162440 Orlando, FL 32816</p>
<p>UNIVERSITÄT DER BUNDESWEHR Werner Heisenberg Weg 39 Neuberg, GERMANY W-8014</p>	<p>VISTA RESEARCH INC. 100 View St, #202, Box 998 Mountain View, CA 94042</p>	<p>FANFIELD LIMITED Sproughton House Sproughton, Ipswich Suffolk, UK IP8 3AW</p>

## INFORMATION FOR AUTHORS

### PUBLICATION CRITERIA

Each paper is required to manifest some relation to applied computational electromagnetics. Papers may address general issues in applied computational electromagnetics, or they may focus on specific applications, techniques, codes, or computational issues. While the following list is not exhaustive, each paper will generally relate to at least one of these areas:

1. Code validation. This is done using internal checks or experimental, analytical or other computational data. Measured data of potential utility to code validation efforts will also be considered for publication.

2. Code performance analysis. This usually involves identification of numerical accuracy or other limitations, solution convergence, numerical and physical modeling error, and parameter tradeoffs. However, it is also permissible to address issues such as ease-of-use, set-up time, run time, special outputs, or other special features.

3. Computational studies of basic physics. This involves using a code, algorithm, or computational technique to simulate reality in such a way that better or new physical insight or understanding is achieved.

4. New computational techniques, or new applications for existing computational techniques or codes.

5. "Tricks of the trade" in selecting and applying codes and techniques.

6. New codes, algorithms, code enhancement, and code fixes. This category is self-explanatory but includes significant changes to existing codes, such as applicability extensions, algorithm optimization, problem correction, limitation removal, or other performance improvement. NOTE: CODE (OR ALGORITHM) CAPABILITY DESCRIPTIONS ARE NOT ACCEPTABLE, UNLESS THEY CONTAIN SUFFICIENT TECHNICAL MATERIAL TO JUSTIFY CONSIDERATION.

7. Code input/output issues. This normally involves innovations in input (such as input geometry standardization, automatic mesh generation, or computer-aided design) or in output (whether it be tabular, graphical, statistical, Fourier-transformed, or otherwise signal-processed). Material dealing with input/output data base management, output interpretation, or other input/output issues will also be considered for publication.

8. Computer hardware issues. This is the category for analysis of hardware capabilities and limitations in meeting various types of electromagnetics computational requirements. Vector and parallel computational techniques and implementation are of particular interest.

Applications of interest include, but are not limited to, antennas (and their electromagnetic environments), networks, static fields, radar cross section, shielding, radiation hazards, biological effects, electromagnetic pulse (EMP), electromagnetic interference (EMI), electromagnetic compatibility, power transmission, charge transport, dielectric and magnetic materials, microwave components, MMIC technology, remote sensing and geophysics, communications systems, fiber optics, plasmas, particle accelerators, generators and motors, electromagnetic wave propagation, non-destructive evaluation, eddy currents, and inverse scattering.

Techniques of interest include frequency-domain and time-domain techniques, integral equation and differential equation techniques, diffraction theories, physical optics, moment methods, finite differences and finite element techniques, modal expansions, perturbation methods, and hybrid methods. This list is not exhaustive.

A unique feature of the Journal is the publication of unsuccessful efforts in applied computational electromagnetics. Publication of such material provides a means to discuss problem areas in electromagnetic modeling. Material representing an unsuccessful application or negative results in computational electromagnetics will be considered for publication only if a reasonable expectation of success (and a reasonable effort) are reflected. Moreover, such material must represent a problem area of potential interest to the ACES membership.

### EDITORIAL REVIEW

In order to ensure an appropriate level of quality control, papers are refereed. They are reviewed both for technical correctness and for adherence to the listed guidelines regarding information content. Authors should submit the initial manuscript in draft form so that any suggested changes can be made before the photo-ready copy is prepared.

## **STYLE**

The ACES Journal is flexible, within reason, in regard to style. However, certain requirements are in effect:

1. The paper title should NOT be placed on a separate page. The title, author(s), abstract, and (space permitting) beginning of the paper itself should all be on the first page. The title, author(s), and author affiliations should be centered (center-justified) on the first page.

2. An abstract is REQUIRED. The abstract should state the computer codes, computational techniques, and applications discussed in the paper (as applicable) and should otherwise be usable by technical abstracting and indexing services.

3. Either British English or American English spellings may be used, provided that each word is spelled consistently throughout the paper.

4. Any commonly-accepted format for referencing is permitted, provided that internal consistency of format is maintained. As a guideline for authors who have no other preference, we recommend that references be given by author(s) name and year in the body of the paper (with alphabetical listing of all references at the end of the paper). Titles of journals, monographs, and similar publications should be in boldface or italic font or should be underlined. Titles of papers or articles should be in quotation marks.

5. Internal consistency shall also be maintained for other elements of style, such as equation numbering. As a guideline for authors who have no other preference, we suggest that equation numbers be placed in parentheses at the right column margin.

6. The intent and meaning of all text must be clear. For authors who are NOT masters of the English language, the ACES Editorial Staff will provide assistance with grammar (subject to clarity of intent and meaning).

7. Unused space should be minimized. For this reason, sections and subsections should not normally begin on a new page.

## **MATERIAL SUBMITTAL FORMAT AND PROCEDURE**

Only camera-ready copies are accepted for publication, although authors may submit other copies for publication review. The term "camera-ready" means that the material is neat, legible, and reproducible. There is NO requirement for India ink or for special paper; any plain white paper may be used. However, faded lines on figures and white streaks along fold lines should be avoided. Original figures – even paste-ups – are preferred over "nth-generation" photocopies. These original figures will be returned if you so request.

While ACES reserves the right to re-type any submitted material, this is not generally done.

All submissions should be sent in triplicate to the Editor-in-Chief. Each submission should be accompanied by a cover letter. The cover letter should include the name, address, and telephone of at least one of the authors.

## **PUBLICATION CHARGES**

At the present time, there are no page charges for camera-ready articles. Authors are entitled to 15 free reprints of their articles and must request these from the Managing Editor. Additional reprints are available to authors, and reprints available to non-authors, for a nominal fee.

## **COPYRIGHTS AND RELEASES**

Each author must sign a copyright form and obtain a release from his organization vesting the copyright with ACES. Both forms will be provided by ACES and allow both the author and his organization to use the copyrighted material freely for their own private purposes.

Permission is granted to quote short passages and reproduce figures and tables from an ACES Journal issue provided the source is cited. Copies of ACES Journal articles may be made in accordance with usage permitted by Sections 107 or 108 of the U.S. Copyright Law. This consent does not extend to other kinds of copying, such as for general distribution, for advertising or promotional purposes, for creating new collective works, or for resale. The reproduction of multiple copies and the use of articles or extracts for commercial purposes require the consent of the author and specific permission from ACES. Institutional members are allowed to copy any ACES Journal issue for their internal distribution only.